Scanning Tunneling Microscopy in Electrochemical Environments

Thesis by

Michael Joseph Heben

In Partial Fulfillment of the Requirements

for the Degree of

Doctor of Philosophy

California Institute of Technology

Pasadena, California

1990

(Submitted February 8, 1990)

Acknowledgements

Whew! That wasn't so bad - was it? Two for flinching.

I thank God I have the opportunity to acknowledge the support, encouragement, and love that has made this thesis possible. My Mom and Dad are incredible. They have always been "there" to help unravel and calm my twisted and paranoid mind during the throes of graduate school and life. They didn't get too mad at me when, as a child, I disassembled (without reassembling) things like the lawnmower and the doorbell. They also have provided a financial safety net that has cushioned me several times. For these reasons, and for many others, I thank and love them very much.

My sisters and brother, and their spouses and families, have also provided me with considerable love and support over the years. I'm thankful to be part of such a warm and loving family. Their wisdom and experience on matters like women, law, women, boating, parents, drinking, life, and clothing styles may one day be useful to me (just kidding). I thank and love them all very much, too.

Several other individuals have become like family to me during my time in graduate school. Scott Smallwood has been as good a friend as is possible. He helped me to keep smiling under a variety of circumstances. He also taught me how to throw a forehand - schwa! Thanks Spot!

Wes Monroe introduced me to Ultimate frisbee and the fine art of early morning coffee drinking. Truly, two of the finer things in life! Ultimate, in particular, has brought me into contact with fine people in Pasadena, Palo Alto, and wherever the disk flies. Thanks, and C.U.

Reggie Penner has been a great friend and coworker. Together, we were able to work as an effective team in the lab and on the pool table. I'll miss the day-to-day exposure to his funny faces, unique sense of humor, and accurate evaluations of people and

situations. Kristl Penner has also been a great friend during the past few years. Dinners and beers at their place saved my sanity several times. Good luck at Irvine!

Bruce Tufts has helped me in many ways during this PhD process. He has always been willing to take time to help me, and others, regardless of the magnitude of the problem. His keen chemical insight and constantly up-beat nature have been invaluable to me. Thanks dibude! Viel Spass in Berlin!

Kurt Fleischer and I have been groupies for each other at Stanford and Caltech. He can make a stone wall loosen-up and he convinced me to take the time to smell good things (e.g., roses). Thanks Kurt!

Malcolm Forbes and Amit Kumar have also been great friends and coworkers. I've learned alot from both of them and I thank them for proof reading drafts of my proposals and thesis. I hope I can find a working environment as fun and fruitful as the one they helped to make at Caltech.

My time in the graduate school has been enriched by the opportunity to work with several other past and present Lewis Group members including; Ian Abrahams, Pat Anderson, Rik Blumenthal, Laura Ferry, Valerie Loubett, Terri Longin, Sharon Lunt, George McMannis, Gordon Miskelly, Charlotte Newcombe, Mark Rosenblum, Mary Rosenbluth, Gail Ryba, Mike Sailor, Pat Santangelo, Mike Schmidt, and Gary Schreve. It has also been quite enjoyable to work closely with our floor-mates, the Bercaw Group. I'm lucky to have been associated with all of these fine people.

My research advisor, Nate Lewis, provided the resources, the intellectual leadership, and the psychic energy that enabled me to pursue my thesis research. Importantly, he is also able to distance himself from the advisor/advisee relationship to become "one of the guys." It has been a privilege working with him, and I thank him for the guidance he has offered during my tenure in The Group.

Our scanning tunneling microscopy (STM) program got its start through a collaboration with Cal Quate and his research group at Stanford University. Much of what I know about STM stems from the many long hours spent in Cal's lab with Moris Dovek and Chris Lang. I thank them for sharing their knowledge so freely.

I am also grateful to Professors Sunney Chan, Bob Grubbs, and Rudi Marcus for agreeing to sit on my committee. I am especially indebted to Sunney Chan for his guidance and advice during my time at Caltech.

Abstract

Scanning tunneling microscopy (STM) has been demonstrated to be an important analytical tool for the *in situ* characterization of electrode surfaces. However, in an electrochemical environment, the tip/sample bias necessary for electron tunneling can also drive heterogeneous charge transfer reactions between the solution-contacted portions of the tip and sample. This faradaic current acts in parallel to the normally measured tunneling current and the measured sum may not exhibit the expected exponential dependence on tip/sample separation. As a result, the interpretation of STM-derived data is not straightforward. The faradaic current component can be selectively reduced by coating the shaft and apex of the STM tip with insulating layers. Two tip-insulating procedures were developed, employing thin layers of either glass or polymer, that effectively reduce tip/sample faradaic currents even in the presence of redox active ions. The amount of exposed metal remaining after insulation was characterized with cyclic voltammetry. Using these insulated STM tips in an instrument constructed specifically for electrochemical investigations, atomic resolution images of highly ordered pyrolytic graphite were obtained in deionized water and in aqueous 0.1 $\underline{M}$ NaCl solutions at tip biases of ± 1.5 V, and in aqueous solutions simultaneously containing 0.1 $\underline{M}$ $Fe(CN)_6^{3-}$, 0.1 $\underline{M}$ $Fe(CN)_6^{4-}$, and 1.0 $\underline{M}$ NaCl at biases of ± 0.8 V. Images of MoS_2 were obtained in 0.5 $\underline{M}$ $NaClO_4$ at tip potentials as large as + 0.5 V. The distance dependence of the tip/sample faradaic current was investigated for the two different kinds of coated tips. A reduction in the faradaic current at tip/sample spacings less than ca 0.3 μm was observed for polymer-coated tips. No such reduction was observed for glass-coated tips. Thin-layer current enhancements were observed for these tips when the amount of exposed metal area was relatively large (ca > 50 nm^2). The tip insulation techniques were also used to produce, with minor modifications, conical and hemispherical ultramicroelectrodes. These were characterized with cyclic voltammetry and chronoamperometry and were applied to the measurement of the heterogeneous rate constant for $Ru(NH_3)_6^{3+}$ reduction.

Table of Contents

Chapter 5

Chapter 1

Scanning Tunneling Microscopy in Electrochemical Environments

Introduction

Scanning tunneling microscopy (STM) has proven to be a powerful and unique tool for the study of surfaces.[1] The technique is extremely versatile in that depending on the mode in which the instrument is operated, a routine investigation can yield information concerning the spatial distribution of surface atoms, the electronic state density, and the surface work function. During the past several years STM has been employed to investigate surfaces in a variety of ambients, including ultrahigh vacuum,[2] cryogenic fluids,[3] atmospheric pressures of gasses,[4] and electrolytic solutions (*vide infra*). The latter demonstrations have signaled that STM has the potential to become an important analytical tool for the *in situ* characterization of electrode surfaces and double layer structure.

In the STM experiment a conducting "tip" that terminates in a single atomic asperity is positioned within several angstroms of a conducting surface. A potential difference applied between the tip and the sample causes a tunneling current to flow across the thin tunneling gap. With the use of piezoelectric materials and negative feedback control, the tunneling current is stabilized while the tip is rastered across the surface. In constant current mode a map of the atomic-scale features of the sample is produced by recording the vertical displacement of the tip required to maintain a constant tunneling current.[5] Alternatively, in constant height mode the feedback control loop responds only rapidly enough to maintain a constant average tunneling current. An image of the surface is constructed by plotting the difference between the average value of the tunneling current and the actually measured tunneling current variations as a function of lateral tip position.[5]

To date, the use of STM for *in situ* studies of electrode surfaces has been limited. The application of the technique has been hindered by the lack of suitable instrumentation and by the need for new conceptual tools. Advances in these two areas should allow scanning tunneling microscopy and spectroscopy methods to be used to investigate the

geometric and electronic features of solution covered electrodes. Such capabilities will provide the electrochemist with an unprecedented view of the important properties of electrode materials. This thesis describes research that represents several important steps toward achieving these goals.

One of the contributions described in this work involves the development of several strategies for producing tunneling tips that are covered with insulating layers. The effect of the dielectric coating is to reduce the area of the tip that is exposed to solution in order to minimize faradaic currents. These coated tips enable the detection of an electron tunneling current even in the presence of solutions containing redox active ions. We have used electrochemical techniques extensively to characterize the size and geometry of the metal area that remains exposed after insulation. In addition to providing valuable information relevant to STM experiments, electrochemical characterization methods indicated that tips produced via our insulation processes could also behave as well-defined ultramicroelectrodes (UMEs). A second major portion of this thesis presents these characterization methods and describes how these UMES have been used to measure extremely fast heterogeneous rate constants (c.a. k^o > 0.1 cm/sec). These results will be presented in Chapter 5.

Motivation for Studies of the Solid/Liquid Interface

The relationship between structure and function at the electrode/electrolyte interface plays a central role in electrochemical systems. An understanding of the nature of this interdependence will comment on such diverse phenomena as the frictional forces acting between sliding surfaces,[6] the aggregation properties of colloidal suspensions,[7] and the rates of electron transfer reactions at semiconducting[8] and metallic electrodes.[9] The atomic-scale structure at the electrode/electrolyte interface may be approximately understood by considering the electrical double layer (EDL) that forms when two phases of

differing electrochemical potential are equilibrated. An instructive case is that of a metal electrode immersed in an electrolytic solution. The solution side of the EDL, which consists of compact and diffuse components, supports virtually all of the electric potential difference between the two phases.[10] The compact portion, also known as the "inner Helmholtz layer," consists of a thin solution layer of molecular dimensions at the electrode's surface, and its structure is governed by both electrostatic and chemical interactions. As a result, the near-electrode region of the solution might contain specifically adsorbed molecules and ions, oriented dipoles, and solvent molecules. In contrast, the structure of the diffuse portion of the EDL is controlled solely by electrostatics, as described by the Gouy-Chapman theory.[10] This region drops the remainder of the electric potential difference between the electrode and the solution.

The interplay between electrostatic and chemical effects at the electrode/electrolyte interface gives rise to the three-dimensional structure of the EDL.[10] The heterogeneity on the solution side of the interface is expected to be dependent on the heterogeneity present at the electrode surface. Additionally, the condition for minimum Gibbs Free Energy at the interface might provide sufficient driving force to reposition the surface atoms of the electrode. Thus, the electronic, compositional, and geometrical structure of the electrode/electrolyte interface depends in a synergistic fashion on the properties of both the electrode and the electrolyte.

A traditional approach towards understanding the relationship between structure and function at electrode surfaces involves correlating measurements of electrochemical cell observables (such as electrode charge, potential, and cell current) with the morphological, compositional and electronic properties of the near-surface region of the electrode. An evaluation of these latter properties is most readily performed *ex situ*. Once the electrode has been removed from the electrochemical environment, the researcher gains access to numerous analytical techniques, including those available only in ultrahigh vacuum (UHV).[11]

The surface composition of emersed electrode materials may be analyzed with secondary ion mass spectrometry (SIMS), Auger electron spectroscopy (AES), x-ray photoelectron spectroscopy (XPS), or x-ray absorption techniques.[11] Scanning electron and optical microscopies can be used to image the morphological features of an electrode. Information concerning the spatial distribution of atomic-scale features may be obtained with STM or ion and electron diffraction techniques. The distribution of electronic states on the electrode surface can be studied with electron energy loss spectroscopy (EELS), ultraviolet photoelectron spectroscopy (UPS), and inverse photoemission (IPS).[11]

Although the electrode can be readily evaluated in UHV, performing the surface investigation outside the electrochemical environment raises an important question: Are the electrode features that are observed *ex situ* representative of those that are responsible for the electrochemical behavior? Several researchers have performed investigations designed to address this issue.[12] The usefulness of *ex situ* studies has been underscored by the good agreement between *in situ* and *ex situ* derived structural data for a few strong-adsorption systems.[13] There will always be some concerns, however, that the *ex situ* surface may not be identical to the *in situ* surface.[14] Such concerns are especially warranted when loosely bound adsorbate species or the solution side of the EDL governs the behavior of the electrode material. Removal of the electrode may also cause surface reconstructions resulting from changes in the condition for minimum free energy at the interface.[14] And although the atomic-scale structures of ordered adsorbate lattices may be identical for certain systems *in vacuo* and in solution (*vide infra*), the dielectric properties of the contacting medium probably affect the configuration and extension of electronic orbitals. Moreover, because potential control of the electrode cannot be maintained outside the electrochemical cell, *ex situ* characterization cannot comment on dynamic features of the solid/liquid interface. Consequently, *ex situ* measurements should be cautiously interpreted, and *in situ* characterization methods should be pursued.

In Situ Investigations of Electrode Materials

The ability to externally control the electrochemical potential of the electrons within a conducting phase has enabled a variety of thermodynamic and kinetic measurements. The most useful and readily accessible *in situ* studies are based on conventional electrochemical techniques that measure surface roughness, surface charge, adsorption isotherms, and electrode kinetics.[10,15] With these approaches, however, the state of the surface cannot be directly ascertained. Details of the interface that may control the behavior of the electrode, or produce some desirable effect if optimized, can be lost in these macroscopic measurements.

The difficulty in establishing the pertinence of *ex situ* derived data stems from the limited number of experimental techniques that are available for direct *in situ* structural characterization. The most widely used experimental approaches involve the absorption, scattering and diffraction of photons. Various Raman and infrared spectroscopic techniques that probe the vibrational modes of surface adsorbates have commented on the identity, orientation, and bonding environment of near-electrode molecular species.[16] Structural information concerning the adsorbates or the underlying electrode surface may be only indirectly obtained with these techniques, however, since the interpretation of spectra is complex and since spatially averaged quantities are measured.

Various x-ray techniques allow a more direct probing of the interfacial structure at electrode surfaces. In particular, surface extended x-ray absorption fine structure (SEXAFS)[17] and x-ray absorption near edge structure (XANES)[18] can, when operated in fluorescence-yield mode, comment on the number of and distance between nearest neighbors as a function of electrode potential. These data may then be employed to construct models for the electrode/adsorbate system. Adsorption isotherms may also be measured since the magnitude of the absorption edge is proportional to the total number of

absorbers. X-ray standing wave investigations have also been employed to study the geometry of adsorbates on surfaces.[17] With this technique the distance between the plane of an adsorbate lattice and the underlying surface is measured. Additionally, long-range order in the plane of the sample has been investigated with grazing angle x-ray diffraction.[13a] Interadsorbate distances and the alignment of the adsorbate lattice may be ascertained if the domain width is sufficiently large (ca > 50Å). Several systems involving underpotential deposition onto highly ordered metal substrates have recently been studied with these x-ray techniques, and a growing body of evidence indicates that the electrochemically formed monolayers are very similar to those formed in UHV. Unfortunately, x-ray based approaches have not found widespread use in the study of the electrode/electrolyte interface because of the need for access to synchrotron radiation sources and the need for nearly perfect electrode surfaces. Although detailed structural information has been obtained for a few well-defined systems, these techniques also measure averaged signals from macroscopic (ca mm^2) areas.

Determinations of the distribution of electronic states on solution-covered electrode surfaces have utilized electrolyte electroreflectance (EER),[19] *in situ* photoemission,[20] and *in situ* inverse photoemission.[21] In the work of Francke and coworkers,[19a] surface states on Ag and Au electrodes were identified with EER. Further investigations employed EER to study the quenching of these surface states as a function of the strength of adsorption of the electrolyte anion. Similar observations have not been possible for the semiconductor/electrolyte interface because of the complexity of the EER spectra. In these systems, however, EER has been used to study the position of the flat-band potential.[19c]

In situ photoemission[20] and inverse photoemission[21] spectra are also difficult to interpret. These techniques involve measuring the extent of charge transfer from optically populated metal states into solution phase scavengers, and photon emission resulting from the injection of energetic electrons or holes into the electrode from redox species in

solution, respectively. Unlike in the UHV analogs, the energy distributions of the solution donor (or acceptor) species must be well known in order to extract information concerning the electrode. In fact, these approaches may provide a means of investigating the distribution function for electronic states in solution.

Scanning Tunneling Microscopy as an *In Situ* Tool

Scanning tunneling microscopy may prove to be a valuable complement to other *in situ* techniques. The first atomic resolution images of highly ordered pyrolytic graphite (HOPG) under deionized water, obtained by Sonnenfeld and Hansma,[22] demonstrated that spatial variations in electron density on a solution-covered surface could be detected with STM. Consequently, it is reasonable to expect that the surface structures that have been probed with x-rays could also be directly imaged with STM. A unique contribution from STM in this application arises from the inherently small areas (ca. 1-2 Å^2) that are involved in the measurement process. This effect relaxes the requirement for long range surface order and, unlike any of the x-ray techniques described above, should allow ordered and disordered adsorbate overlayers and domain wall structures to be directly imaged.

STM has also been shown to provide surface electronic information. The most common application in this area has involved the use of differential conductance (dI/dV) spectroscopic methods to probe the density of states in metals and semiconductors. Materials of interest to electrochemists that have been investigated in UHV include Si,[23] GaAs,[24] graphite,[25] Pd[26] and Au.[26] Once again, STM's unique contribution arises from the inherently localized electron tunneling probe employed. This feature of STM has allowed the mapping of the spatial distribution of electronic states with atomic resolution. Although these investigations were typically performed in UHV, it is expected that similar capabilities could be demonstrated for liquid-covered surfaces. The success of STM in this task will depend on the ability to discriminate between the tunneling current and other electron-

transfer mechanisms that may play a role in the *in situ* experiment (e.g., faradaic charge-transfer).

The STM methodologies that will facilitate the *in situ* measurement of surface electronic structure should also enable other STM-based spectroscopic inquiries. Measurement of the variations in tunneling current with modulations in the tip/sample spacing (dI/dS spectroscopy) has been shown to yield information concerning the shape of the potential distribution, and thus of the work function, at conducting sample surfaces. Application of dI/dS spectroscopy to solution-covered metal electrodes has already yielded spatially resolved information concerning the surface work function (*vide infra*). Further advances will comment on the distribution of potential in the EDL, the lifetime of solvated electrons, and the spatial decay of electronic wave functions. Similar investigations on semiconductor electrodes may comment on the magnitude and behavior of the barrier height and the position of the energy bands in photoelectrochemical cells.

Clearly, STM possesses tremendous potential for the elucidation of processes at the electrode/electrolyte interface. The technique is complementary to other available *in situ* and *ex situ* techniques and offers several unique advantages. The inherently localized nature of the tunneling probe relaxes the need for sample perfection and long-range order. Thus, structural and electronic information can be obtained from disordered and ordered solution-covered conducting surfaces with unparalleled spatial resolution. Moreover, the versatility of the technique allows such information to be acquired from one specific area of a sample, without requiring changes in the experimental setup. Additionally, the potential of the sample electrode may be altered during an *in situ* STM to allow the observation of dynamic features. The combination of capabilities available in scanning tunneling microscopy are ideally suited for studies of the electrode/electrolyte interface.

History of the Application of STM to Studies of Liquid and Solution-Covered Surfaces

Scanning tunneling microscopy was first introduced by Binnig et al. in two seminal papers, which appeared in 1982.[27] As noted above, the technique has been employed since then by numerous research groups to investigate a variety of surfaces in contact with a variety of ambients. Several instances where electrode surfaces were prepared in an electrochemical cell and then imaged with STM *ex situ* are particularly interesting from an electrochemical point of view.[28] These applications, however, are not directly related to the subject of this thesis and will not be discussed here. Instead, we will focus our attention on the history of the development of *in situ* STM studies of liquid and solution-covered surfaces. The interested reader may consult the sources referenced above for further information concerning the application of STM to studies of surfaces in contact with other ambients.

The first use of STM for imaging a solution-covered surface was reported by Sonnenfeld and Hansma in 1986.[22] These researchers obtained atomic resolution STM images of HOPG in water, and images at lower resolution of Au in aqueous 2 m$\underline{M}$ NaCl solutions. HOPG images were obtained using total tip-sample biases of 100 mV (tip -) and total currents (faradaic + tunneling) of 50 nA. Individual solvent molecules were not observed in the STM images, presumably because their positions were time-averaged by thermal motions, which were fast in comparison to the tip speed. Itaya and Sugawara[29] subsequently reported images of HOPG in aqueous 0.05 $\underline{M}$ H_2SO_4 in the presence of residual faradaic currents of 0.2 nA (bias = 100 mV, tip -). Liu et al.[30] obtained one-dimensional traces with a resolution of ca 30 nm of solution-covered, metal-coated, integrated circuits. In this case, the authors used a total current of 5 - 25 nA, which included a substantial distance-dependent faradaic current component, to control the interelectrode distance with a conventional feedback arrangement. This work apparently formed the basis for the development of scanning electrochemical microscopy (SECM). Husser and

coworkers have published several papers employing SECM where the faradaic current, rather than the tunneling current, may be used to image conducting and insulating surfaces with micron resolution.[31]

Sonnenfeld et al.[32] have used STM to determine the topography of etched (0.05 v/v% Br_2/MeOH) and polished GaAs surfaces. STM images of these surfaces were obtained both in aqueous 0.01 $\underline{M}$ KOH and in concentrated aqueous NH_4OH. GaAs surfaces exposed to the chemical etchant and polished with lens paper exhibited average roughnesses of 1 nm over intervals of 5 to 1000 nm. Occasional 100 nm scale defects were also present on such surfaces. STM images of etched GaAs surfaces in 0.01 $\underline{M}$ aqueous KOH remained unchanged over periods of several minutes. Interestingly, the GaAs lattice could not be resolved at these solution-covered surfaces, despite the fact that previous atomic resolution images of GaAs in UHV have been reported.[2a,24a]

Work by Schneir and coworkers[33] extended the list of pure liquids suitable for STM studies by demonstrating imaging capabilities with a series of nonpolar organic liquids, such as paraffin oil and fluorocarbon grease. These liquids have the advantage of possessing greater viscosity than aqueous solutions, and hence exhibit inherently smaller residual currents. These workers were able to attain tip-substrate biases (ca 3 V) greater than those routinely possible in air or in aqueous solutions. In addition, these liquids were found to improve the signal to noise ratio of the STM atomic resolution images, possibly because of improved vibrational damping characteristics as a result of the liquid layer. The authors suggest that nonpolar, organic liquids may serve to protect air-sensitive, or otherwise reactive surfaces, and hence may facilitate the imaging of such surfaces under ambient conditions.

Schneir et al.[34] have also used the greater biases available in nonpolar organic liquids (~ 3 V) to facilitate the surface modification of gold surfaces. The features introduced with this procedure were imaged in situ under a fluorocarbon grease. Gold mounds, initially

ca 10 nm in diameter, decreased in height and broadened over a period of 24 h as a result of diffusion. Preliminary self-diffusion coefficients for gold atoms at these surfaces of $D = 10^{-20} - 10^{-16} \, cm^2 \, sec^{-1}$ were estimated from the observed rate of change of height with time. This is the first instance in which solid-state-like diffusion coefficients have been estimated from STM images. Thus, it seems likely that room-temperature diffusion coefficients might be obtained with similar procedures for well-characterized systems in the future with STM.

Itaya et al.[35] have examined the nanotopography of polycrystalline Pt electrode surfaces immersed in aqueous, 0.1 $\underline{M}$ H_2SO_4. Increases in the surface area of Pt electrodes accompanying cycling in this electrolyte were associated with electrofaceting of the electrode surface, in agreement with the *ex situ* observations of Gomez et al.[28a] and Vasquez et al..[28b] The crystallographic orientation of these facets, however, was not apparent in the *in situ* investigations.

Using a unique four-electrode STM, Lev et al.[36] obtained the first images of electrode surfaces under potentiostatic control. They employed an additional platinum electrode and a battery to bias the tip and nickel sample away from the rest potential of the sample in a 0.5 $\underline{M}$ H_2SO_4 solution. The resulting electrochemical potential of the sample was measured with respect to a saturated calomel reference electrode (SCE). The current-bias relationships obtained for reduced and anodically passivated nickel surfaces revealed that the exponential current-distance relationship expected for a tunneling-dominated current was not observed at the oxide-covered surfaces. On this basis, the authors concluded that the nickel oxide layer was electrically insulating, and was greater than ca 10 A in thickness. These researchers demonstrated the ability to decouple the tip-substrate bias from the substrate potential, and were the first of several (*vide infra*) to image electrode surfaces under potential control.

Morita et al.[37] have examined polycrystalline Ag surfaces *in situ* in the presence of a 0.1 $\underline{M}$ KCl solution. After an electrochemical cycling treatment, the electrode was

disconnected from potentiostat circuitry and imaged with STM. Large current spikes in the STM image decayed with time$^{-1/2}$ and were attributed to mass transfer controlled reactions at activated sites. The origin of these current spikes, however, was not identified.

The effects of Cl⁻ adsorption on STM images of Au(111) single crystals were investigated by Wiechers et al..[38] The Au electrode was imaged at positive potentials vs. a Pd-H reference electrode in a 0.05 $\underline{M}$ H₂SO₄ aqueous solution also containing 5 m$\underline{M}$ NaCl. With increasing positive electrode potentials (up to +0.9V), the STM images became "noisier," presumably because of increased Cl⁻ adsorption. Upon returning to less positive potentials, it was observed that the structure of terraces (which were several atomic layers high) had been modified by the Cl⁻ adsorption. These experiments also employed a novel strategy for combatting residual faradaic currents, which was introduced earlier by Lustenberger et al.[39] in their STM observations of HOPG in contact with 0.1 $\underline{M}$ NaCl. The strategy involved poising the potential of the W tip at a constant potential vs. the reference electrode so that faradaic currents were minimized. As a result the tip/sample bias was necessarily changed with any change in the electrochemical potential of the sample. The effective work function of the Au(111) sample was measured to be ≈2.15 eV by monitoring the change in the logarithm of the tunneling current that accompanied changes in the tip/sample spacing.

Trevor et al.[40] have performed similar experiments with Au(111) films that were epitaxially grown on mica. They observed the roughening, dissolution, and annealing of the Au surface terrace structure that resulted from oxidation and reduction cycles in 0.1 $\underline{M}$ HClO₄. Analysis of atomic-layer resolution images obtained with the addition of 50 $\mu\underline{M}$ HCl revealed that the presence of HCl reduces the roughening that is due to oxidation-reduction cycles and may facilitate Au mobility on the surface. These investigations were performed with a constant tip/sample bias of -10 mV (tip -).

Gewirth and Bard[41] have studied surface changes that accompany oxidation of

HOPG. Before electrochemical cycling, atomic resolution images of HOPG obtained at 0.05

V *vs.* a Ag quasi-reference electrode (AgQRE) in 0.1 $\underline{M}$ H_2SO_4 were indistinguishable from

those obtained in air. After 20 cycles from 0 to 1.8 V *vs.* AgQRE, the surfaces displayed

roughness on the order of 100 Å, which was attributed to the formation of graphitic oxides.

Barrier height images were obtained by modulating the tip/sample spacing at 15 kHz and

measuring the resultant changes in the tunneling current. The barrier height image over the

unroughened portions of the sample yielded a value for the barrier height of 0.9 eV, while

measurement over the oxidized areas yielded values less than 0.25 eV. The lower barrier

height over the roughened regions served to support the conclusion that graphitic oxides

were indeed formed during the electrochemical cycling.

Several researchers have obtained images of electrodeposits on conducting

surfaces. Sonnenfeld and Schardt[42] deposited Ag on HOPG by sweeping the potential of

the surface to negative potentials *vs.* a Ag/AgCl reference electrode in an aqueous 0.05 $\underline{M}$

$AgClO_4$ solution. STM observations after 30 mC (corresponding to a uniform 0.09 μm

deposit) had been passed revealed only atomically flat graphite, indicating that no

deposition had occurred in the field of view. After a total charge of 59 mC had been passed

"rolling hills" were observed at positive tip biases of 0.100 V. Imaging after flowing 59 mC

with the sample at positive potentials revealed a single Ag island $\approx$ 600 Å in diameter. The

authors concluded from these observations that the electrodeposition proceeded by an

island, rather than a layer-plus-island, growth mechanism.

Hottenhuis et al.[43] have studied Ag deposition from 0.01 $\underline{M}$ $AgNO_3$ onto Ag(111)

single crystals. In these experiments, as in those of Sonnenfeld and Schardt discussed

above, potential control of the sample was removed before imaging with STM. At tip biases

of +10 mV, the freshly formed deposits were imaged with relatively large tunneling currents

of 10-20 nA. These large values were employed to overcome a 5 nA faradaic current

between the tip and the sample. The shapes of the observed nanometer-scale topographical features lent support to the conclusion that the deposition process was governed by surface active impurities, as described by the kinematic wave theory.

Uosaki and Kita[44] have employed STM to investigate the morphology of copper electrodeposits on polycrystalline Pt. Their instrument required only 4.2 s to obtain an image of a 100 nm^2 portion of the surface and, consequently, they were able to observe the time evolution of the topography of the Cu electrodeposits. The Pt electrode was potentiostatically maintained at -1.25 V *vs.* a Pt pseudoreference electrode to drive the deposition from an aqueous solution containing 2 m$\underline{M}$ $HClO_4$ and 5 m$\underline{M}$ $CuSO_4$. STM images were obtained with the tip poised +500 mV *vs.* the reference electrode. A steady-state current of 0.28 mA/cm^2 was flowing while the topography of the surface was imaged.

The underpotential deposition (UPD) of Pb on Au(111)/mica surfaces has recently been investigated by Green et al..[45] With the sample held at a potential where Pb *deposition did not occur* (+600 mV *vs.a* Pb/Pb^{2+} *reference electrode), pits, steps, and islands* were observed with nanometer resolution in the 0.05 $\underline{M}$ $HClO_4$ + 5 m$\underline{M}$ $Pb(NO_3)_2$ aqueous solution. Larger islands appeared in the STM image when the electrode potential was swept to + 60 mV *vs.* the reference electrode. During the deposition process a cyclic voltammogram was recorded, allowing the number of coulombs involved in the deposition process to be determined. The measured value corresponded to that expected for an HCP monolayer on the Au surface. Because the images were obtained at a constant tip/sample bias of +37 mV (tip +), substantial faradaic currents (several nanoamps) were measured between the tip and the sample as the electrode was swept toward the UPD potential.

The effect of Pb^{2+} adsorption on STM images of chemically polished Ag(100) electrodes has been studied by Christoph et al..[46] Prior to including Pb^{2+} ions into the solution, these authors performed imaging experiments in pure 0.5 $\underline{M}$ $NaClO_4$ to demonstrate that the topographical features of the Ag(100) electrodes were not altered on

the scale of their instrument's resolution (ca 1 nm) by changes in the potential of the electrode (with respect to SCE) or the tunneling current. For these experiments the potential of the STM tip was maintained at a value that minimized faradaic currents to the tip in bulk solution (ca +100mV *vs.* SCE). With addition of 1 m$\underline{M}$ Pb(ClO$_4$)$_2$, the structure of the Ag surface was smoothed upon cycling the potential of the electrode to negative values where Pb^{2+} adsorption occurred. The original, rougher surface was again obtained at more positive potentials where the Pb^{2+} ions were not specifically adsorbed. With lead ion adsorption the measured barrier height increased from $\approx$ 1.7 eV to 2.7 eV. As noted by the authors, this result was opposite to that expected given the bulk work functions values for Ag and Pb. Further experiments dealt with imaging morphological changes that accompanied deposition and stripping of multilayers of Pb^0. During the deposition and stripping, as in the previous adsorption studies, the tip was continually scanned to avoid any screening effects. The fact that temporally stable images could be obtained even while Pb^{2+} was being reduced at the sample indicated that the proximity of the tip inhibited deposition processes within the tunneling gap.

Organization of the Thesis

The material presented in this thesis is divided into two distinct, but interrelated, parts. Chapters 2-4 constitute Part I and focus on the application of STM to the study of electrochemical systems. In Chapter 2 the theoretical aspects of the electron tunneling process in STM will be described. The main focus in this chapter, however, will be on the new conceptual issues that arise when STM experiments are performed in electrochemical environments. In particular, the role of faradaic currents will be discussed extensively. Chapter 3 will describe the design, construction and operation of an STM that was built explicitly for electrochemical investigations. In Chapter 4 we will turn our attention to the preparation and characterization of insulated STM tips. The capabilities that these tips have

demonstrated for the *in situ* characterization of electrode surfaces, and the distance dependence of the tip/sample faradaic current measured using these tips, will also be discussed in Chapter 4. In the second portion of the thesis, composing Chapter 5, the uses of insulated tips as ultramicroelectrodes (UMEs) are explored. The minor alterations in the coating procedures and the electrochemical characterization of the resulting conical and hemispherical UMEs are presented. The application of these UMEs to the measurement of fast, heterogeneous rate constants will also be discussed.

References

1. For a survey of recent activity in the field see: Stobbs, W.N., Ed. *Scanning Tunneling Microscopy: Papers from the Third International Conference*, Blackwell Scientific Publications: Oxford, 1989.

2. Representative examples include: (a) Feenstra, R.M.; Stroscio, J.A.; Tersoff, J.; Fein, A.P. *Phys. Rev. Lett.* **1987**, 58, 1192-5. (b) Jaklevic, R.C.; Elie, L. *Phys. Rev. Lett.* **1988**, 60, 120-23. (c) Becker, R.S.; Golovchenko, J.A.; Swartzentruber, B.S. *Phys. Rev. Lett.* **1985**, 54, 2678-80. (d) Binnig, G.; Rohrer, H.; Gerber, Ch.; Weibel, E. *Phys. Rev. Lett.* **1983**, 50, 120-23. (e) Hamers, R.J.; Avouris, Ph.; Bozso, F. *Phys. Rev. Lett.* **1987**, 59, 2071-74. (f) Hallmark, V.M.; Chiang, S.; Rabolt, J.F.; Swalen, J.D.; Wilson, R.J. *Phys. Rev. Lett.* **1987**, 59, 2879-82.

3. Slough, C.G.; McNairy, W.W.; Coleman, R.V.; Drake, B.; Hansma, P.K. *Phys. Rev. B.* **1986**, 34, 994-1005. (b) Smith, D.P.E.; Kirk, M.D.; Quate, C.F. *J. Chem. Phys.* **1987**, 86, 6034-38.

4. Miranda, R.; Garcia, N.; Baro, A.N.; Pena, J.L.; Rohrer, H. *Appl. Phys. Lett.* **1985**, 47, 367-369. (b) Park, S.; Quate, C.F. *Appl. Phys. Lett.* **1986**, 48, 112-114. (c) Abraham, D.W.; Sattler, K.; Ganz, E.; Mamin, H.J.; Thomson, R.E.; Clarke, J. *Appl. Phys. Lett.* **1986**, 49, 853-55. (d) Carim, A.H.; Dovek, M.M.; Quate, C.F.; Sinclair, R.; Vorst, C. *Science* **1987**, 237, 630-33.

5. Hansma, P.K.; Tersoff, J. *J. Appl. Phys.* **1987**, 61(2), R1-23.

6. Goldblatt, I.L. in *Microscopic Aspects of Adhesion and Lubrication*; Georges, J.M., Ed., Tribology Series No. 7; Elsevier: New York, 1982; pp. 521-549.

7. Bijsterbosch, B.H. in *Trends in Interfacial Electrochemistry*; Silva, A.F., Ed., NATO ASI Series C Vol. 179; D. Reidel: Dordrecht, 1986; pp. 187-204. (b) Hunter, J.H. in *Comprehensive Treatise on Electrochemistry*; Bockris, J.O'M.; Conway, B.E.; Yeager, E., Eds.; Plenum: New York, 1980; Vol. 1, pp. 397-437.

8. Turner, J.A.; Parkinson, B.A. *J. Electroanal. Chem.* **1983**, 150, 611.

9. (a) Gennett, T.; Weaver, M.J. *Anal. Chem.* **1984**, 56, 1444. (b) Weaver, M.J. *J. Electroanal. Chem.* **1978**, 93, 231.

10. Bockris, J.O'M.; Reddy, A.K.N. *Modern Electrochemistry*; Plenum Press: New York, 1970.

11. Feldman, L.C.; Mayer, J.W. *Fundamentals of Surface and Thin Film Analysis*; North-Holland: New York, 1986.

12. (a) Kolb, D.M. *Zeit. Phys. Chem. N. F.* **1987**, 154, 179-199. (b) Bange, K.; Straehler, B.; Sass, J.K.; Parsons, R. *J. Electroanal. Chem.* **1987**, 229, 87-98.

13. (a) Samant, M.G.; Toney, M.F.; Borges, G.L.; Blum, L.; Melroy, O. *J. Phys. Chem.* **1988**, 92, 220-5. (b) White, J.H.; Abruna, H.D. *J. Phys. Chem.* **1988**, 92, 7131-34.

14. Robinson, J. in *Electrochemistry: Specialist Periodical Report*; Pletcher, D., Ed.; The Royal Society of Chemistry: London, 1984; Vol. 9, pp. 101-62.

15. Bard, A.J.; Faulkner, L.R. *Electrochemical Methods*; John Wiley & Sons: New York, 1980.

16. Fleischmann, M. in *Proceedings of the Robert A. Welch Foundation: XXX. Advances in Electrochemistry*; Robert A. Welch Foundation: Texas, 1986; pp. 91-168.

17. Abruna, H.D.; White, J.H.; Albarelli, M.J.; Bommarito, G.M.; Bedzyk, M.J.; McMillan, M. *J. Phys. Chem.* **1988**, 92, 7045-52, and references therein.

18. McBreen, J.; O'Grady, W.E.; Tourillon, G.; Dartyge, E.; Fontaine, A.; Pandya, K.I. *J. Phys. Chem.* **1989**, 93, 6308-11.

19. Francke, C.; Piazza, G.; Kolb, D.M. *Electro. Act.* **1989**, 34(1), 67-73. (b) Shen, W.; Fantini, M.C.A.; Tomkiewicz, M.; Gambino, J.P. *J. Appl. Phys.* **1989**, 66(4), 1759-64. (c) Gandia, J.; Pujadas, M.; Salvador, P. *J. Electroanal. Chem.* **1989**, 244, 69-79.

20. Sass, J.K. *Surf. Sci.* **1980**, 101, 507-17, and references therein.

21. McIntyre, R.; Roe, D.K.; Sass, J.K.; Storck, W. *J. Electroanal. Chem.* **1987**, 228, 293-300.

22. Sonnenfeld, R.; Hansma. P.K.; *Science* **1986**, 232, 211-13.

23. (a) Hamers, R.J.; Tromp, R.M.; Demuth, J.E. *Phys. Rev. Lett.* **1986**, 56, 1972-75. (b) Feenstra, R.M.; Stroscio, J.A.; Fein, A.P. *Surf. Sci.* **1987**, 181, 295-306.

24. (a) Stroscio, J.A.; Feenstra, R.M.; Fein, A.P. *Phys. Rev. Lett.* **1987**, 58, 1668-71. (b) Demuth, J.; Avouris, P. *Phys. Today* **1983**, Nov., 62.

25. Binnig, G.; Fuchs, H,; Gerber, Ch.; Rohrer, H.; Stoll, E.; Tosatti, E. *Europhys. Lett.* **1986**, 31, 1-36.

26. Kaiser, W.J.; Jaklevic, R.C. *IBM J. Res. Develop.* **1986**, 30, 411-16.

27. (a) Binnig, G,; Rohrer, H.; Gerber, Ch.; Weibel, E. *Appl. Phys. Lett.* **1982**, 40, 178-80. (b) Binnig, G,; Rohrer, H.; Gerber, Ch.; Weibel, E. *Phys. Rev. Lett.* **1982**, 49, 57-61.

28. For examples see: (a) Gomez, J.; Vasquez, L.; Baro, A.M.; Garcia, N.; Perdriel, C.L.; Triaca, W.E.; Arvia, A.J. *Nature* **1986**, 323, 612-4. (b) Vasquez, L.; Gomez, J.; Baro, A.M.; Garcia, N.; Marcos, M.L.; Gonzalez Velasco, J.; Vara, J.M.; Arvia, A.J.; Presa, J.; Garcia, A.; Aguilar, M. *J. Am. Chem. Soc.* **1987**, 109, 1730-33.

29. Itaya, K.; Sugawara, S. *Chem. Lett.* **1987**, 1927-30.

30. Liu, H.; Fan, F.; Lin, C.W.; Bard, A.J. *J. Am. Chem. Soc.* **1986**, 108, 3838-9.

31. Husser, O.E.; Craston, D.H.; Bard, A.J. *J. Electrochem. Soc.* **1989**, 136(11), 3222-29, and references therein.

32. Sonnenfeld, R.; Schneir, J.; Drake, B.; Hansma, P.K.; Aspnes, D.E.; *Appl. Phys. Lett.* **1987**, *50,* 1742-4.

33. (a) Schneir, J.; Hansma, P.K. *Langmuir* **1987**, 3, 1025-7. (b) Giambattista, B.; McNairy, W.W.; Slough, C.G.; Johnson, A.; Bell, L.D.; Coleman, R.V.; Schneir, J.; Sonnenfeld, R.; Drake, B.; Hansma, P.K. *Proc. Nat. Acad, Sci. USA* **1987**, 84, 4671-4.

34. Schneir, J.; Sonnenfeld, R.; Mart, O.; Hansma. P.K.; Demuth, J.E.; Hamers, R.J. *Appl. Phys. Lett.* **1988**, 63, 717-21.

35. Itaya, K.; Higaki, K.; Sugawara, S. *Chem. Lett.* **1988**, 421-4.

36. Lev, O.; Fan, F.; Bard, A.J. *J. Electrochem. Soc.* **1988**, 135, 783-4.

37. Morita, S.; Otsuka, I.; Okada, T.; Yokoyama, H.; Iwasaki, T.; Mikoshiba, N. *Jap. J. Appl. Phys.* **1987**, 26(11), L1583-5.

38. Wiechers, J.; Twomey, T.; Kolb, D.M.; Behm, R.J. *J. Electroanal. Chem.* **1988**, 248, 451-60.

39. Lustenberger, P.; Rohrer, H.; Christoph, R.; Siegenthaler, H. *J. Electroanal. Chem.* **1988**, 243, 225-35.

40. Trevor, D.J.; Chidsey, C.E.D.; Loiacono, D.N. *Phys. Rev. Lett.* **1989**, 62(8), 929-932.

41. Gewirth, A.A.; Bard, A.J. *J. Phys. Chem.* **1988**, 92, 5563-6.

42. Sonnenfeld, R.; Schardt, B.C. *Appl. Phys. Lett.* **1986**, 49(18), 1172-4.

43. Hottenhuis, M.H.J.; Mickers, M.A.H.; Gerritse J.W.; Van Der Eerden, J.P. *Surf, Sci.* **1988**, 206, 259-278.

44. Uosaki, K.; Kita, H. *J. Electroanal. Chem.* **1989**, 259, 301-8.

45. Green, M.P.; Richter, M.; Xing, X.; Scherson, D.; Hanson, K.J.; Ross, P.N.; Carr, R.; Lindau, I. *J. Microsc.* **1988**, 152(3), 823-9.

46. Christoph, R.; Siegenthaler, H.; Rohrer, H.; Wiese, H. *Electr. Acta* **1989**, 34(8), 1011-22.

Chapter 2

Currents in
Electrochemical STM Experiments

Introduction

The theoretical concepts needed to understand the operational principles of the scanning tunneling microscope have been well developed, at various levels of complexity, over the past few years.[1] A starting point for understanding the physics of electron tunneling may be found by considering Figure 1.[1a,2] The figure depicts the variations of potential with distance expected when two dissimilar metals are brought together in a vacuum so that the wave functions of the electrons in the metals may interact. In this manner a trapezoidal potential energy barrier is produced. For our purposes we can consider the two different metals to be the sample and the tip in an STM experiment. In the absence of barrier lowering that is due to image charge forces, the current for small biases (i.e. for $V_{bias} << \phi_1$ and ϕ_2) is given by the well-known Fowler-Nordheim relation (Eqn. 1).[1a,2]

$$I_t \propto \exp[-As\phi^{1/2}] \tag{1}$$

In the expression $A=(4\pi/h)(2m)^{1/2}$, where m is the effective mass of the electron in the tip/sample gap, s is the tip/sample separation, and ϕ is the average work function of the potential energy barrier $(\approx \frac{1}{2}(\phi_1+\phi_2))$. The most important feature of the tunneling process described by Equation 1 is that the current, at a given bias, is exponentially dependent on the distance between the two metals. Using the free electron mass (giving A = 1.025 $eV^{-1/2}Å^{-1}$), and a typical average work function of 4 eV, Eqn. 1 predicts that the tunneling current decreases by approximately an order of magnitude when s is increased by only 1 Å. It is this exponential dependence that enables tunneling gaps of c.a. 5-10 Å to be formed and stabilized with the use of negative feedback control techniques and piezoelectric materials (more on this subject in Chapter 3). If a constant current is maintained while the tip is rastered across the metal surface, then contours of constant $s\phi^{1/2}$ will be traced by the apex

of the tip. If the metal surface possesses a spatially uniform ϕ, then the tip/sample spacing (s) will remain constant during the rastering. By recording the changes in the height of the tip as the tip is rastered and s is kept constant, an image of the surface may be obtained. The topography is measured by determining the voltage that must be supplied to the Z-piezoelectric transducer in order to maintain a constant tip/sample spacing.

Though greatly simplified, the description offered by Eqn. 1 contains the essential features needed to understand STM. Tersoff and Hamann[1c] have developed a more complete theoretical treatment that invokes Bardeen's transfer Hamiltonian approach[3] to describe tunneling between a model probe tip and a sample surface.[1b] In this treatment the tunneling current is found to be proportional to the local density of states at the Fermi level of the sample at the position of the tip. Thus, if a constant current is maintained as the tip is scanned, contours of constant local density of states are traced. For metal surfaces, the Tersoff/Hamann theory predicts results similar to those expected from Eqn. 1. For semiconductor surfaces, however, electronic structure effects are also expected to play an important role in the resultant images. Recent STM experiments on GaAs[4] and Si[5] surfaces have confirmed these predictions.

Additional considerations arise when the STM experiment is performed in an electrochemical environment. Firstly, when the tip and sample are immersed in a condensed phase, the material of the tip/sample gap must be considered to be a polarizable medium. It is reasonable to expect that the high electric fields present in the tunneling gap (c.a. 10^7 V/cm) may perturb the arrangement of weakly adsorbed or nonadsorbed dipolar species under the tip. Secondly, the medium provides a new means by which electrons can flow between the tip and the sample. In analogy to recent demonstrations found in the electron transfer literature,[6] one can envision a through bond contribution to the normally measured through space tunneling current. Such a mechanism could explain STM's unexpected ability to image Langmuir-Blodgett films,[7] polymer layers,[8] and DNA strands.[9]

A third effect, however, is typically of overriding concern in an *in situ* STM experiment. In an electrochemical environment, the tip/sample bias that is necessary for electron tunneling can also drive heterogeneous charge transfer reactions between the solution-contacted portions of the tip and the sample. This faradaic current will act in parallel to the normally measured tunneling current, and the measured sum may not exhibit the expected exponential dependence on tip/sample separation.[10] For example, in our laboratory, we have found that feedback control of the tunneling gap is lost if the faradaic current (I_f) is of comparable magnitude to the tunneling current (I_t). Additionally, the bias dependence of the measured current will be a convolution of the bias dependences of the two components. As a result, even when the tip/sample gap can be stabilized, the interpretation of either work function (dI/dS) or local density-of-states (dI/dV) measurements is not straightforward.

The interpretation of STM-derived data is simplified if the faradaic component of the total tip/sample current is small in comparison to the tunneling current component. The tip/sample biases at which this situation may be achieved become progressively more restricted as the STM is operated in electrolytic solutions containing 1) pure liquids and electrochemically inert components, 2) redox species that undergo a phase change with a change in oxidation state, or 3) kinetically reversible or quasi-reversible species.[10] Because the faradaic current between the tip and the sample increases monotonically with the amount of tip-metal exposed to solution, and the tunneling current flows only through a single atomic-scale asperity on the tip, the faradaic component can be selectively reduced in all cases by coating the shaft and apex of the STM tip with insulating layers.[10] For this reason virtually all *in situ* STM experiments performed to date have employed tips that have been coated with insulating materials (e.g., glass, or lacquer) so that less than ca 10^{-4} cm^2 of metal is exposed to solution (*vide infra*). The reductions in faradaic current afforded by tip insulation techniques vary with the amount of exposed metal area, the proximity of the tip to

the sample, and the possible electrochemical reactions. To elucidate these factors further we can consider the three distinct cases of electrochemical interest in more detail.

Case I: Pure Liquids and Inert Electrolytes

In a pure electrolytic solution (e.g., 0.1 $\underline{M}$ NaCl), faradaic current will not flow if the tip/sample bias is less than the value necessary to drive irreversible solvent decomposition or electrolyte reactions at both the tip and the sample. The available bias window (ΔE_t) can be easily calculated from the electrochemical potential data for the solvent/electrolyte system under study.[10a] Thus, in theory, it should be possible to image surfaces in aqueous salt solutions with STM at biases as large as 1.2 V. In practice, however, it is difficult to obtain solvents and electrolytes with sufficient purity that faradaic currents are not observed between the tip and the sample at appreciable biases (ΔE_t > 10 mV). For example, Sonnenfeld and Hansma[11] used glass-coated Pt-Ir tips, yet still found it necessary to use a large current setpoint of 50 nA (with a ΔE_t = 100mV, tip negative) to obtain the first atomic resolution images of highly ordered pyrolytic graphite (HOPG) under water. The faradaic portion of the total current was determined to be 19 nA by measuring the current that remained when the tip was withdrawn from tunneling range.[11] In this work it was tacitly assumed that the faradaic current remained constant with interelectrode separation.

Case II: Redox Processes Accompanied by a Phase Change: Bias Polarity Considerations

Distinctly different STM imaging considerations exist in the presence of a redox couple possessing one member that is insoluble.[10] Such conditions are found in several recent STM studies of electrodeposits on conducting surfaces.[12] The work of Sonnenfeld and Schardt,[12a] which dealt with the *in situ* imaging of silver deposits on HOPG, is a particularly illustrative example. An idealized diagrammatic representation of the

electrochemical reactions and potentials relevant to the work is shown in Figure 2. Silver deposits were formed by sweeping the potential of the HOPG electrode to potential values more negative than the electrode's rest potential in the 50 m$\underline{M}$ AgClO$_4$ solution (ca +0.68 V vs. SHE).[12a] Water was oxidized at a counter electrode to complete the electrochemical circuit. Analysis of the electrochemical system reveals that during the deposition the sample was poised somewhere along the bold solid line in Figure 2, while the counter electrode was positioned on the unbolded solid line. Once the desired deposition was performed, the counter electrode was disconnected from the circuit and the surface was imaged with STM. In accordance with the analysis presented here, beautiful images of the deposited Ag were obtained with a bias of +0.100 V (tip positive).[12a] Glass-coated tips were employed and the faradaic current was measured to be < 0.1 nA when the tip was retracted 1 μm from the surface. With biases larger than $\approx$0.14 V, it is expected that the same electrochemistry that was responsible for the initial silver deposition would occur between the sample and the tip. In this case oxygen evolution would occur at the tip, instead of the counter electrode, and the tip's potential would be poised on the unbolded solid of Fig. 2. Feedback control of the tunneling gap would be thwarted under these conditions, and atomic-scale imaging would be impossible.

With the opposite tunneling junction polarity (tip negative), imaging would be impossible at all bias magnitudes. In this scenario metal deposits on the sample would be oxidized and become soluble and metal ions in solution would be plated onto the tip. The tip potential would now fall somewhere on the bold solid line in Figure 2, while the sample potential would lie on the dashed line. Because complementary halves of the same electrochemical reaction would be driven at both electrodes, the faradaic current is expected to be unmanageably large at all appreciable negative biases. The problem is exacerbated by thin-layer faradaic current enhancements (vide infra) and the changes in tip geometry that would attend metal deposition.

Case III: Reversible Redox Species

The most demanding case of electrochemical importance is when reversible or quasi-reversible redox species are present.[10] Such conditions are found in a variety of situations of interest to electrochemists. For example, while studying the properties of a semiconducting electrode, both halves of a redox couple should be present to establish a well-defined solution potential and properly poise the Fermi level of the semiconductor. *In situ* observations of corroding metal surfaces must be carried out in solutions containing concentrations of metal ions. Also, methods that allow STM operation in the presence of reversible redox species will certainly be useful in facilitating imaging in the presence of electroactive impurities.

If the redox species exhibit reversible kinetic behavior at the tip and sample, then a situation similar to that found while attempting to image the Ag deposits of Case II with negative tip polarity will be found at all appreciable biases and at both polarities. In this case oxidized species may be reduced at the tip while reduced species are oxidized at the sample. In this situation, however, the newly reduced species does not form a deposit and may migrate back to the sample to participate in the cycle once again. Thin-layer current enhancements[13] (*vide infra*) will compound the problem. Unlike the Ag deposition experiment, faradaic currents are expected to be problematic at both bias polarities.

In the presence of quasi-reversible redox couples, it may be possible to access a bias window in which STM images can be obtained. In this case a significant overpotential, η, ($\eta = E - E_{rev}$) may be associated with the generation of faradaic current at one or both of the electrodes.[14] A given faradaic current will flow only when the tip/sample bias exceeds the sum of the anodic and cathodic kinetic overpotentials ($\eta_a + \eta_c$). At potentials less than this sum, it should be possible to stabilize feedback control and obtain STM images. However, these capabilities have not yet been demonstrated, and all STM images of

solution-covered surfaces obtained, except for those presented in this thesis and in related publications, fall under Class I or II conditions.

Magnitudes of Faradaic Currents in Electrochemical STM

The amount of exposed metal remaining after tip insulation is an important quantity for evaluating faradaic currents in electrochemical STM. This parameter can be assessed for a given insulated tip with the expression that describes the diffusion-limited current to a hemispherical ultramicroelectrode (UME), Equation (2).[15]

$$I_{lim} = 2\pi nFDCR \tag{2}$$

In this expression n is the number of electrons involved in the charge transfer reaction, F is the Faraday (96480 C/mol e⁻), D and C are the diffusion coefficient and concentration, respectively, of the electroactive species, and R is the radius of the exposed metal hemisphere. It can be seen from Equation (2) that for a typical value of D ($\approx 1 \times 10^{-5}$ cm^2/s) the diffusion-limited current to a r = 10μ UME will be 1 nA (and thus comparable to the tunneling current) for an electroactive species concentration of ≈ 0.16 mM. It is important to note that this calculation is not directly applicable to an UME close to a planar surface, as is the case in an STM experiment, since Equation (2) rests on the assumption that the diffusion layer around the UME is at least 2R in thickness.[15]

Even with insulating procedures faradaic currents can still be problematic. The proximity of the tip to the sample during an *in situ* STM investigation permits thin-layer currents to become an important mechanism for faradaic charge transport.[13] In contrast to the UME treatment described above, the faradaic current to an electrode in a thin-layer cell is not governed by diffusion of electroactive species from the bulk electrochemical environment. If both forms of a redox couple are initially present, then complementary

electrochemical reactions are driven at each electrode and the faradaic current should

increase with decreasing interelectrode spacing. If the diffusion coefficients of the oxidized

and reduced species and their concentrations are assumed to be equal, then the diffusion

limited thin-layer current between two planar electrodes of area A, separated by an

interelectrode distance of d, is described by Equation (3):[13]

$$I_{lim} = 2nFDCA/d \quad \text{(with } C_{ox} = C_{red} = C)} \tag{3}$$

If we assume that the confined solution volume does not mix with the bulk solution,

and that the current flow is perpendicular to the electrode surfaces, then Eqn. (3) can also be

used to estimate the thin-layer faradaic current when an insulated STM tip approaches a

conducting substrate. At typical tunneling distances (ca 10 Å), and with a 1 μm radius disk of

metal at the tip apex, faradaic currents might be comparable in magnitude to the tunneling

current (ca 1 nA) for electroactive impurities at concentrations as low as 1 $\mu\underline{M}$.[13] The

applicability of Eqn. (2) at somewhat larger tip/sample spacings has been tentatively

established in our laboratory for glass-coated Pt-Ir tips and will be discussed further in

Chapter 4.

From considerations of a typical tip geometry (see Chapter 5), it may be more

reasonable to consider the exposed metal area to be distributed in a hemisphere. Recent

theoretical calculations[16] involving the same assumptions that were made above for the

disk geometry predict that the diffusion-limited, thin-layer current between a hemispherical

electrode and a planar electrode increases logarithmically, rather than linearly, with the

reciprocal of the electrode spacing (Eqn. 4).

$$I_{lim} = 2\pi nFDCR \ln(1 + R/d) \tag{4}$$

According to these calculations a limiting thin-layer current of 1 nA will flow between a 1 μm radius hemisphere and a large conducting plane, separated by 10Å, when the concentration of redox active species is 0.24 mM.[16] For comparison, a concentration 6.9 times larger would be needed for a 1 nA current if the same electrode behaved as an isolated UME.[15] Also, considerably larger concentrations may be tolerated in this case, since most of the exposed metal of the hemisphere is relatively distant to the planar electrode. Though these calculations have not been experimentally verified, they support the generally accepted idea that the faradaic current between the tip and sample should increase from the value predicted from the UME formalism (when d >> 2R)[15] to a thin-layer dominated value at small interelectrode spacings (d << 2R).[13]

In the above discussions of currents in thin-layer cells, we have tacitly assumed that the limiting currents are reached at small tip/sample biases. Theory for a thin-layer cell formed from two planar electrodes containing equal concentrations of redox species (with equal diffusion coefficients) predicts that only half of the expected limiting current is reached with electrode potential differences of 2RTln(3)/nF $\approx$ 56.4 mV (for n=1).[13] Thus, at biases smaller than this value, faradaic currents should be restricted to < 0.5 nA in the case of reversible redox species and with the concentrations and electrode sizes mentioned above. Equivalently, the condition that $I_f < I_t$ could be fulfilled with somewhat larger electrodes, or higher redox species concentrations, at biases less than $\approx$ 56 mV. Even larger tip/sample biases could be accessed if kinetic limitations begin to govern the current transport. Such conditions are found when the rate constant for mass transport ($\approx$ D/d) is exceeded by the electron transfer rate constant (k^o).[13] For the thin-layer cell with the disk-shaped electrode, values of k^o would have to be larger than $\approx$ 100 cm/sec for the faradaic current to be governed solely by mass transport.

Within tunneling distances the estimates given by considering thin-layer cell configurations are probably inappropriate. At interelectrode distances approaching 10Å, the

electrical double layers of the electrodes, as estimated from the expected Debye lengths, will overlap for univalent electrolyte concentrations less than 0.4 $\underline{M}$.[14] Consequently, electrostatic effects may modify the composition of the solution in the region of the tip/sample gap. Also, if solution species are preferentially adsorbed onto either the tip or the sample, then a surface concentration, rather than a bulk concentration, should be considered.[17] Moreover, it is not clear that a macroscopic transport description, which assumes the existence of a large ensemble of species, is applicable at such small values of d. Clearly, the faradaic current does not become infinite at d=0 as the thin-layer formalisms suggest.

Managing Faradaic Currents for *In Situ* STM Investigations

STM studies in electrochemical systems are generally performed by either nulling or reducing the faradaic currents to manageable levels. As demonstrated by Sonnenfeld and Hansma,[11] this task is simplified by performing the investigation under conditions that conform to Case I conditions. Consequently, most electrochemical STM studies have focussed on imaging HOPG[18] and metal[19] surfaces in contact with acid or salt solutions (typically ≤ 0.1 $\underline{M}$). Tip insulation was recognized as being crucial in all of these experiments, and various insulation techniques were employed to limit the area of exposed metal . The biases on the tip (relative to the sample) were typically in the range + 90 mV to - 50 mV to avoid currents that were due to faradaic processes. In several of these investigations[18a,b;19a,b] the magnitude of the faradaic current was measured while the tip was not in tunneling range. In these cases the faradaic current was always less than 10% of the total current, and reported values ranged from 0.02 - 0.2 nA.

The work of Lustenberger et al.[18c] is different from these studies in that epoxy-coated tantalum tips with relatively large exposed metal areas (10^4 to 10^5 μm^2) were employed. The tips were maintained at potentials (-500 mV to 0 V *vs.* SCE) that resulted in

the smallest faradaic currents (< 10 pA) through the tip in the aqueous 0.1 $\underline{M}$ NaClO$_4$

solution. The authors reported that a thin oxide layer should be present on the tip within this

potential range. The faradaic current was evidently not overwhelming while the tip was in

tunneling range since images of HOPG were obtained, at nanometer resolution, with

tunneling currents as low as 150 pA. Wiechers et al.[19e] have used similar techniques to

poise the potential of a tungsten tip during their investigations of Cl⁻ adsorption on Au(111)

surfaces. However, their results could not be scrutinized with respect to faradaic currents,

since tunneling and faradaic current values were not reported. One possible drawback of

this approach is that a change in the potential of the sample electrode results necessarily in

a change in the tip/sample bias. Consequently, it will be difficult to vary the two quantities

independently in this configuration.

Several other recent experimental efforts have dealt with imaging metal

electrodeposits on HOPG[12a] and metal[12b-e] surfaces. Potential control of the sample

surface was used in these experiments to deposit and strip metal monolayers and

multilayers. In some instances potential control of the substrate was maintained while the

surfaces were imaged with STM.[12c-e] Salts of metal ions were included into the solutions

in concentrations ranging from 1 - 50 m$\underline{M}$ and, therefore, these images were obtained under

Case II type conditions (*vide supra*). The residual faradaic currents, as measured with the tip

out of tunneling range, ranged from 0.1 nA to 5 nA. An extremely low value of 2 pA was

achieved in experiments by Christoph et al.[12e] by employing the methodologies introduced

in the publication of Lustenberger et al.[18c] (*vide supra*). Considerable care was taken to

employ only high-purity materials and solutions in this more recent work. Uosaki and

Kita[12c] also poised their Pt-Ir tip +500 mV *vs.* a Pt pseudoreference to investigate copper

deposition on polycrystalline Pt and observed faradaic currents less than 0.1 nA. As in the

Case I experiments discussed above, all of these Case II investigations utilized tip-insulation

strategies.

Summary

The above discussions of several representative Case I and Case II type of studies reveal that to date, two general methods for managing faradaic currents have emerged. One approach involves maintaining the tip at a fixed potential *vs.* a reference electrode so that the faradaic currents through the tip are minimal in bulk solution. The behavior of the faradaic component as the tip approaches the sample has not yet been addressed in these types of investigations, but in cases where high-purity solutions and materials have been used, the faradaic currents while tunneling have not been problematic. As mentioned earlier, however, this approach is somewhat restrictive in that the tip/sample bias and the sample potential cannot be varied independently. Also, this technique is not expected to be useful for imaging surfaces under Case III conditions.

The second general approach involves attempts to reduce the amount of exposed metal area on the tip with insulating coatings. For the Case I and Case II type of studies discussed above, the exposed tip area typically ranged from 50 to 10^4 μm^2. In one instance[18a] the exposed metal area was reduced to 10^{-4} μm^2 (10^4 $Å^2$) by employing an insulating varnish. To date, however, estimates of exposed metal areas on STM tips have been made while the tip is withdrawn from the sample surface. Consequently, the role of thin-layer currents has not been addressed. Reducing the exposed tip areas further, so that only the minimum amount of metal necessary for tunneling remains exposed, should minimize faradaic currents and allow the tip and sample potentials to be arbitrarily selected for all types of investigations, including those that conform to Case III conditions. Two tip-insulating procedures that employ thin layers of either glass or polymer and evidently achieve this goal have recently been developed in our laboratories.[10] After coating, and a subsequent "field-emission" process performed in the tunneling microscope, the amount of exposed metal area on the glass-coated tips can apparently be less than 100 $Å^2$. With these

methods tip/sample faradaic currents are less than 10 pA and are small in comparison to typical tunneling current setpoints (ca 1 nA), even in the presence of high concentrations of reversible redox species and at large biases (ca 1 V).[20] These procedures and the capabilities of the tips that result are discussed in Chapter 4.

References

1. (a) Hansma, P.K.; Tersoff, J. *J. Appl. Phys.* **1987**, 61(2), R1-23. (b) Feuchtwang, T.E.; Cutler, P.H. *Phys. Scripta.* **1987**, 132-40. (c) Tersoff, J.; Hamann, D.R. *Phys. Rev. B.* **1985**, 31(2), 805-13.

2. (a) Binnig, G.; Rohrer, H.; Gerber, Ch.; Weibel, E. *Appl. Phys. Lett.* **1982**, 40(2), 178-80. (b) Fowler, R.H.; Nordheim, L. *Proc. R. Soc. London A* **1928**, 119, 173-81.

3. Bardeen, J. *Phys. Rev. Lett.* **1961**, 6, 57.

4. Stroscio, J.; Feenstra, R.M.; Fein, A.P. *Phys. Rev. Lett.* **1987**, 58(16), 1668-71.

5. Tromp, R.M.; Hamers, R.J.; Demuth, J.E. *Science* **1986**, 234, 304-9.

6. (a) Mcclendon, G. *Acc. Chem. Res.* **1988**, 21, 160-167. (b) Purugganan, M.D.; Kumar, C.V.; Turro, N.J.; Barton, J.K. *Science* **1988**, 241, 1645-49.

7. (a) Smith, D.P.E.; Bryant, A.; Quate, C.F.; Rabe, J.B.; Gerber, Ch.; Swalen, J.D. *Proc. Natl. Acad. Sci. USA* **1987**, 84, 969. (b) Horber, J.K.H.; Lang, C.A.; Hansch, T.W.; Heckl, W.M.; Mohwald, H. *Chem. Phys. Lett.* **1988**, 145, 151.

8. (a) Albrecht, T.R.; Dovek, M.M.; Lang, C.A.; Grutter, P.; Quate, C.F.; Kuan, S.W.; Franck, C.W.; Pease, R.F.W. *J. Appl. Phys.* **1988**, 64(3), 1178-84.

9. (a) Beebe, T.P.; Troy, E.W.; Ogletree, D.F.; Katz, J.E.; Balhorn, R.; Salmeron, M.B.; Siekhaus, W.J. *Science* **1989**, 243, 370-2. (b) Lee, G.; Arscott, P.G.; Bloomfield, V.A.; Evans, D.F. *Science* **1989**, 244, 475-7.

10. (a) Dovek, M.M.; Heben, M.J.; Lewis, N.S.; Penner, R.M.; Quate, C.F. in *Molecular Phenomena at Electrode Surfaces: ACS Symposia Series*, **1988**, 378, 174-201. (b) Heben, M.J.; Dovek, M.M.; Lewis, N.S.; Penner, R.M.; Quate, C.F. *J. Microsc.* **1988**, 152(3), 651-61.

11. Sonnenfeld, R.; Hansma, P.K. *Science* **1986**, 232, 211-13.

12. (a) Sonnenfeld, R.; Schardt, B.C. *Appl. Phys. Lett.* **1986**, 49(18), 1172-4. (b) Hottenhuis, M.H.J.; Mickers, M.A.H.; Gerritsen, J.W.; Van Der Eerden, J.P. *Surf, Sci.* **1988**, 206, 259-278. (c) Uosaki, K.; Kita, H. *J. Electroanal. Chem.* **1989**, 259, 301-8. (d) Green, M.P.; Richter, M.; Xing, X.; Scherson, D.; Hanson, K.J.; Ross, P.N.; Carr, R.; Lindau, I. *J. Microsc.* **1988**, 152(3), 823-9. (e) Christoph, R.; Siegenthaler, H.; Rohrer, H.; Wiese, H. *Electr. Acta* **1989**, 34(8), 1011-22.

13. (a) Hubbard, A.T.; Anson, F.C. in *Electroanalytical Chemistry*; Bard, A.J., Ed., Vol. 4; Marcel Decker: New York, 1971, 129-211. (B) Hubbard, A.T. *CRC Critical Reviews in Analytical Chemistry* **1973**, 3, 201-242. (c) Anderson, L.B.; Reilley, C.N. *J. Electroanal. Chem.* **1965**, 10, 295-305.

14. Bard, A.J.; Faulkner, L.R. *Electrochemical Methods*; John Wiley & Sons: New York, 1980.

15. Galus, Z. *Fundamentals of Electrochemical Analysis*; Halsted Press: New York, 1976; Chapter 4.

16. Davis, J.M.; Fan, F.; Bard, A.J. *J. Electroanal. Chem.* **1987**, 238, 9-31.

17. Seibold, J.D.; Scott, E.R.; White, H.S. *J. Electroanal. Chem.* **1989**, 264, 281-9.

18. (a) Gewirth, A.A.; Bard, A.J. *J. Phys. Chem.* **1988**, 92, 5563-6. (b) Itaya, K.; Sugawara, S. *Chem. Lett.* **1987**, 1927-30. (c) Lustenberger, P.; Rohrer, H.; Christoph, R.; Siegenthaler, H. *J. Electroanal. Chem.* **1988**, 243, 225-35.

19. (a) Trevor, D.J.; Chidsey, C.E.D.; Loiacono, D.N. *Phys. Rev. Lett.* **1989**, 62(8), 929-32. (b) Lev, O.; Fan, F.; Bard, A.J.; *J. Electrochem. Soc.* **1988**, 135, 783-4. (c) Morita, S.; Otsuka, I.; Okada, T.; Yokoyama, H.; Iwasaki, T.; Mikoshiba, N. *Jap. J. Appl. Phys.* **1987**, 26(11), L1853-5. (d) Itaya, K.; Higaki, K.; Sugawara, S. *Chem. Lett.* **1988**, 3, 421-4. (e) Weichers, J.; Twomey, T.; Kolb, D.M.; Behm, R.J. *J. Electroanal. Chem.* **1988**, 248, 451-60.

20. Heben, M.J.; Penner, R.M.; Lewis, N.S.; Dovek, M.M.; Quate, C.F. *Appl. Phys. Lett.* **1989**, 54(15), 1421-3.
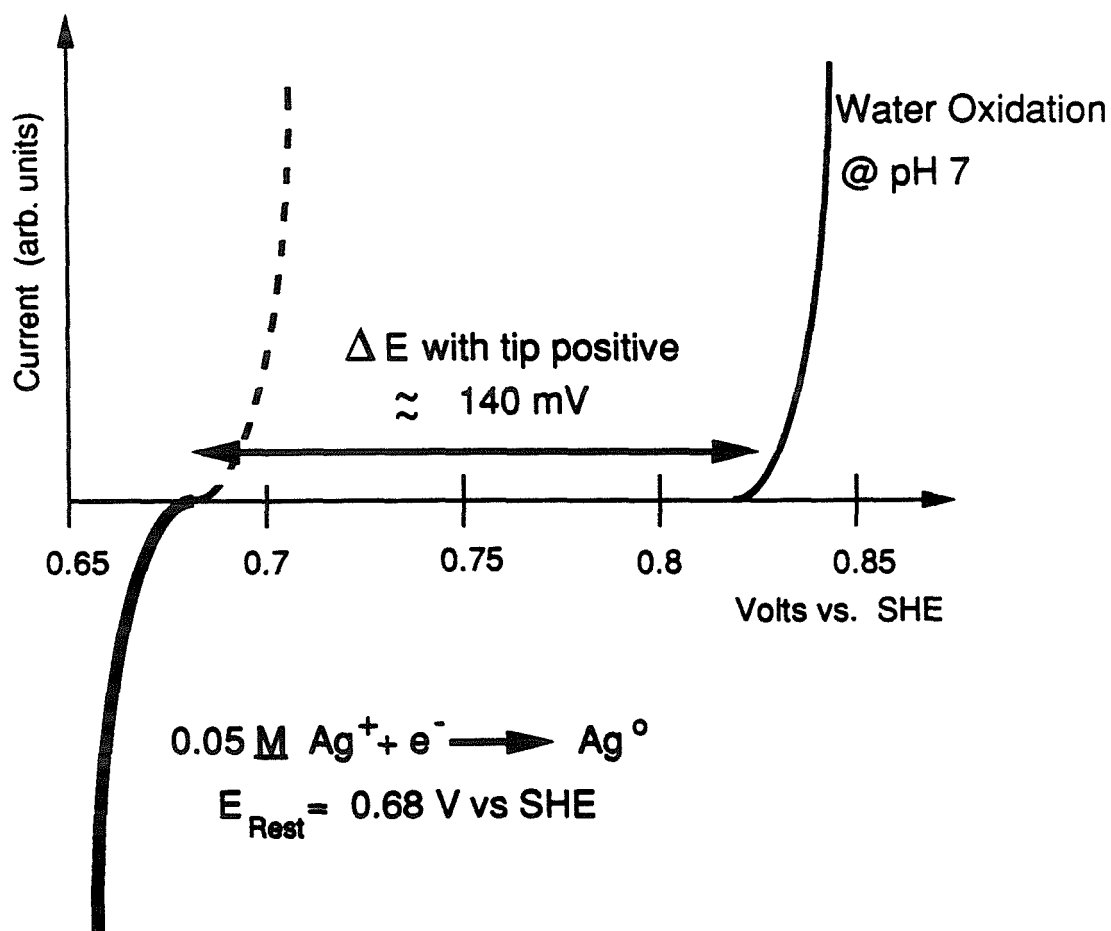
Figure 1:

Diagram of energetics for electron tunneling between two metals in vacuum.
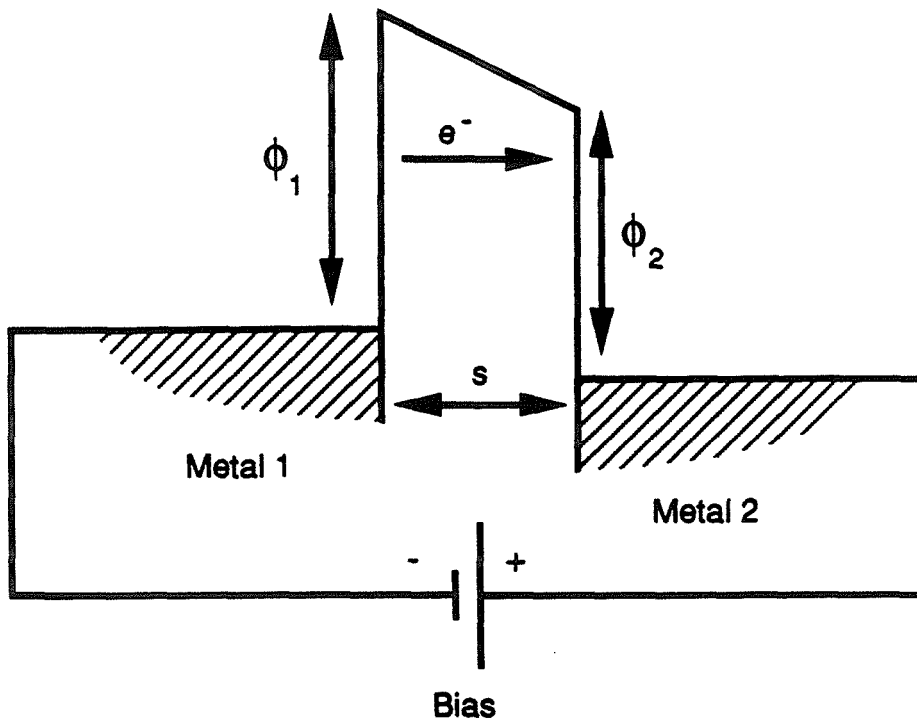
Figure 2:

Hypothetical current/potential relationships for imaging Ag deposits in the presence of Ag^+

ions in an aqueous solution (pH 7). The intersections of the current curves with the

potential axis represent thermodynamic values derived from Ref. 12a. The shapes of the

curves are arbitrary and do not contain kinetic information. Similar energetic

considerations may be found for all Case II type STM investigations (see text).

Expected Current/Potential Behavior for Imaging

Ag Deposits in the Presence of Ag$^+$

Water Oxidation

@ pH 7

Δ E with tip positive

$\approx$ 140 mV

Current (arb. units)

0.65   0.7   0.75   0.8   0.85

Volts vs. SHE

0.05 $\underline{M}$ Ag$^+$+ e$^-$ $\longrightarrow$ Ag^o

E$_{Rest}$ = 0.68 V vs SHE

Chapter 3

Design of a Scanning Tunneling Microscope
for the Investigation
of Electrochemical Systems

Introduction

Advances in instrument design have facilitated the growth of STM as an important surface analytical tool. In this chapter we will consider briefly some of the instrumental developments that have allowed atomic resolution imaging to become routine. We will then focus on the new design considerations that arise when attempting to image liquid-covered surfaces, and will give a brief accounting of some of the more important historical developments in the design of the electrochemical STM. The chapter will conclude with a discussion of the unique design features and capabilities of the electrochemical STM used in our laboratory. Images obtained with our microscope operating in air will also be presented.

The critical aspects of STM design deal with the formidable task of separating detected spatial variations of electronic wave functions, and signals derived therein, from spurious mechanical, acoustical and thermally derived noise.[1] Stated in another way; the task is to isolate and control the vertical and lateral confines of an electron tunneling current. Important developments facilitating this goal include the introduction of magnetic levitation,[2] eddy current damping,[3,4] and spring-supported staging[4] for vibration isolation. Simplicity of design was gained through the realization that stacked plates separated by lossy elastomers could achieve similar ends.[5,6] High-speed imaging techniques, employable on relatively smooth surfaces, were found to yield an improved signal-to-noise ratio[1,7] and opened the real-time imaging domain. The invention of the tube scanner by Binnig and Smith[8] further reduced the complexity of microscopes, and since mechanical resonances of the tube occur at higher frequencies (ca 8 kHz), the tube scanner allows still higher tip speeds. Throughout these design evolutions the most important consideration has remained the need for compactness and rigidity in the microscope body.

The design criteria for an *in situ* electrochemical STM include the concerns outlined above as well as several needs peculiar to an electrochemical environment. Sonnenfeld and Hansma[9] constructed the first STM designed to image solution-covered surfaces, and their work highlighted two important design considerations. Firstly, the microscope construction should enable the tip/sample gap to be easily flooded with the solution of interest. The first solution microscope was designed such that the tip and sample were immersed in solution, while the piezoelectric scanning elements remained above the solution level. However, this design also allowed the solution to contact other potentially reactive structural components of the microscope. In an ideal *in situ* microscope, the solution should contact only the tip, sample, auxiliary electrodes (if employed) and chemically and electrically inert materials.

The importance of tip insulation is the second significant solution microscope design feature recognized by Sonnenfeld and Hansma.[9] As discussed in Chapter 2, faradaic currents will always be present between the tip and sample in all but ideally pure solutions. If these currents are of the same magnitude as the tunneling current, then feedback control will be difficult to maintain. Several strategies have been employed to circumvent problems associated with faradaic current components (see Chap. 2). Our efforts to reduce faradaic currents by tip-insulation methods will be explained in more detail in Chapter 4.

The first electrochemical STM to operate with a single tube scanner was also developed by Sonnenfeld and coworkers.[10] This STM also incorporated a novel fluid transfer line that provided for the delivery and removal of solution from the tip/sample gap. This microscope required a smaller volume of solution and, consequently, thermal drift problems caused by evaporative loss of solution were significantly reduced. A noteworthy advance in microscope design was provided by Morita et al.[11] and separately by Itaya et al..[12] By switching between two independent sets of circuitry, they were able to perform STM investigations and conventional three-electrode voltammetry in the same instrument. Lev et al.[13] demonstrated that surfaces could be imaged while under potentiostatic control

by employing a battery and a Pt "flag" electrode to poise the potential of a nickel sample electrode away from the solution rest potential.

The microscope used for the research presented in this thesis has been constructed with all of the aforementioned design features in mind. In addition, several unique aspects of the microscope make it well suited for studies of the solution-covered surfaces. Noteworthy features of the instrument include a modular design for rapid tip and/or sample exchange, inert components contacting the electrolyte, and stepper motor driven approach mechanics that enable remote operation. Additionally, the low-noise control electronics utilized in this instrument are versatile and allow the microscope to be operated in several different modes. This microscope is significantly different from our earlier version[14] and, consequently, will be discussed in detail here.

Design of the Microscope

Our electrochemical STM consists of two major parts: the microscope body and the control electronics. The microscope body is composed of the base and the approach mechanics, and its structure is schematically shown in Figure 1. The base of the tunneling microscope supports the approach mechanics, provides for sample mounting, and confines a small volume (ca 2-3 ml) of the solution of interest in the region of the tip/sample gap. The approach mechanics supports the piezoelectric scanner and the tip, and facilitates coarse formation of the tunnel junction. The control electronics detects and provides all of the electronic signals that are needed for maintaining and deciphering an electron tunneling current. These parts and other ancillary portions of the microscope are discussed below.

The base of the microscope

In order to ensure compatibility with common electrochemical solvents, the base of the tunneling microscope was fabricated from quartz. Quartz was found to be superior to

Pyrex, which we employed in an earlier design,[14] since time-dependent elasticity effects[15] were not displayed by the quartz. Three equally spaced dimples were ground into the uppermost surface of the quartz base to provide positioning points for the approach mechanics (*vide infra*). A hole along the axis of the cylindrically symmetric quartz piece allowed quartz sample holders to be mounted in the microscope. Another hole was drilled through the wall of the base and was capped with an optical flat. This viewing hole allowed the initial positioning of the tip to be observed with an optical stereoscope. The quartz base was anchored to a brass support by two nylon screws (Fig. 1).

The brass support was also cylindrical and provided several important functions (Fig. 1). Three buckle fasteners on the brass piece facilitated mounting of the approach mechanics. The interior of the brass piece was hollowed out so that the current preamplifier could be located under, and very close to, the tip/sample junction. This arrangement successfully minimized the electronic noise inputted to the preamplifier. A threaded hole along the axis of the brass support accommodated a threaded Delrin plug that was used to secure a sample holder in place. By tightening the Delrin plug, an O-ring compression seal could be obtained between the quartz sample holder and the quartz base (Fig. 1). A seat for the O-ring was cut into the bottom of the quartz base to achieve simultaneously a solution tight seal and a quartz-to-quartz mating.

It is important to note that the considerable weight of the brass support (≈ 1.25 kg) constituted over 65% of the total weight of the fully assembled microscope. Consequently, the brass piece served to lower the center of mass of the instrument and desensitized the microscope to environmental vibrational noise. Further vibration isolation was achieved with the use of an arrangement similar to that described by Binnig and coworkers.[5,6] Stacked brass plates separated by silicone rubber feet were found to yield excellent isolation with minimum space and machining requirements.

Sample holders

Sample holders were made of quartz and were shaped as depicted in Figure 1. Samples were cemented to the top of the pedestal with silver paint, and electrical connections were made via a capillary opening. After mounting, the edges of the sample and the Ag paint were generally insulated from solution with epoxy. Sample holders were firmly mounted in place with the methods described above. The sample wire was enclosed by a grounded shield, and travelled to the current preamplifier.

The approach mechanics

The second major part of the microscope body is the approach mechanics for positioning the tip (Fig. 1). In our design, the mechanics was held in position on the quartz base by use of symmetrically arranged springs. As indicated in Figure 1, the spring tension was applied between the buckle fasteners on the base and small bolts that protruded from the uppermost stainless-steel plate of the approach mechanics. Three stainless-steel rods were press-fit into this steel plate and mated with the dimples in the quartz base. These facilities enabled the approach mechanics to be rapidly and rigidly mounted on the microscope base.

The three steel rods also functioned as guidance rails for a second, lower stainless steel plate. This second plate, which was spring-loaded to the first by two springs, carried the piezoelectric tube scanner and the tip. The two springs were positioned to achieve an asymmetric loading for improved stability in the plane of the sample. To obtain a controlled approach of the tip to the sample, the second plate was pushed toward the sample by a stepper motor that was anchored to the upper plate.

The piezoelectric scanner and tip mounting

The single tube piezo was constructed from PZT-5H material,[16] and was of the design and dimensions (0.5" long X 0.25" O.D. X 0.020" wall) described by Binnig and Smith.[8] Piezo scanners formed with these specifications have been reported to possess sensitivities of 50 Å/V in X, Y and Z directions.[8,17] However, our piezo tube was protected from solution by a sheath of heat-shrink-type Teflon tubing and was epoxied on a MACOR block. Additionally, a brass chuck that was cemented onto the end of the piezo tube allowed tips to be secured in place with a set screw. Consequently, the motion of our piezo tubes was somewhat hindered and these tubes typically displayed sensitivities between 25 and 50 Å/V. These values were determined for each piezo tube by imaging the well-known surface of highly ordered pyrolytic graphite. Because constant-height imaging techniques (*vide infra*) were generally employed, absolute calibration in the Z direction was not typically required. However, it is reasonable to expect that our construction methods should not appreciably restrict the motion of the tube in the Z direction. Interferometric measurements performed on one fully assembled tube with a commercially available distance measurement system[18] (with a resolution of ca 80 nm) yielded an average value for the Z response of 52 Å/V. Therefore, when required, we have adopted a value of 50 Å/V for the response of the tube in the Z direction. A detailed view of the scanner construction is also shown in Figure 1.

Stepper motor drive electronics

Circuitry was constructed in order to drive the stepper motor with either pulsed or DC voltages. A detailed schematic of the circuitry may be found in the Appendix to this chapter. Under DC operation, the tip could be translated at rates up to 0.2 mm/s either towards or away from the sample. This capability was found to be extremely useful in coarse tip/sample positioning. In the pulse mode, the stepper motor could be driven either with a

train of pulses or with a single pulse. The pulses were of 10 ms duration and consisted of arbitrarily programmable voltages between the limits of 5 to 8 V.

The amount of tip travel in response to a single voltage pulse was found to be a function of the stiffness of the springs employed to load the stepper motor. By appropriate adjustment of the loading and the pulse voltage, it was found that the steel plate that carried the piezo and tip could be reproducibly moved as little as 100Å in response to a single, manual voltage pulse to the stepper motor.

In automatic mode, the circuitry sent 10 ms pulses to the stepper motor every 100 ms. This mode was extremely useful for the final approach of the tip into tunneling range. To prevent shorting between the tip and the sample, the pulse train was terminated if a current in excess of a given setpoint value (typically 1 nA) was sensed. Exceeding the setpoint also caused the circuitry to fully retract the piezo tube by applying the full voltage (approximately 150 V) to the piezo. Tunneling was then re-established by allowing the piezo voltage to capacitively discharge, enabling a smooth approach of the tip toward the sample until feedback control was established.

Instrument Control Electronics

The system of electronics that governs the operation of a STM must employ five major components: (1) A current preamplifier; (2) feedback control electronics; (3) tip/sample bias supply; (4) X and Y scan drivers; and (5) image/information processing. Additionally, for electrochemical investigations, it is desirable to be able to alter the potential of the sample with respect to some electrochemical reference potential (e.g., the standard hydrogen electrode). The manner in which these elements interact to form an integrated system for the control of our microscope is represented in the diagram shown in Figure 2. In the construction of the control electronics for our STM, we have followed the lead of, and have been assisted by, several researchers from Prof. C.F. Quate's research group at

Stanford University.[19] Thorough discussions of the relevant theoretical and practical issues encountered in the design of control electronics for a STM are available in publications from his laboratory.[1,20] Consequently, we will discuss only briefly the electronic peculiarities of the system currently in use for the control of our microscope. Detailed schematics of all of the major electronic circuits can be found in the Appendix to this chapter.

Current Preamplifier. The current preamplifier provided current-to-voltage conversion and amplification and developed easily managed voltages (ca 10 mV to 10 V) from small electron tunneling currents (ca 10 pA to 10 nA). Current-to-voltage conversion was performed by differentially detecting the voltage that the tunneling current developed across a 10 MΩ resistor, producing a gain of 10^7 V/A. Because this method of current measurement did not require a well-defined ground reference level, the potential of the sample could be freely floated. In an effort to minimize the amount of electronic noise introduced into the system, a battery was generally employed as a bias supply. With the use of a commercial potentiostat, the sample and preamp could be floated together as a working electrode. These facilities are quite valuable for *in situ* electrochemical investigations.

A subsequent, adjustable gain element amplified the differentially detected signal by factors of either 10, 100, or 1000. In this manner the overall sensitivity of the preamp could be selected to yield conversion factors of 0.1, 1.0 or 10 nA/V. The available range in current sensitivity permitted a wide variety of STM experiments to be performed. The entire preamp was enclosed in a grounded metal box (1" X 1" X 2"), which could fit under the microscope's brass support piece.

Feedback Control Electronics. The principal elements of the electronics that maintain negative feedback control of the electron tunneling current are diagrammatically represented in Figure 2. The input stage of the circuit compares a user-specified current

setpoint to the amplified tunneling current signal derived from the preamp. The difference between the measured current and the desired setpoint is then adjustably amplified and/or integrated. The resultant signal is low-pass filtered and applied to a high-voltage gain stage. The response time of the feedback loop was varied through adjustment of the RC time constant of the low-pass filter. The high-voltage feedback signal was used to control the length of the piezo tube in order to control the tip/sample separation.

X-Y Scan Drivers. The high-voltage signals that drive the scanning motions of the piezo tube were derived from external sources. Depending on the specific experiment, either Wavetek function generators (Model 182A) or EG&G PAR Universal Programmers (Model 175) were used to generate the desired waveforms. The X an Y raster control signals were inputted to both the scan control circuitry and the video processor. The input to the scan circuitry was voltage-divided and applied to a variable gain amplifier. The amplified signal was then added to a DC offset, and the resulting sum was sent to a high-voltage amplifier to drive the lateral motions of the piezo tube. In this manner the area scanned by the tunneling tip was mapped into the XY signals delivered to the video processor.

Image Storage and Display. The video processor we used was an Arlunya Image Processor.[21] The processor accepted and digitized X,Y, and Z analog voltage inputs, and the X and Y inputs served to locate pixels in the 512 X 512 array, which represented the scanned sample area. The magnitude of the tube height or current signal was scaled into a 0-1 volt range and applied to the Z input of the video processor to set the brightness levels of the XY locations addressed by the scans. The video processor was also able to translate XYZ data into a standard video format, enabling images to be displayed on a video monitor and to be stored on video tape with a commercially available VCR. Images presented in this thesis are photographs of images that were displayed on the video monitor.

Discussion

As described above, the overall construction and choice of materials make this microscope modular and chemically inert. In particular, samples and tips can be readily and rigidly mounted in the microscope, while all metallic or potentially reactive surfaces are insulated from solution by either Teflon, chemically inert epoxy or neoprene. The materials used in the instrument also possess mechanical and thermal expansion properties that insure the stability of the instrument. Drift rates of less than 5Å/min while tunneling can be readily attained after an initial equilibration period of approximately 1 hour. Furthermore, the appreciable fluid capacity of the STM avoids solution compositional changes and greatly facilitates inclusion of auxiliary electrodes for electrochemical investigations. This combination of properties makes the instrument quite attractive for use in electrochemical applications.

The use of a stepper motor to move the scanner and tip made this STM somewhat top-heavy, and therefore led to increased susceptibility to vibrations. To counteract this, the brass support piece (which served to lower the center of mass of the microscope itself) and the brass vibration isolation plates were designed to work in concert to isolate effectively the STM from low frequency mechanical vibrations. Furthermore, when loaded with the microscope, the system of plates served to lower the center of gravity of the whole system, because the microscope's bottom was supported by the uppermost plate at a level equal in height to the lowest plate.[14] Additionally, the lossy silicone rubber feet proved to provide effective damping between adjacent plates. The entire system was found to provide sufficient stability so that atomic resolution images of graphite and MoS_2 could be obtained routinely (*vide infra*).

An advantageous feature of this microscope design is that the stepper motor driven approach mechanics and supporting electronics provide capabilities for fully remote

operation. This automatic approach facility, in conjunction with the modularity of microscope design, make this instrument ideal for use in inert atmosphere gloveboxes where manual dexterity is compromised. Because tip speeds in the automatic approach mode range from 0.1 μm/sec to 5 μm/sec (depending on spring tension and voltage pulse height), macroscopically large distances (ca 100 μm) can be traversed in less than 1 minute. Thus, the conditions on coarse tip-sample positioning are less stringent than with manual controls, where the tunneling tip must be visually placed within a few microns of the sample for the rapid final approach into tunneling range. This arrangement also minimized inadvertent "crashing" of the tip (direct physical contact between the tip and the sample) during coarse positioning. In fact, it was found that the ability to detect tunneling current, deactivate the pulse train, and retract and relax the piezo tube were so effective at preventing tip/sample shorting that most W and Pt/Ir tips yielded atomic resolution images without further procedures. Moreover, these capabilities facilitated a "field-emission" procedure that was a necessary step in preparing insulated STM tips for *in situ* investigations. The usefulness of this particular feature of the microscope will be explained in more detail in Chapter 4.

The electronic components of the microscope work in unison to form a versatile set of control circuitry. Thus, the operating conditions of the STM can be readily adjusted for optimal imaging of a particular surface. Smooth surfaces, such as the Van der Waals planes of MoS_2 or HOPG, were typically imaged with constant-tip-height,[7,22] or "fast-scan" methods. In this mode of operation the feedback response of the microscope is damped so that an average tip/sample separation, rather than a constant tunneling current, is maintained. Topographical information is then obtained by recording the difference between the measured tunneling current and the setpoint current value. X and Y scan frequencies may be as high as 2 kHz and 50 Hz, respectively. Thus, 50 complete images may be obtained per second, perhaps allowing dynamic surface properties to be observed. Figure 3 shows atomic resolution images of HOPG and MoS_2 that were obtained with our microscope

operating in fast-scan mode. The bright features in the images shown in the Figure correspond to atomic positions of high tunneling current, and the images are in good agreement with images obtained by other researchers using similar methods.[1,7,23] For the case of HOPG (Fig. 3a), the experimentally obtained image is in agreement with recent theoretical work[24] that suggests that only the B sites on the surface (i.e., those atoms without neighbors in adjacent layers) should appear in the STM image if the sample crystal states are not significantly perturbed by the presence of the tip. The positions of these B site surface atoms are separated by 2.46Å.[1]

The layered structure of MoS_2 is composed of S-Mo-S sandwiches with the Mo atoms possessing trigonal prismatic coordination. An unambiguous identification of the features appearing in the STM image of Fig. 3b is difficult because the Mo and S sublattices can be superimposed with a lattice translation. Recent theoretical calculations[25] indicate that the matrix element for electron transfer from the sample to the tip is maximized over the Mo nonbonding d_z^2 orbitals for tip/sample separations between 7 and 10 Å. Consequently, in the absence of overriding local density of states effects, the tunneling current should also reach a maximum value over the subsurface Mo atoms in fast-scan STM experiments. Experimental support for this theoretical prediction is found in recent STM investigations of a similar material, WTe_2.[26] The metal atom in this layered material possesses a distorted octahedral coordination and, consequently, Te and W sublattices cannot be superimposed with a lattice translation. In these observations the positions of the subsurface tungsten atoms were clearly resolved. Though the electronic structures of MoS_2 and $WeTe_2$ are not identical (the metal d_z^2 orbitals are expected to mix with the $d_{x^2-y^2}$ and d_{xy} orbitals in the latter material), and the tip/sample separation is not well known in our experiment, we tentatively assign the high tunneling current features in Fig. 3b to correspond to the positions of the subsurface Mo atoms. The Mo-Mo distance in this material is known to be 3.16Å.[27]

Fast-scan techniques cannot be employed for rough surfaces since the relatively slow feedback response prohibits the tip from following large height variations. Such surfaces may be imaged by allowing the feedback to respond quickly while the tip is rastered. In this so-called "slow-scan" mode a constant tunneling current is maintained. If the variations in the height of the sample are appreciable, then atomic-scale information is lost when the Z signal is mapped into the 0-1 volt input range of the Arlunya video processor. Information concerning the smaller-scale features of the surface can be recovered if the derivative of the Z signal with respect to position is displayed. The derivative signal is obtained by using a high-pass filter such that maxima in the resultant signal correspond to regions of rapidly changing height. Figure 4 demonstrates the complementary nature of images obtained with slow-scan and derivative mode techniques. X and Y scan frequencies were 5 Hz and 6 mHz, respectively, for both images. Figure 4a is a slow-scan image of a relatively large area (1250 X 1000 Å) of a polished and annealed Pt(111) single crystal.[28] The overall variation in height across the scanned area is ≈ 1000 Å, with the brightest regions being the highest portions of the sample. Figure 4b is an image of the same region obtained using the derivative of the Z signal. The surface had drifted ≈150 Å downwards with respect to the scan window during the time between acquisition of the two images. Steps and ledges are highlighted in this second image since abrupt changes in the height of the surface appear bright in this image. By considering the two representations simultaneously, a more detailed view of the surface may be obtained. Evidently, the annealing treatment did not produce a surface with large area terraces. We learned subsequently that the sample had been significantly damaged when it was originally cut from the single crystal boule.

A final noteworthy feature of the microscope is the ability to achieve accurately large variations in the distance between the tip and sample. To achieve such control, single voltage pulses are employed to adjust the Z-piezo voltage at which tunneling occurs. Complete retraction of the piezo then yields the desired tip/sample spacing. This technique

can be used to control accurately tip/sample distances for values as large as the full travel of the piezo tube (0.75 μm). Calibration of the piezo travel in response to a pulse (for a given pulse height and set of springs) allows coarser distance variation over the travel of the stepper motor. This procedure has applications in potentiometric, galvanostatic or cyclic voltammetry experiments where the STM tip is used as a microelectrode at well-defined small tip/sample spacings. Our laboratory is currently exploiting these instrumental capabilities in several electroanalytical applications, and will describe the results of these experiments in subsequent publications.

CONCLUSION

We have constructed a scanning tunneling microscope that is well suited for electrochemical investigations. This STM incorporates several novel features that have not been employed elsewhere, including remote operation, compatibility with electrochemical solvents, variable distance control, facile tip/sample interchange, modular design, and adaptability to most electroanalytical applications. With the microscope operating in air, we have been able to obtain atomic resolution images of HOPG and MoS_2. The microscope has also proven to be useful for imaging atomically rough surfaces with high resolution. The results presented in Chapter 4 demonstrate that the instrument is quite valuable for investigations of the solid/liquid interface.

References

1. Bryant, A. Ph.D. Thesis, Stanford University, 1986.

2. Binnig, G.; Rohrer, H.; Gerber, Ch.; Weibel, E. *App. Phys. Lett.*, **1982**, 40, 178.

3. Binnig, G.; Rohrer, H.; Gerber, Ch.; Weibel, E. *Phys. Rev. Lett.*, **1982**, 49, 57.

4. Binnig, G.; Rohrer, H. *Sci. Am.*, **1985**, August, 26.

5. Binnig, G.; Gerber, Ch.; Marti, O. *IBM Tech. Disc. Bull.*, **1984**, 27, 3137.

6. Gerber, Ch.; Binnig, G.; Fuchs, H.; Marti, O.; Rohrer, H. *Rev. Sci. Instr.*, **1986**, 57, 221.

7. Bryant, A.; Smith, D.P.E., Quate, C.F. *Appl. Phys. Lett.*, **1986**, 48, 832.

8. Binnig, G.; Smith, D.P.E. *Rev. Sci. Instr.*, **1986**, 57, 1688.

9. Sonnenfeld, R.; Hansma, P.K. *Science*, **1986**, 232, 211.

10. Sonnenfeld, R.; Shneir, J.; Drake, B.; Hansma, P.K.; Aspnes, D.E. *Appl. Phys. Lett.*, **1987**, 50(24), 1742.

11. Morita, S.; Otsuka, I.; Ohasa, T.; Yokoyama, H.; Iwasaki, T.; Mikoshiba, N. *Jap. J. Appl. Phys.*, **1987**, 26(11), L1853.

12. Itaya, K.; Sugawara, S. *Chem. Lett.*, **1987**, 1927.

13. Lev, O.; Fan. F.F.; Bard, A.J. *J. Electrochem. Soc.*, **1988**, 135, 783.

14. Dovek, M.M.; Heben, M.J.; Lang, C.A.; Lewis, N.S.; Quate, C.F. *Rev. Sci. Instr.*, **1988**, 59(11), 2333.

15. Murgatroyd, J.B.; Sykes, R.F.R. *J. Soc. Glass Tech.*, **1944**, 28, 406.

16. Stavely Corp., E.B.L. Div., East Hartford, CT.

17. Personal communication, J. Jahanmir, Quanscan, Inc., Pasadena, CA.

18. CMX Distance Measuring Interferometer, Model 2010, CMX Systems, Inc., Meriden, Conn.

19. In particular, M.M. Dovek and C.A. Lang.

20. Park, S. Ph.D. Thesis, Stanford University, 1986.

21. Arlunya Model TF5111, Princeton Electronic Products, Inc., No. Brunswick, NJ.

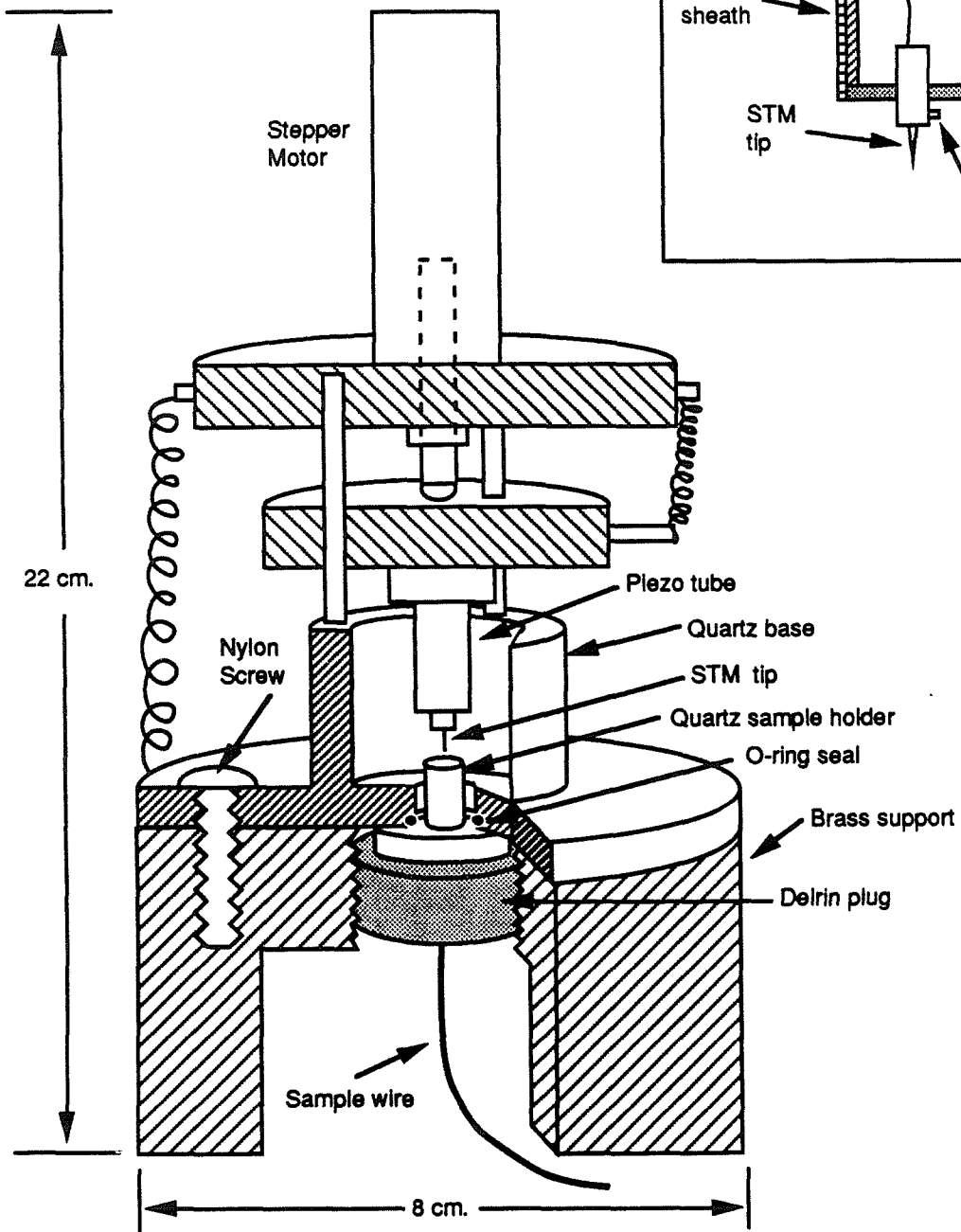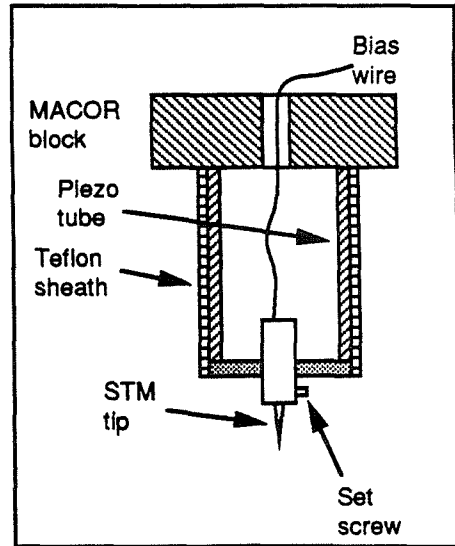22. Hansma, P.K.; Tersoff, J. *J. Appl. Phys.*, **1987**, 61(2), R1.

23. Kramar, J.A. Ph.D. Thesis, California Institute of Technology, 1990.

24. (a) Tomanek, D.; Louie, S.G.; Mamin, H.J.; Abraham, D.W.; Thomson, R.E.: Ganz, E.; Clarke, J. *Phys. Rev. B.*, **1987**, 35, 7790. (b) Batra, I.P.; Garcia, N.; Rohrer, H.; Salemink, H.; Stoll, E.; Ciraci, S. *Surf. Sci.*, **1987**, 181, 126. (c) Williams, R.S.; Farrelly, D.; Eklund, E.A.; Snyder, E.J. Submitted to *Nature*.

25. Personal communication, T.R. Coley, California Institute of Technology, Pasadena, CA.

26. Tang, S.L.; Kasowski, R.V.; Parkinson, B.A. submitted to *Nature*.

27. Dickinson, R.G.; Pauling, L. *J. Am. Chem. Soc.* **1923**, 45, 1466-71.

28. Samples were first mechanically polished successively with 6 μ and 1 μ diamond grits. An electromechanical polishing technique (see Ref. 29), employing alternating currents and a 5 $\underline{M}$ NaCN bath, was used to remove surface damage. Further processing (personal communication, H.D. Abruna) involved electropolishing with a 10 $\mu A/cm^2$ current in 80 °C conc. HCl (4 hrs.), and exposure to hot conc. HNO_3 (80 °C, 1 hr.). Annealing was then performed by heating the crystal to 700 °C in a flowing Ar stream, introducing I_2 vapor into the stream for 10 min., and allowing the temperature to decrease to 200 °C. The sample was then reheated to 450 °C in a pure Ar flow.

29. Samuels, L.E. *Metallographic Polishing by Mechanical Methods*; American Society for Metals: Metals Park, OH., 1982.
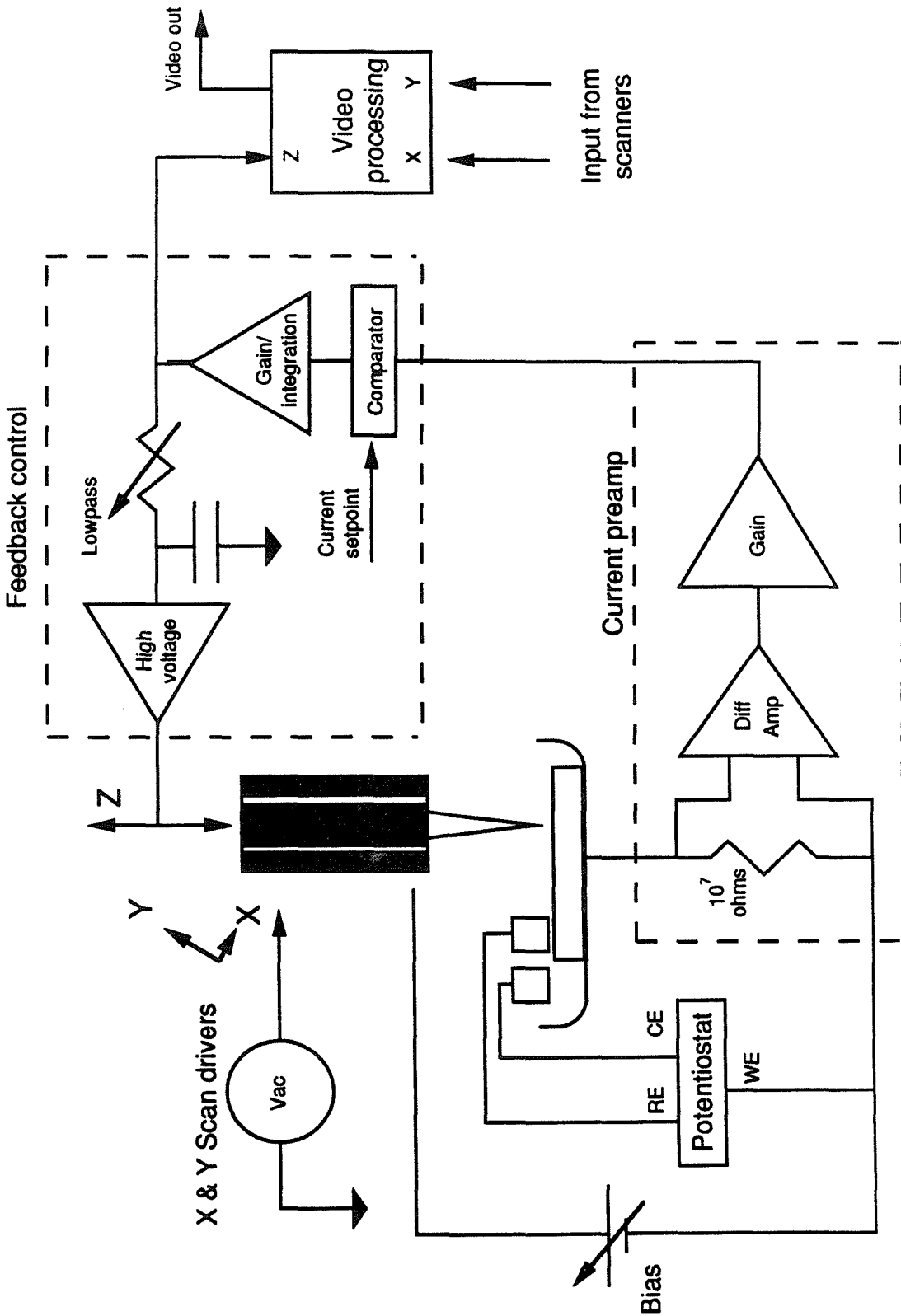
Figure 1:

Diagram of the scanning tunneling microscope constructed for electrochemical investigations. The microscope body is composed of a Quartz base and of stepper motor driven approach mechanics. The quartz base supports the approach mechanics, provides for sample mounting, and confines a small volume of solution in the region of the tip/sample gap. The approach mechanics support the piezoelectric scanner and the tip, and facilitate coarse formation of the tunnel junction. The body of the microscope is anchored to a brass support piece that serves to lower the center of gravity of the instrument.

Piezo construction

MACOR block

Bias wire

Piezo tube

Teflon sheath

STM tip

Set screw

Stepper Motor

22 cm.

Nylon Screw

Piezo tube

Quartz base

STM tip

Quartz sample holder

O-ring seal

Brass support

Delrin plug

Sample wire

8 cm.

Figure 2:

Block diagram of the electronic components of the scanning tunneling microscope

described in the text. Five necessary control elements are illustrated: (1) the current

preamplifier; (2) feedback control electronics; (3) tip/sample bias supply; (4) X and Y scan

drivers; and (5) image processing facilities. Potentiostatic sample control may be employed

for electrochemical investigations. Detailed schematics of the circuitry can be found in the

Appendix to the chapter.

61

Figure 3:

Images of (a) highly ordered pyrolytic graphite and (b) MoS_2, obtained in air. Both images were obtained with the microscope operating in fast-scan mode. The measured current was high-pass filtered to remove scan coupling. (a): Tungsten tip, + 200 mV bias (tip positive), I_t = 1 nA. (b): Tungsten tip, + 300 mV (tip positive), I_t = 0.5 nA. The nonorthogonality of the scan directions is particularly evident in the image of MoS_2. HOPG samples were kindly provided by Dr. A. Moore. Natural MoS_2 samples were obtained from Climax Molybdenum Co., Greenwich, CT.

(a) ~5 Å


(b) ~10 Å
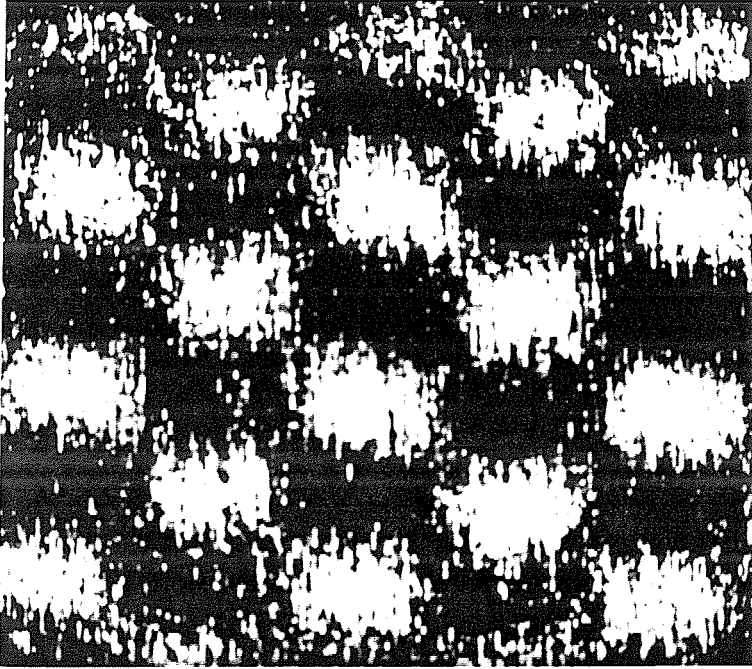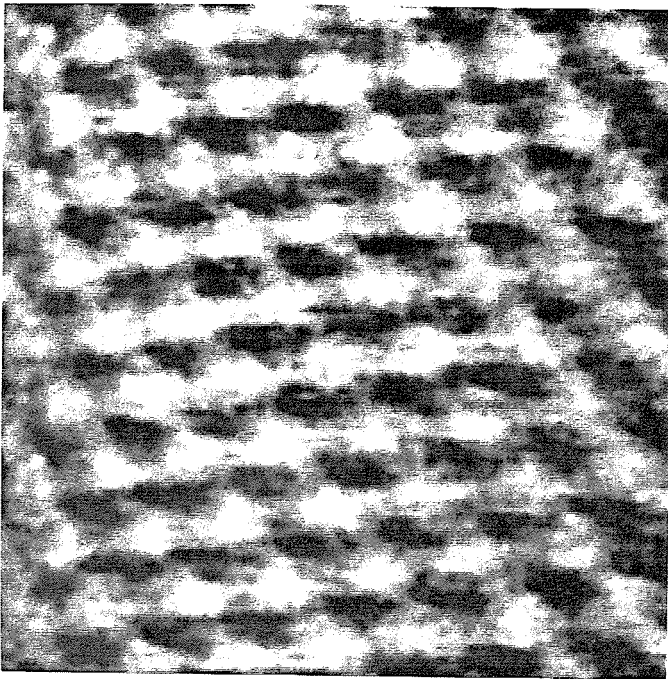
Figure 4:

Slow-scan image of a polished and annealed Pt(111) crystal (see text): (a) Z height data,

and (b) differential of Z signal with respect to position. Both images were obtained with

tungsten tips held at a positive bias of 48 mV. The tunneling current was 0.3 nA for (a) and

0.5 nA for (b). The height variation in the image is $\approx$1000 Å. The high-pass filtered signal for

the differential image in (b) was obtained by subtracting a low-pass filtered version of the

signal (1 kHz, 48 db/octave) from the unfiltered signal.

(a)

~1000 Å

~1200 Å

(b)

~1000 Å
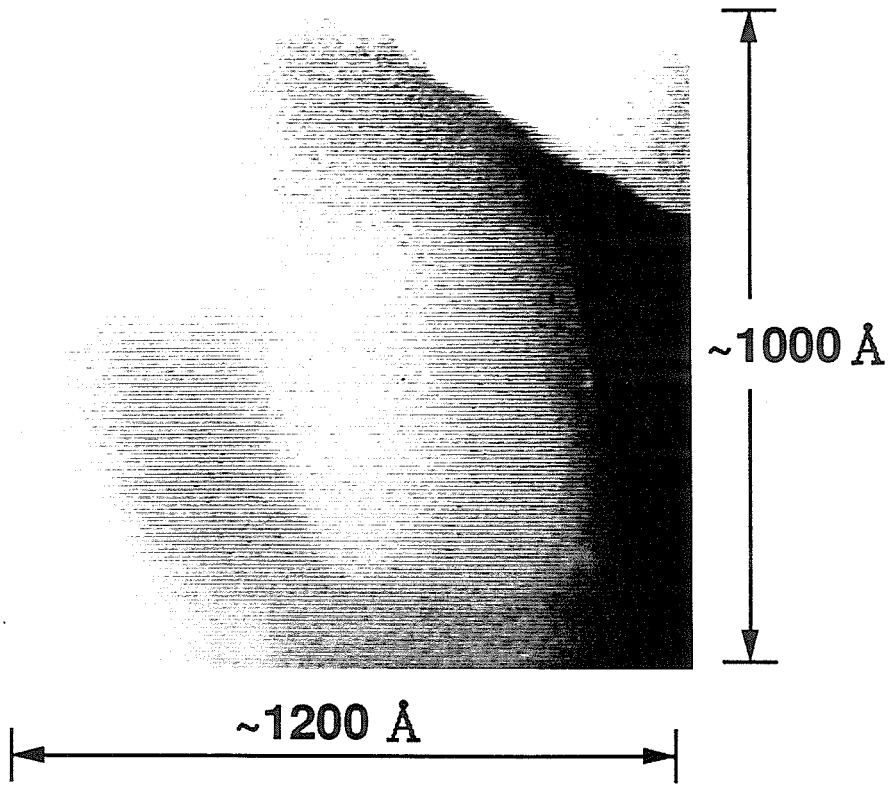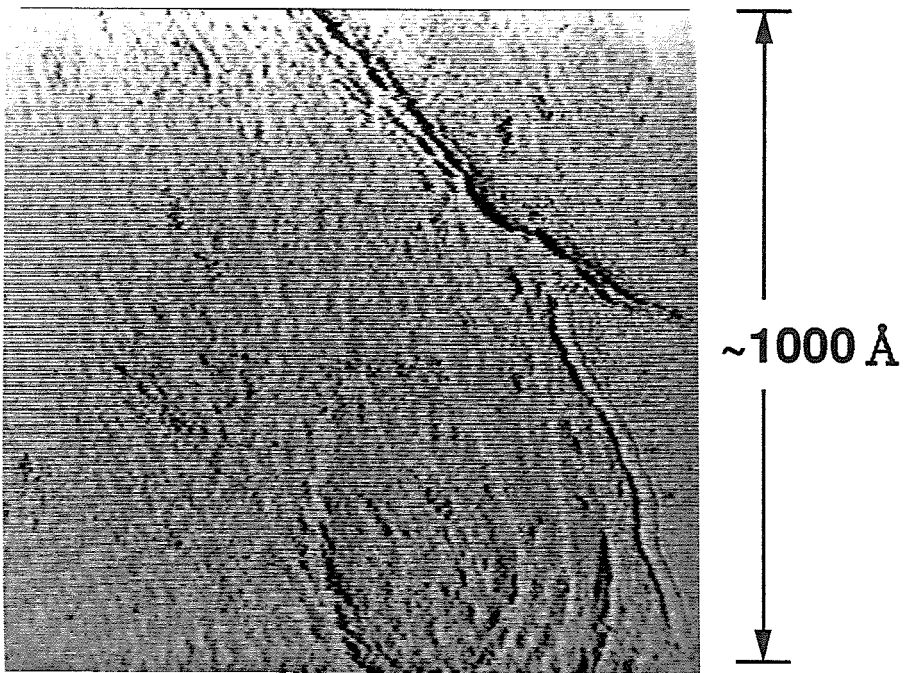
Appendix: Circuit Diagrams

Detailed circuit diagrams for the important electronic components of the STM are presented in this Appendix. The four schematic diagrams presented depict the circuitry for (1) the feedback control electronics; (2) the high voltage electronics that control the tip/sample spacing; (3) the scanning circuitry that controls the lateral motions of the tip; and (4) the digital circuitry that develops pulses to drive the stepper motor and that enable the automatic approach/retraction facility. Captions to the figures describe the features of each circuit in more detail.

Figure A1:

Diagram of the circuit used to develop a feedback control signal. The circuit compares a user-specified current setpoint value to the measured tunneling current, and develops an error signal. The error signal is adjustably amplified and/or integrated. Negative and positive feedback output signals are generated. An input for overriding the feedback control is also provided. All op-amps are AD544s or equivalent.
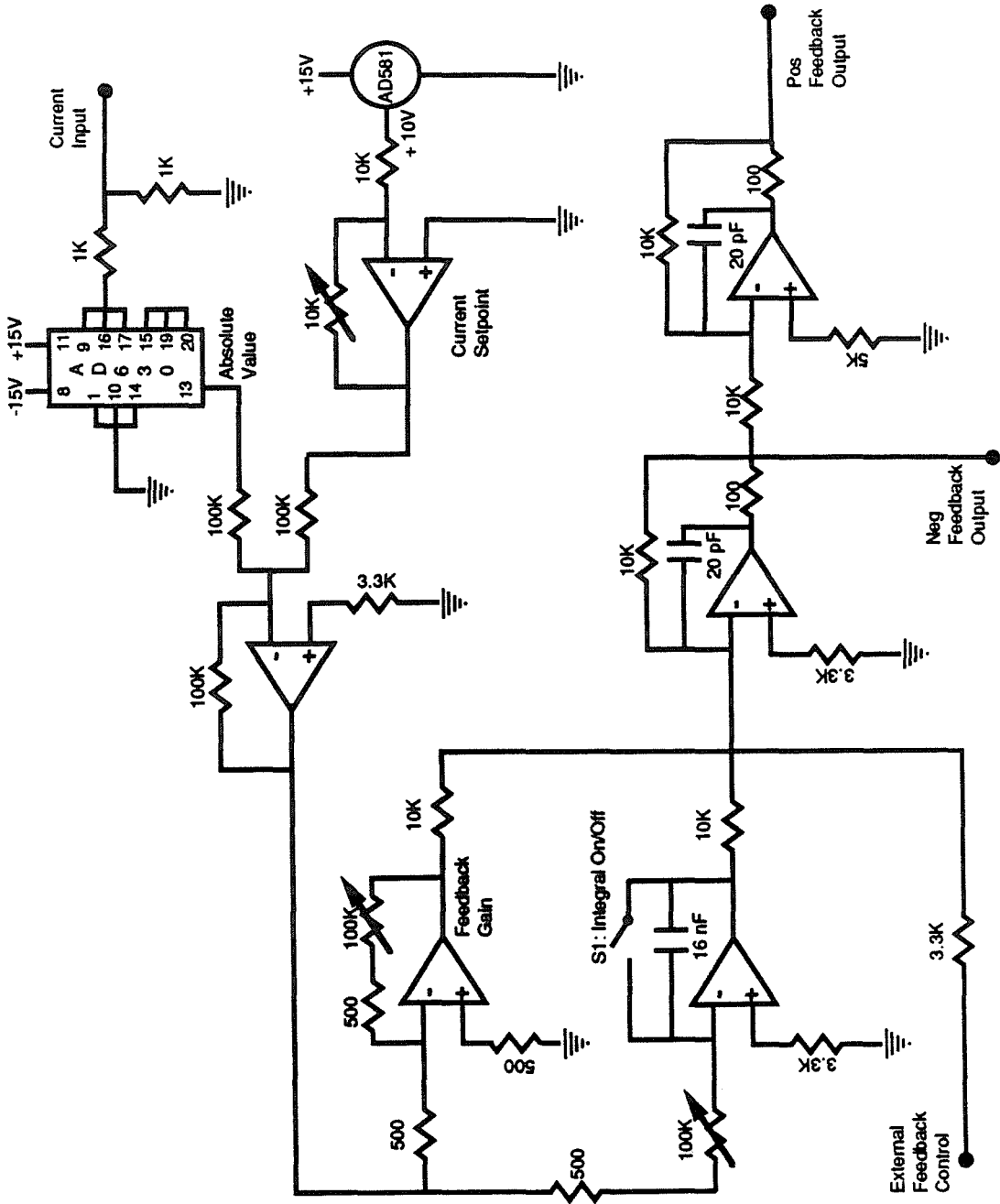
Figure A2:

Diagram of the circuit used to develop high-voltage signals for controlling the tip/sample

separation. The negative feedback output from the circuit presented in Fig. A1 is applied to

the feedback input of this circuit. An adjustable low-pass filter is used to control the rate at

which the input to the high-voltage op-amp can vary. This control signal is amplified by a

factor of 20 before it is applied to the inner electrode of the piezo tube. When the piezo-

retract input senses an output from the stepper motor control circuit (Fig. A4), the

cascaded TIP31 transistors turn on, and the piezo tube is rapidly retracted. The piezo tube

then relaxes into tunneling range as the charge on the 250 μF capacitor leaks through the

1 MΩ resistor to ground. Ports for monitoring a fraction of the Z-piezo voltage, and for

applying a modulation to the tip/sample gap, are also provided. A diode network (not

shown - see Fig. A3) protects the op-amp from damaging transients.

Z Piezo Voltage Output

+150V

−15V

BB5383

120K

6K

1M

6K

AD544

AD544

250 μF

10 μF

50K

TIP31A

+15V

TIP31A

+15V

1M

Z piezo Modulation Input

Z piezo Voltage Monitor

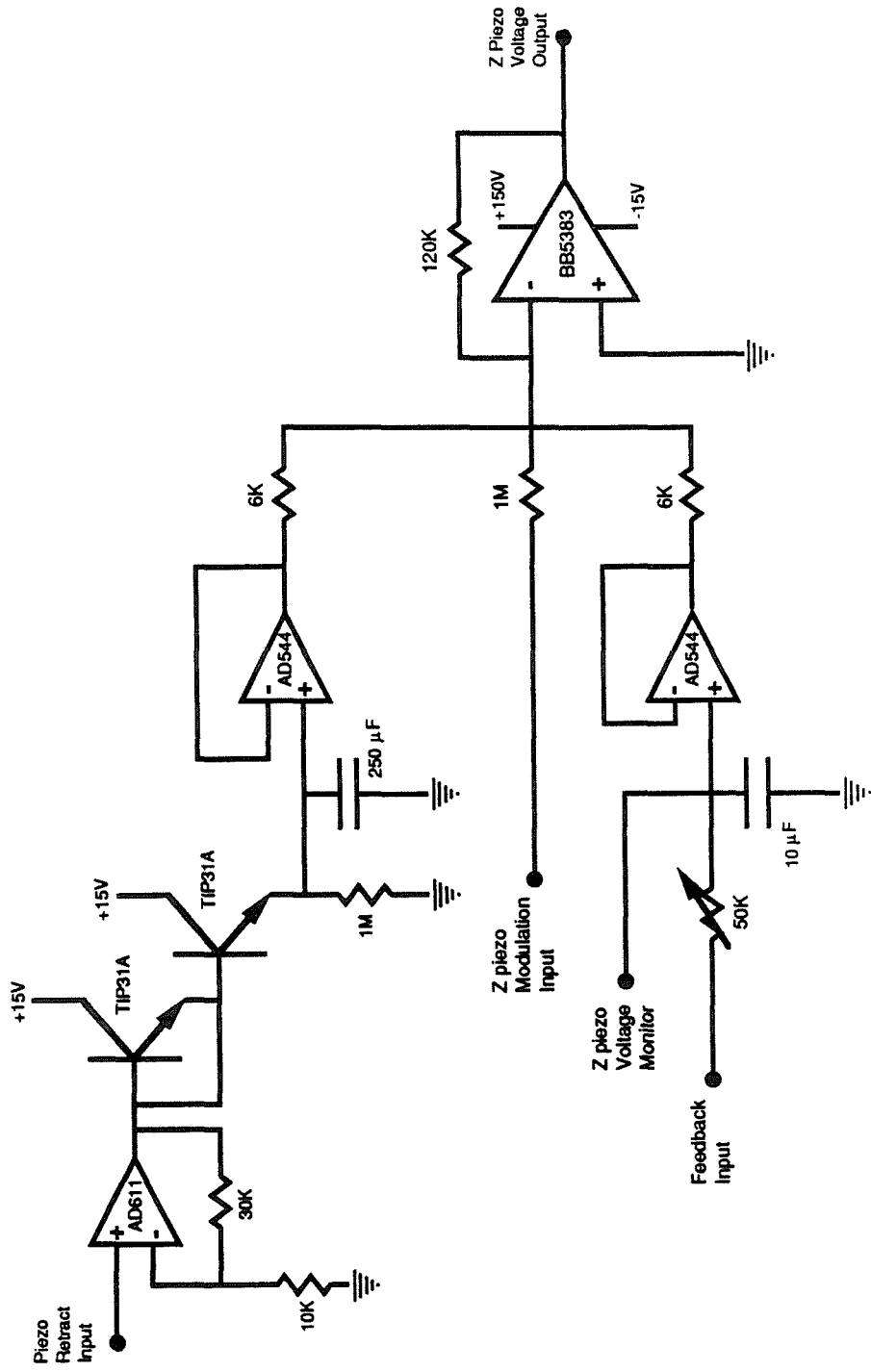Feedback Input

AD611

30K

10K

Piezo Retract Input

Figure A3:

Diagram of the circuitry that controls the scanning motions of the tip. Identical circuits are used for driving the motions of the piezo tube in both X and Y directions. The outputs of the two scan circuits are applied to two adjacent electrodes of the four outer electrodes on the piezo tube. The remaining two electrodes are grounded. When the circuit is activated, inputted sinusoidal or sawtooth waveforms are first voltage-divided, and then adjustably amplified. The resultant signal is applied to the input of the high-voltage amplifier. A switch allows an additional factor of 10 in amplification to be selected. A user-selectable DC offset value is summed with the time-varying signal at the input to the op-amp. A diode network protects the high-voltage op-amp from damaging transients.

To piezo

1N4937

1N4937

1N4746A

ECG 5101A

BB5383

+ 150V

− 15V

100K

10K

2 X1N4148

10K

S1

100K (lo)

10k (hi)

− 15V

60

1K

270

+ 5V

1 μF

+ 15V

− 15V

100K

AD544

750

S1

512

Scan & Video
Drive
(4V pp)

To video

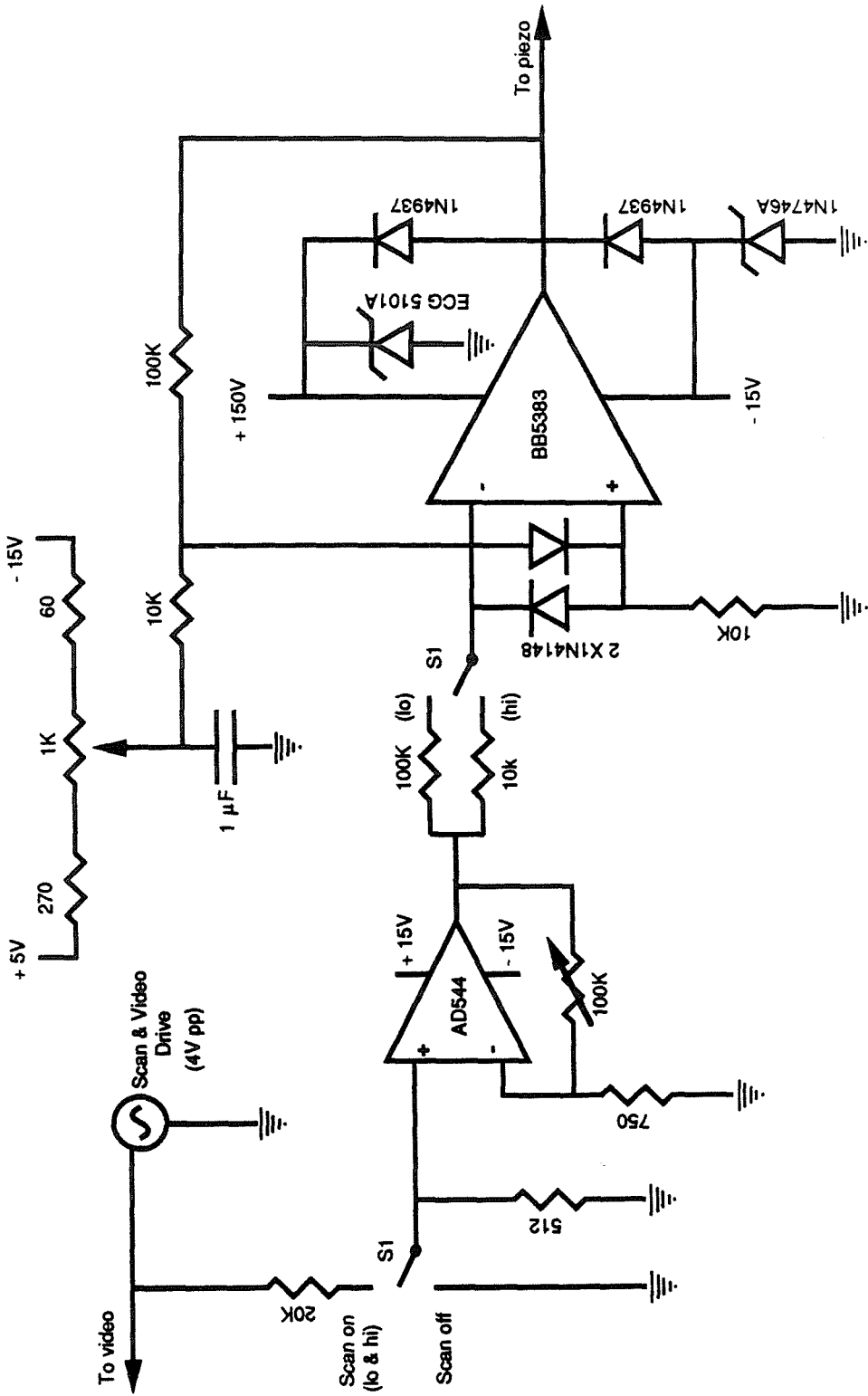20K

Scan on
(lo & hi)

Scan off

Figure A4:

Diagram of the circuitry that develops pulses that drive the stepper motor and enables the automatic approach facility. If the measured current is less than 0.16 nA (assuming that the sensitivity of the current preamp is 1 nA/V), and the circuitry has been reset, then 10 ms pulses, of variable voltage height, are sent to the stepper motor at 100 ms intervals. When a current exceeding the 0.16 nA threshold is sensed, the pulse train is terminated, and the piezo retract output voltage goes to TTL high (see Fig. A2). Green and Red LEDs are on when pulses are being sent to the stepper motor, and when the threshold value has been exceeded, respectively.
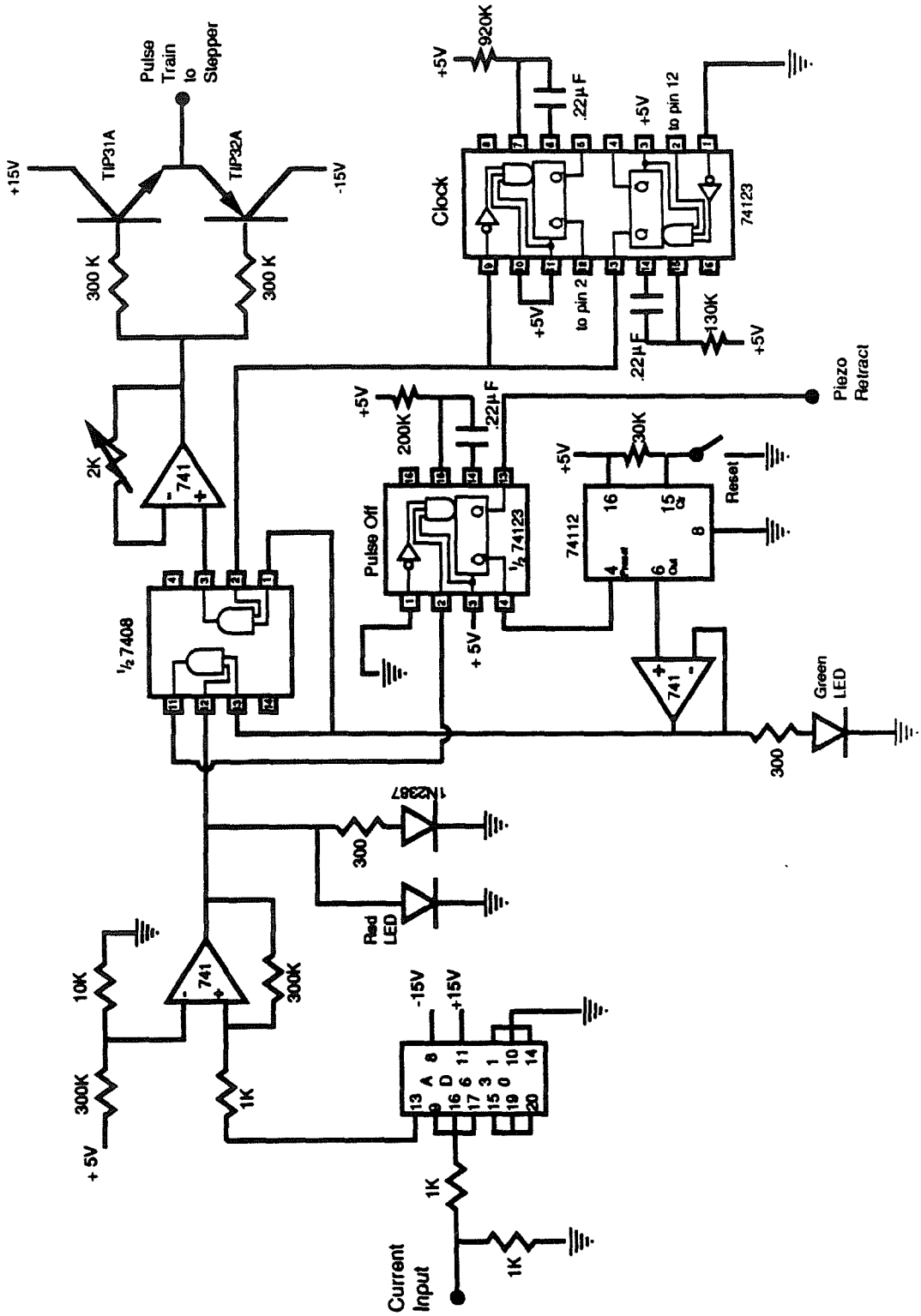
Chapter 4

Atomic Resolution Imaging
of Electrode Surfaces in
Solutions Containing Redox Active Ions

Introduction

As discussed in earlier chapters of this thesis, the electrochemical environment poses new challenges to the tunneling microscopist. The total current between tip and sample may contain a substantial component attributable to faradaic charge transfer reactions. This current interferes with conventional STM imaging because it obscures the tunneling current and hinders feedback control of the tunneling gap. Previous investigators have had to choose the electrode/electrolyte system carefully to insure that electrochemically active redox reagents were not present, and/or have had to constrain their ability to image by working at electrode and tip potentials where faradaic tip/sample currents were minimal (for examples, see Chapter 2). Since many electrode/electrolyte combinations of interest typically contain high concentrations of redox active reagents, these constraints will not provide a general method for successful imaging using conventional STM techniques. In this chapter, we describe the preparation of coated STM tips that relax this restriction. Such tips can have less than 100 Å^2 of exposed metal area at the apex, and apparently completely discriminate between the faradaic charge transfer currents and the tunneling current. To our knowledge, these tips exhibit the smallest amount of exposed metal area of any tips employed in STM studies to date. Below, we describe our procedures for tip etching and tip coating, and then describe the imaging capabilities that these tunneling tips have demonstrated.

Materials

We have employed both tungsten (Alfa) and a platinum-iridium (Pt-Ir; 70% Pt, 30% Ir from Engelhard) alloy as tunneling tip materials in our investigations. Both materials possess sufficient mechanical stiffness in 0.020" drawn wire form to be useful in STM

experiments, and both may be reproducibly etched by electrochemical means to form sharp

tunneling probes. The mechanical rigidity of these materials also insures that the as-etched

tips remain sharp during the coating processes we have developed. Insulated W tips have

been prepared with the use of poly(α-methylstyrene) layers. Pt-Ir tips may be coated with

either PαMS or glass, since this material exhibits a high melting temperature and oxidation

resistance. The imaging application dictates the choice of tip and coating materials. For

example, PαMS/W tips are easily fabricated and are well suited for imaging surfaces in

contact with aqueous or alcoholic solutions. However, these tips are not useful for imaging

in ambients that cause swelling or dissolution of the polymer coating (e.g., CH_3CN, CH_2Cl_2).

Though more difficult to form, Pt-Ir glass-coated tips may be employed in these cases. The

exposed Pt-Ir metal is also expected to be more resistant to oxidation and corrosion, and

electrochemical reactions occurring at these surfaces should be more facile. This latter

feature of the Pt-Ir/glass tips has been exploited in the construction of small

ultramicroelectrodes (see Chapter 5), and such tips will find use in potentiostatic,

galvanostatic or cyclic voltammetry experiments where the insulated tip is used as an

electrode at well-defined tip/sample spacings in an STM configuration.

The coating of these metal tips by glass and polymer layers (*vide infra*) was found to

be a function of the sharpness, surface roughness, and cone angle of the etched tips.

Consequently, as a crucial starting point to tip preparation, the etching characteristics of

0.020" wires were investigated.

Tip Etching

The electrochemical etching bath was different for each of the two tip materials. For

the Pt-Ir alloy an unstirred solution of 6 $\underline{M}$ NaCN and 2 $\underline{M}$ KOH was employed. Similar baths

have been used elsewhere for Pt-Ir etching.[1] The cyanide salt was employed to provide

complexation of Pt and Ir ions in order to hasten electrochemical dissolution of the tip. The

presence of OH⁻ served to inhibit the formation of HCN. Tungsten tips were etched in an unstirred 4 $\underline{M}$ KOH solution. All etching was performed in a fume hood.

To control the depth of immersion, the tips were mounted in a chuck, which had an adjustable distance travel. A 3" inner diameter wax-impregnated graphite ring was used as the counter electrode, and this ring was centered around the Pt-Ir tip. Using this arrangement, the tip and counter electrode were lowered simultaneously into the etching bath. During etching, an AC potential was applied between the tip and counter electrode, and the current was monitored as a function of time in the etching solution.

Figure 1a shows a representative I vs. t curve for a Pt-Ir tip etched at 25 RMS volts (60 Hz). Two distinct regions may be discerned in the figure. The transition from region I to region II was abrupt if the initial current, which was related to the initial depth of immersion, was at least 1.5 to 2.0 amps. Orange-red light was emitted from the apex of the tip during the etching process.

In stage I, visual inspection of the tip indicated that the diameter of the immersed portion of the tip was uniformly reduced with etching time, while the length remained essentially unchanged. The transition to stage II corresponded to a dramatic change in the etching mechanism of the tip. During this second stage a long and narrow metal filament, a result of stage I etching, was reduced in length without further reduction in diameter. The shapes of tips emersed at points labeled "A" or "B" in Figure 1a are schematically represented in the corresponding portions of Figure 1b. A Pt-Ir tip, removed 5 seconds after the abrupt transition from stage I to stage II etching, symbolized in the portion of figure 1b labelled "stop," was repeatedly found to be morphologically smooth and sharp, with an aspect ratio of approximately 2 (height/radius). An electron micrograph of such a tip is shown in Figure 2a. These tips were well suited for subsequent coating by either polymer or glass.

The current vs. time curves for W tips also displayed these two distinct stages of

etching behavior. In this case the etching voltage was typically 30 VRMS, and the transition to stage two occurred within ≈50 s of the initiation of the etching. These tips were considerably sharper than the Pt-Ir versions, as shown in Figure 2b.

Over a variety of runs, we observed that etched tips varied widely in geometry and morphology as a result of changes in etching voltage, etching time or the age of the etching solution. Fortunately, the current vs. time relationships of the tips provided a standard means by which the etching process could be monitored. Such curves reliably described the evolution of the tip structure for most experiments, and the above etching procedure was found to be quite satisfactory for producing the desired tip features.

Tip Coating

In order to limit the amount of electrochemically active area (and thereby suppress faradaic currents in STM imaging mode), the etched Pt-Ir tips were coated with either a glass or a polymer layer. Tungsten tips were damaged by the high temperature processing necessary for glass coating and, consequently, were coated only with PαMS. The two similar coating methodologies are described below.

Glass Coating. A coating apparatus was constructed in order to apply controllable, uniform coatings of nonporous glass insulation to the etched Pt-Ir tips. The apparatus is depicted in Figure 3, and consisted of a tip positioner that facilitated variable speed translation and a filament that produced molten glass beads to coat the tip.

The glass was maintained at the desired temperature by a resistively heated 0.020" Pt filament. In order to localize molten glass beads by surface tension, part of the filament was bent into a teardrop shape that measured approximately 1.5 mm in inner diameter. To provide for measurement of the filament's temperature, 0.005" Pt and Pt-Rh(10%) thermocouple wires were welded to the Pt filament. A temperature-control circuit was

employed to maintain constant preset filament temperatures during the various steps in the coating procedure. Support for the filament consisted of two brass posts that were fed through a plexiglass base. The brass posts were cooled by water that flowed through the posts, and through a rubber tubing bridge that connected them, while the filament was heated. The posts also provided electrical contact to the filament. Prior to melting the glass, the entire filament-post system was covered with a bell jar and was evacuated through a port in the plexiglass base. A liquid N_2 trap was essential for preventing pump vapors from reacting with the molten glass.

A soda-lime glass (Corning Glass # 0080) was chosen for tip coating because its thermal expansion coefficient (α), 9.5×10^{-6} $^\circ C^{-1}$ (Ref. 2) closely matched that of Pt-Ir(30%) (estimated to be ~8.3×10^{-6} by assuming that α varies linearly from α_{Ir} to α_{Pt} with Ir content[3]). Additionally, the working point of the soda-lime glass (990 $^\circ C$) was readily accessible with a Pt filament.[2] Prior to use, the glass was cleaned with i-C_3H_7OH and deionized water.

To prepare the glass for coating the metal tip, glass from a 2 mm diameter rod was fed into the teardrop of the electrically heated filament (ca 1400 $^\circ C$). The filament was then cooled to room temperature and the system was enclosed with the bell jar and evacuated. When the interior pressure reached 40 mtorr, the filament was electrically heated to 1450 ± 20 $^\circ C$ for 5 minutes. During this time period, trapped gases were evolved from the molten glass bead. While maintaining a constant filament temperature, the bell jar was then vented to atmospheric pressure. This step served to insure that unescaped gas bubbles collapsed to a size that did not introduce pinholes in the STM tip's coating. The temperature of the glass was then reduced to a value used for the actual coating process, typically 1350 ± 20 $^\circ C$.

The freshly etched tip was then mounted in a collet (Fig. 3), and positioners were used to center the tip relative to the molten glass bead. A Newport micrometer driver (model

855C) was then employed to advance the tip into the glass (Fig 3). Tip speeds between 0.2 and 20 mm/min were maintained as the tip was introduced into, and translated through, the teardrop of molten glass. During this process, glass was transferred from the teardrop to the tip. The electric heating current was adjusted by the temperature-control circuit to maintain a constant filament temperature despite the changing thermal mass of the filament. The progress of the coating was monitored by observing the filament from above during the coating process. In all cases, virtually all the glass was removed from the filament with 5 to 7 mm of tip translation. Further translation exposed a portion of the bare shaft, which was subsequently gripped with tweezers in order to remove the tip from the collet.

At tip speeds greater than ≈10 mm/min, the tip was not coated, but rather the glass bead was pushed out of the teardrop by the advancing tip. Speeds less than ≈5 mm/min allowed the tip to punch through the molten glass bead, and resulted in relatively large amounts of exposed metal area at the apex. Although these tips were not optimal for STM work, we have used tips made with these slow translation speeds to produce ultramicroelectrodes with sizes in the range of 0.001 to 25 μm^2 (see Ref. 4, and Chapter 5). Intermediate tip speeds were the most desirable for STM tip fabrication. However, because the glass viscosity was a strong function of temperature, the useful speed ranges were also quite sensitive to variations in the glass-melt temperature. The correct tip speed was achieved when the shape of the apex of the tip could be seen emerging from the glass bead. It is important to note that at present, this tip-coating process can be only qualitatively controlled. Because the Pt filaments are fashioned by hand, the shape of the filament is an important variable that remains difficult to control. Unfortunately, the lifetime of a filament is limited (ca 10-20 coatings) since with increasing amounts of time at elevated temperatures, the filament softens and begins to sag. A tip possessing a small amount of exposed metal area is best produced by coating and characterizing a series of tips with similar shapes and morphologies while using the same filament. The amount of exposed metal area of each tip

in the series, as determined by electrochemical techniques (*vide infra*), can then be used to suggest modifications to the melt temperature and tip-translation velocity for the next tip in the series. With this iterative process a tip with the desired characteristics may be obtained. By following this strategy approximately 1 in 5 tips are suitable for STM imaging under solution in the most demanding electrochemical conditions (*vide infra*).

Polymer Coating. Two different procedures were used for forming polymer-coated tips. Poly(α-methylstyrene) (PαMS) (Aldrich Chemical Co., Milwaukee, Wisconsin, U.S.A.), with a molecular weight of ≈60,000, was found to have mechanical properties well suited for coating by either method. The first procedure was qualitatively similar to that used for glass coating and also required a heated wire filament. However, because of the relatively low melting temperature of the PαMS, 0.020" copper or nichrome wire could be used as a filament in the glass-coating apparatus. To simplify matters further, and because of the lack of the need to remove bubbles in the PαMS, a simpler polymer coating apparatus was usually substituted for that shown in Figure 3. This simpler apparatus consisted of a soldering iron onto which an "omega" shaped wire (dia. = 3-4 mm) was attached. The as-supplied PαMS consisted of small polymer beads (weight≈20 mg) that proved to be approximately the correct size for coating a single STM tip. The polymer bead was then supported by the "omega" shaped wire and heated by the soldering iron. An AC RMS voltage of 110V-120V was applied to the soldering iron, and this yielded a polymer melt of the desired viscosity. During coating, the polymer melt was adjusted to a temperature of approximately 210 ± 10 °C, which is ≈ 100 degrees higher than T_m for this polymer as determined by an iron-constanton thermocouple immersed in the polymer melt. Although the color of as-received PαMS was milky white, films cast from a polymer melt using this procedure were optically transparent.

The coating of etched W and Pt-Ir wires was then accomplished by translating (by

hand) the etched tip through the polymer melt. In the case of polymer-coated Pt-Ir(30%)

wires, the rate of tip translation during the coating process did not appear to be as important

a variable as was found for the glass-coating procedure. A typical tip translation speed was

approximately 0.5 mm/sec, although qualitatively similar STM tip behavior was observed for

tip speeds between 0.25 and 1.0 mm/sec. As in the case of the glass-coated tips, only about

20% of the polymer coated tips were found to be suitable for imaging in the most demanding

electrochemical environments (vide infra).

The second procedure, which is more commonly employed for STM investigations in

our laboratories, involved the use of a 30-35 wt% solution of PαMS in methylene chloride.

This solution proved to possess sufficient viscosity to permit an aliquot to be localized in the

"omega" shaped wire by surface tension. By passing the etched tips through the polymer

membrane, a thin insulating coating was formed. Coated tips were then allowed to dry for ≈1

hr. before they were employed in an STM experiment. Electrochemical characterization

techniques (vide infra) revealed that approximately 80% of the tips fabricated with this

procedure were completely insulated.

This second polymer-coating method has two distinct advantages over the first

technique described above. Firstly, residual methylene chloride in the cast polymer films

acted as a plasticizer to make these coatings less brittle and hence, less susceptible to

fracture. To make use of this advantage, tips employed by the second method were typically

used within 8 hrs. of fabrication. Secondly, the casting procedure was not particularly

sensitive to the rate of tip translation through the polymer membrane, and tips could be

easily prepared without the use of any ancillary equipment.

Characterization

One of the key properties of electrochemical STM tips is the area of metal that is

exposed to the electrolyte. The primary goal of our tip-coating processes is to reduce and

control this exposed area, in order to minimize the faradaic current that is produced from a given tip/sample bias voltage. At the time these procedures were developed, no information was available in the electrochemical STM literature concerning the active area of insulated STM tips. Consequently, there was a need to develop procedures that would allow quantitative measurement of the exposed metal area of various tips. In this work, cyclic voltammetry was found to be a convenient technique for determining the exposed electrochemically active area of the various STM tips. The microelectrode-type behavior of small metal hemispheres and disks has been recently described in the electrochemical literature,[5] with the limiting current and the scan rate dependence of the I-V behavior providing information on the apparent radius and area of the active metal. Recently, Fan and Bard employed similar techniques to evaluate the amount of exposed metal area at their epoxy-coated tips.[6]

The tips of interest were used as the working electrode in a conventional potentiostatically controlled 3-electrode cell. The reference electrode was a saturated calomel electrode, and the counter electrode was a Pt flag. The tips were held in such a way that only the coated ends of the tip were exposed to solution. In most measurements, the electrolyte was an unstirred aqueous solution containing 4.0 m$\underline{M}$ $K_4Fe(CN)_6$ and 1.0 $\underline{M}$ KCl.

Cyclic voltammetry data for an uncoated Pt-Ir tip wire clearly displayed diffusional waves associated with macroelectrode behavior, and, as expected, yielded large ($\approx mm^2$) exposed areas of metal. Figure 4 displays cyclic voltammograms and scanning electron micrographs for several types of tips. Figure 4a depicts the cyclic voltammetry of a typical commercially available (Longreach Scientific Resources, Orr's Island, Maine, U.S.A.) glass coated Pt-Ir(30%) tip. The voltammetry for this tip at a 50 mV/sec sweep rate displayed the steady-state behavior indicative of a microelectrode. Using the well-known expression for the limiting current at a hemispherical microelectrode[5] ($I_{lim} = 2\pi nFDCR$, Eqn. 2 of Chap. 2), the area of exposed metal was estimated to be 660 μm^2 ($I_{lim} \approx 20$ nA). The size of the area

seen at the tip's apex in the SEM photograph qualitatively agrees with the electrochemically determined area. This conclusion was substantiated by energy-dispersive x-ray analysis (EDAX), which indicated that the exposed metal consisted of Pt-Ir.

The tips shown in Figures 4b and 4c were fully insulated with polymer and glass, respectively. In contrast to the large faradaic current seen for the specimens used in Figure 4a, the cyclic voltammograms for these tips are featureless (except for spurious electrical noise) to less than 0.5 pA of faradaic current, even in the presence of 4 m$\underline{M}$ Fe(CN)$_6^{4-}$. A steady-state limiting current of 1 pA would correspond to an active area of $\approx$100 Å^2, indicating that an upper limit of 100 Å^2 can be established for the exposed metal area of these tips. Consistently, at the limiting resolution of the SEM ($\approx$1 μm), the underlying metal in the tips of Figures 4b and 4c was completely obscured by the coatings. In addition, the characteristic x-ray lines of Pt and Ir were not observed in EDAX analysis. We thus concluded that the tips were completely coated with insulation, and we had achieved our initial goal of eliminating the faradaic currents at the metal tip. The ultimate success of this procedure relies on the fact that the tip is essentially completely insulated by the coating, but the insulating layer is thin enough so that with one further preparative step, tunneling processes can still occur in a conventional STM arrangement. Examples of this process are described in the next section.

Imaging

Tips that were fully coated with insulation, as evidenced by the presence of the voltammetric behavior depicted in Figures 4b or 4c, were prepared for imaging in solution by mounting them in the scanning tunneling microscope that was described in Chapter 3. Highly ordered pyrolytic graphite (HOPG) was usually employed as an electrode material. Typically, a controllable tunneling gap could not be formed when conducting substrates were approached in air with normal biases of 200-500 mV. Occasionally, feedback control of

the tunneling current setpoint could be maintained after approaching. In these cases, tip/sample contact was evident in the distorted current traces that were obtained when the X-Y scans were activated. Tips processed in this manner apparently maintained enough insulating material at the apex to interfere with feedback control of the tunneling gap. In order to circumvent this problem, a field-emission process was performed in an air ambient. The coated tips were moved towards the sample surface in ≈500 Å steps by voltage pulses sent to the stepper motor that drives the STM's approach mechanics. The tip's potential during approach was maintained at a large positive value (+15 V).

Despite the fact that these tips were totally electrically insulated to faradaic current flow in the aqueous $Fe(CN)_6^{4-}$ electrolyte, a tunneling current of ca 1 nA was sensed by the instrument upon approach to the graphite surface. Upon sensing this tunneling current, the pulse train to the stepper motor was electronically deactivated, the piezoelectric tube scanner was fully retracted along its Z axis (≈ 0.75 μm), and the potential on the tip was reduced to a value suitable for imaging (≈ 300 mV). The voltage that controlled the retraction of the tube was then capacitively discharged, and the tip subsequently relaxed back into tunneling range. At this point, the tip was suitable for use both in conventional STM imaging experiments and for use in electrochemical STM experiments.

The physics associated with the approach/retraction process described above are uncertain. The process is definitely useful to prohibit prolonged intimate physical contact between the tip and the sample. Additionally, we speculate that dielectric breakdown of the coated tips may expose enough metal area so that tunneling then occurs. We call this step in the preparation of tips "field emission." We note that a similar procedure has been utilized to clean the apex of commercially available glass coated tips that had been insulated further by an SiO layer.[7] The tips prepared in this manner were used to perform localized electrodeposition.

In experiments in which HOPG was approached in air, approximately 10-20% of the

tips prepared with these procedures still did not allow the Z-piezo voltage to vary smoothly with changes in the tunneling current setpoint. In these cases, images could not be obtained, presumably because of an excessively thick residual coating at the apex of the tip. It is interesting to note that virtually all tips that enabled feedback control and that successfully completed the "field emission" process yielded atomic resolution images of HOPG in air. In contrast, in our trials, only 60-70% of uncoated Pt-Ir(30%) tips yielded atomic resolution images of HOPG in air. This observation suggests that a sharpening effect is also occurring as a result of the field emission process. One possible explanation of this phenomena might involve the field-assisted transport of metal atoms along a fissure in the coating.

The success of the tip insulation process was evidenced by the low faradaic current level between the tip and sample during STM tunneling and imaging experiments. These tips typically suppressed faradaic currents, even in highly conducting electrolytes, to values of less than 0.5 nA. Consequently, STM images (employing conventional fast-scan imaging techniques) could be readily obtained in a variety of electrolyte solutions. However, the fragile nature of these tips, and the experimentally demanding constraints on tip-insulation quality, were repeatedly evidenced by the fact that if the tip physically contacted the sample, then faradaic currents would completely overwhelm the tunneling current (i.e., $I_{faradaic} \gg 1$ nA), and would disable feedback control at tip-sample biases as small as 10 mV. Figure 5a displays a fast-scan image of HOPG, obtained with a polymer-coated tungsten tip, in an aqueous solution containing 0.1 $\underline{M}$ Fe(CN)$_6^{4-}$, 0.1 $\underline{M}$ Fe(CN)$_6^{3-}$, 1.0 $\underline{M}$ KCl. Carbon atoms, separated by $\approx$ 2.5 Å are clearly evident in this image. It is interesting to note that this image is virtually identical to an image of the same surface obtained in an air ambient (Fig. 3a, Chap. 3) despite the fact that the image presented in Figure 5a was obtained at a surface in contact with a redox-active electrolyte. Evidently, the in situ HOPG surface is free of adsorbates that can be detected by the STM imaging process. This observation is in accord

with the expected chemical inertness of the basal plane surfaces of graphite.

Figure 5b is a fast-scan image of MoS_2, obtained with a glass-coated Pt-Ir tip, in an aqueous 0.5 $\underline{M}$ $NaClO_4$ solution. Once again, the image is evidently free of adsorbates, and is quite similar to images of MoS_2 we have obtained in air. STM images similar to that shown in Figure 5 were obtained over a range of tip/sample biases in a variety of electrolytes. To date, we have successfully imaged HOPG at tip/sample biases of ± 1.5 V in pure H_2O and in aqueous 1 $\underline{M}$ NaCl, and at biases of ± 0.8 V in aqueous solutions of 0.1 $\underline{M}$ $Fe(CN)_6^{4-}$, 0.1 $\underline{M}$ $Fe(CN)_6^{3-}$, 1.0 $\underline{M}$ KCl. These data represent the first atomic resolution images of an electrode surface in contact with liquids containing both forms of a reversible redox couple. Similar capabilities have been demonstrated by both polymer and glass-coated tips. Atomic resolution images of MoS_2 have been acquired in aqueous 0.5 $\underline{M}$ $NaClO_4$ at positive tip biases as large as 0.5 V.

Distance Dependence of the Tip/Sample Current

It is of interest to determine the relationship between the observed current and the tip/sample separation for glass and polymer-coated tips. Current versus tip/sample separation (s-s$_o$) data were obtained by translating the tip toward the sample at a rate of less than 50 Å/s. The I vs. (s-s$_o$) curves were not significantly dependent on the tip translation rate for speeds slower than this value. The approach was automatically halted by the feedback circuit as the tip was brought into tunneling range. Figure 6 shows representative data that we have obtained for polymer/W tips. For an HOPG sample in an aqueous solution containing 5 $m\underline{M}$ $Fe(CN)_6^{3-/4-}$ and 50 $m\underline{M}$ KCl, currents were less than the noise in the current measurement (i.e., < 10 pA) for tip/sample separations larger than approx 50 Å (curve A). In solutions containing larger concentrations of the redox active ions (0.1 $\underline{M}$ $Fe(CN)_6^{3-/4-}$, 1 $\underline{M}$ KCl), the maximum faradaic currents at polymer/W tips were 200-500 pA (curve B). Qualitatively similar behavior was observed for polymer/W tips with a Pt sample (curve C).

According to the expression for the limiting current to a hemispherical microelectrode, the limiting currents of 200-500 pA correspond to exposed metal areas of $\approx 10^4$ - 10^5 Å^2.[5]

In contrast, the behavior of the tip/sample faradaic current for glass-coated Pt-Ir tips is shown in Figure 7. Tips that survived the field-emission process described above typically displayed currents < 10 pA at all tip/sample displacements greater than ≈ 50 Å in 0.1 M $Fe(CN)_6^{3-/4-}$, 1 $\underline{M}$ KCl (curve A). This limiting current corresponds to < 30 Å^2 of exposed metal area. On one occasion the faradaic current between the tip and sample was larger than the noise level in the current preamplifier, and its distance dependence was investigated. Curves B and C in Figure 7 show the measured current versus distance relationship for this tip and a Pt sample in solutions containing 4 m$\underline{M}$ $Fe(CN)_6^{3-/4-}$ (40 m$\underline{M}$ KCl), and 0.1 $\underline{M}$ $Fe(CN)_6^{3-/4-}$ (1 $\underline{M}$ KCl), respectively.

The behavior of the two types of coated tips is evidently quite different. At the larger redox ion concentrations, the polymer/W tips displayed a dip in the faradaic current at distances within 0.1 μm from the surface. In contrast, the glass-coated tips never displayed such a dip. In fact, for the case of curve C in Figure 7, the faradaic current increased with decreasing tip/sample separation until the current setpoint (5 nA) was reached. Assuming that the thin-layer current formalism introduced in Chapter 2 is applicable, a plot of I vs. $(s-s_o)^{-1}$ should allow the measurement of the effective electrode radii of the thin-layer cell electrodes, in accordance with Equation 1.

$$I_{lim} = 2\pi FDCR^2/(s-s_o) \tag{1}$$

In writing Eqn. 1 we have assumed that the electrode areas may be described as disks $(A=\pi R^2)$, and we have taken $s-s_o$ to be the interelectrode spacing. A plot of the data for $s-s_o$ values from 10 nm to 50 nm is shown in Figure 8. From the slope of the plot, and taking D = 7.9 X 10^{-6} cm/sec for both forms of the redox couple,[8] the effective radii of the thin layer cell

electrodes were determined to be ≈ 29 nm. This result is in surprisingly good agreement with the radius (6.8 nm) determined by treating the tip as a disk-shaped microelectrode (I_{lim} = 4FDCR, Ref. 5) with a limiting current value of that found at large s-s_o (210 pA). Though thin-layer currents were evident for this glass-coated tip, the analysis presented above is not rigorous since the +60 mV tip potential that was employed was not sufficient to produce a true limiting current.

The dip observed for the polymer/W tips with the larger redox ion concentrations is not understood at this time. One possible explanation for the observed behavior was suggested in a recent paper by Christenson and Claesson.[9] Their work involved the observation of cavitation between hydrophobic surfaces in pure water with a crossed-cylinder microforce balance. Interferometric measurements revealed that small vapor cavities formed to minimize the surface free energy of the system when the hydrophobic surfaces were brought into contact. These cavities persisted for separation distances of larger than 1 μm. The cavities could be nucleated, however, only when the surfaces were first brought into contact and then separated.

Thin films of PαMS cast onto glass slides are indeed hydrophobic, exhibiting contact angles greater than 90°. However, the dip in faradaic current that we observe does not persist to s-s_o values larger than ≈ 0.3 μm. Furthermore, the dip is observed with the first approach to either HOPG or Pt surfaces; initial contact between the tip and the sample is not required. The first objection may be addressed by considering that our geometry is significantly different from that of Christenson and Claesson. Also, the hydrophobicity of our tips and samples are undoubtedly different from their Langmuir-Blodgett deposited fluorocarbon monolayers.[8] These differences might also provide enough driving force for cavity nucleation without the need for tip/sample contact.

In order to explore the possibility of cavitation, we performed several additional experiments. In an effort to reduce the surface tension between the PαMS surfaces and the

solution, a methanolic electrolyte solution was employed. Because of the low solubility of $Fe(CN)_6^{3-/4-}$ salts in methanol, we opted to use a 26% methanol in water solution containing 25 m$\underline{M}$ $Fe(CN)_6^{3-/4-}$ and 0.25 $\underline{M}$ KCl. This solution exhibited a significantly lower contact angle ($\approx 45°$) on planar PαMS surfaces, indicating that the interfacial surface tension had been reduced. However, measurements of the distance dependence of the tip/sample current with polymer/W tips and HOPG surfaces in the methanolic solution were quite similar to those made in the aqueous solution. The methanol fraction evidently lowered the viscosity of the solution, but the nonzero contact angle indicated that significant surface tension still remained at the polymer/solution interface. Consequently, these results could not be interpreted to mean that cavitation does not occur in this system.

To gain access to 100% methanol solutions, which readily spread on planar PαMS surfaces (contact angle of $\approx 0°$), $Co(bpy)_3Cl_2$ and $Co(bpy)_3Cl_3$ were used as redox compounds. The solubility of these compounds in both water and methanol was sufficient to allow 25 m$\underline{M}$ $Co(bpy)_3^{3+/2+}$, 0.25 $\underline{M}$ LiCl solutions to be made. Investigation of the distance dependence of the tip/sample current in the aqueous solution yielded an unexpected result for polymer/W tips and an HOPG sample. In this instance the measured current changed from an $s-s_0$ independent value (4 nA with tip at + 100 mV in one case) to the tunneling current setpoint (6 nA) over a 20 Å distance without evidence of a pronounced dip. Furthermore, within the resolution of the experiment, thin-layer current enhancements were not observed.

Unfortunately, these last two sets of experiments, employing 26% MeOH solutions and $Co(bpy)_3^{3+/2+}$ as redox active ions, respectively, were each performed with only two tips. The data for the aqueous $Co(bpy)_3^{3+/2+}$ solution are especially suspect in that relatively large faradaic currents were measured at large tip/sample separations, indicating that the tip had not been well insulated by the polymer coating. Unfortunately, because of the observed reproducibility of the polymer-coating process, the degree of insulation of these tips was not

independently checked prior to the field-emission process. On rare occasions we have observed similar behavior for polymer/W tips in aqueous 0.1 $\underline{M}$ Fe(CN)$_6^{3-/4-}$. If the exposed metal was distributed more than a few microns away from the apex of the tip, then variations in s-s$_0$ achieved in the STM would not be expected to alter significantly the tip/sample faradaic current. Conversely, the exposed metal must be distributed near the apex of the tip in order to observe the dip phenomena. Also, assuming kinetic effects are not limiting, the dimensions of the tips that displayed the dip are at least a factor of ten smaller than the distance over which the dip occurs (R = 0.004 to 0.01 μm for limiting current between 200 and 500 pA: *vide supra*).

The origins of the current dip for PαMS-coated tips is not known at this time. It is important to understand the phenomenon, and determine if cavitation does occur, to be sure that true *in situ* investigations can be performed with these polymer-coated tips. A more complete investigation would involve performing more experimental work with various redox couple/solution combinations. Additionally, the polymer coating could be derivatized (e.g., sulfonated) in order to alter its surface charge and wettability properties. In contrast, the glass-coated tips have never displayed the current dip phenomenon. In fact, in one example, we have observed thin-layer behavior. Therefore, it seems that we can exclude the possibility of cavity formation for these tips. Though difficult to fabricate, glass-coated tips are clearly valuable for *in situ* STM investigations since faradaic currents can be virtually eliminated. The ability to employ large tip/sample biases while excluding faradaic currents may enable *in situ* investigations of the electronic structure of electrode surfaces via dl/dV techniques.

Summary

Procedures that yield insulated Pt-Ir and W tips have been described. Tips can be prepared with either glass or polymer layers that suppress faradaic currents at most

tip/sample biases, even in aqueous solutions containing high concentrations of redox active species. A field-emission process has been described that is quite useful for cleaning the apex of these tips for *in situ* STM investigations. Tips that *successfully completed the* insulation and field-emission procedures yielded atomic resolution STM images in a variety of electrolyte solutions. To date, we have succeeded in obtaining images of HOPG in DI water and aqueous 1.0 $\underline{M}$ NaCl at tip biases of ±1.5 V, and in aqueous solutions simultaneously containing 0.1 $\underline{M}$ Fe(CN)$_6^{3-}$, 0.1 $\underline{M}$ Fe(CN)$_6^{4-}$ and 1.0 $\underline{M}$ NaCl at biases of ±0.8 V. This latter experiment represents the most dramatic suppression of faradaic current to date, and to our knowledge, is the only example of STM imaging in electrolytes containing such high concentrations of redox species. MoS$_2$ surfaces have also been imaged with atomic resolution in 0.5 M NaClO4 at biases as large as +0.5 V. The need to reproducibly fabricate insulated STM tips that enable the imaging capabilities described above prompted us to develop the tip preparation schemes that we have described. These procedures should facilitate the continuing use of STM in a variety of *in situ* electrochemical applications. Furthermore, investigations of the distance dependence of the tip/sample current have provided information concerning the nature of the tip/sample junction while performing STM investigations in electrolytic solutions.

References

1. (a) Guld, C. *Med. Electron. Biol. Engr.* **1964**, 2, 317-27. (b) Wolbarsht, M.L.; MacNichol, E.F.; Wagner, H.G. *Science* **1960**, 132, 1309-10.

2. Bansal, N.P.; Doremus, R.H. *Handbook of Glass Properties*, 1986, Academic Press, Orlando.

3. Weast, R.C. (ed.) *Handbook of Chemistry and Physics*, 1975, 56th edn., CRC Press, Cleveland.

4. Penner, R.M.; Heben, M.J.; Lewis, N.S. *Anal. Chem.* **1989**, 61, 1630-36.

5. (a) Dayton, M.A.; Brown, J.C.; Stutts, K.J.; Wightman, R.M. *Anal. Chem.* 1980, 52, 946-950. (b) Aoki, K.; Akimoto, K.; Tokuda, K.; Matsuda, H.; Osteryoung, J. *J. Electroanal. Chem.* **1984**, 171, 219-30. (c) Galus, Z. *Fundamentals of Electrochemical Analysis*; Halsted Press: New York, 1976; Chapter 4.

6. Fan, F.F.; Bard, A.J. *J. Electrochem. Soc.* **1989**, 136(11), 3216-22.

7. Schneir, J.; Hansma, P.K.; Elings, V.;Gurley, J.; Wickramasinghe, K.; Sonnenfeld, R. *S.P.I.E. Conference Proceedings*, **1988**, 16, 897-900..

8. Hepel, T.; Osteryoung, J. *J. Phys. Chem.* **1982**, 88, 1406-11.

9. Christenson ,H.K.; Claesson, P.M. *Science* **1988**, 239, 390-392.

Figure 1:

(a) Current versus time curve for a 0.020" Pt-Ir(30%) wire etched in an unstirred aqueous solution that contained 6 $\underline{M}$ NaCN and 2 $\underline{M}$ KOH. The etching voltage was a 25 V_{RMS} AC potential. A description of stage I and stage II etching is found in the text. (b) Diagrammatic representation of tip shapes found after emersion at points labelled A, B, and STOP in part (a) of this figure.

(a)
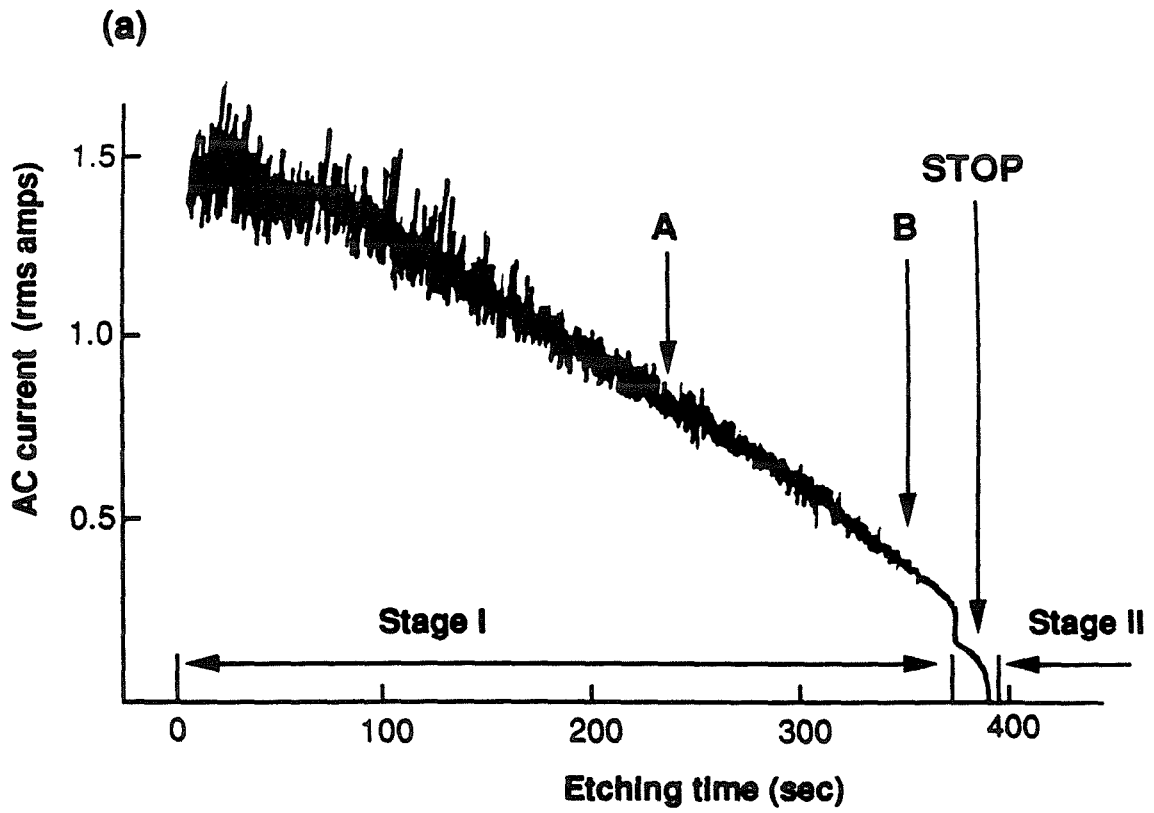
(b)
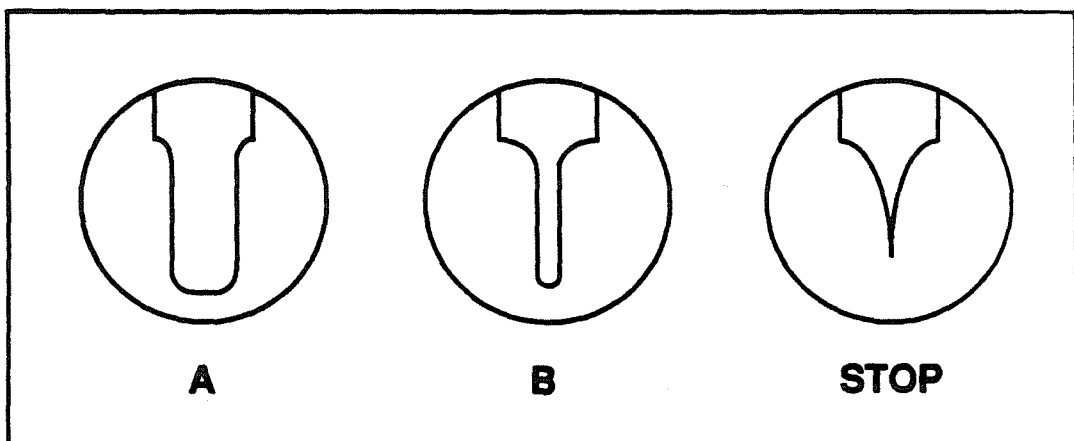
Figure 2:

Scanning electron micrographs of the apexes of (a) a Pt-Ir(30%) wire and of a (b) W wire

after electrochemical etching.

(a)

(b)

Figure 3:

Schematic diagram of apparatus used to apply glass layers to etched Pt-Ir(30%) wires. A

complete description may be found in the text.

Glass
bead

STM tip

Collet for
mounting
of tips

Platinum
filament

thermocouple
wires

Y

Z

X

Translation

Enlargement

Glass bell jar

Connection between
posts for water
circulation

Brass posts provide
support and electrical
conductivity

Feed through for
thermocouple

To vacuum pump for
bell jar evacuation

Cooling water
inlet and outlet

Leads for resistive
heating of platinum
filament

Figure 4:

Comparison of cyclic voltammetry, electrochemically determined areas and scanning

electron micrographs for several coated STM tips. (a) Commercially available glass-coated

tip, (b) fully insulated glass-coated tip, (c) fully insulated polymer-coated tip. Cyclic

voltammetry was performed at 50 mV/s in an unstirred aqueous solution containing 4 m$\underline{M}$
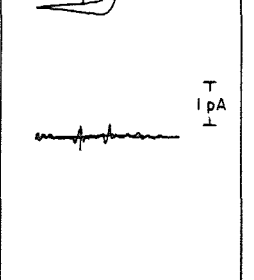
$K_4Fe(CN)_6$ and 1 $\underline{M}$ KCl.
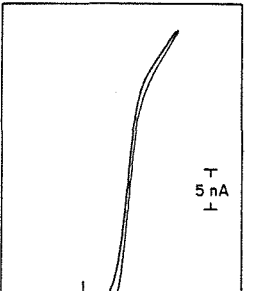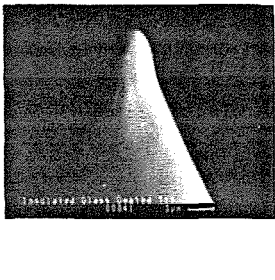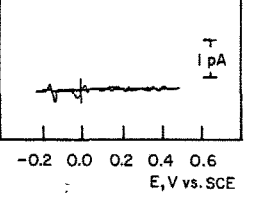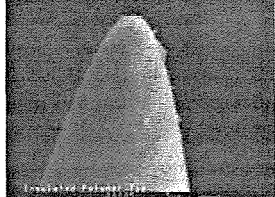
Tip description	Cyclic voltammogram	Exposed metal area	SEM Image
(a) Commercial glass coated		6.6×10^{10} A^2	
(b) Glass coated		<100 A^2	
(c) Polymer coated		<100 A^2	

Figure 5:

(a) Atomic resolution image of a highly ordered pyrolytic graphite surface in contact with an aqueous solution containing 0.1 $\underline{M}$ Fe(CN)$_6^{4-}$, 0.1 $\underline{M}$ Fe(CN)$_6^{3-}$,and 1 $\underline{M}$ KCl. A polymer-coated tungsten tip was used at a potential of +200 mV. (b) Atomic resolution image of MoS$_2$ in contact with an aqueous 0.5 $\underline{M}$ NaClO$_4$ solution. A glass-coated Pt-Ir, at a potential of +300 mV, was employed. Both images were obtained with fast-scan methods with a 1 nA tunneling current.

(a)

~5 Å

(b)

~5 Å
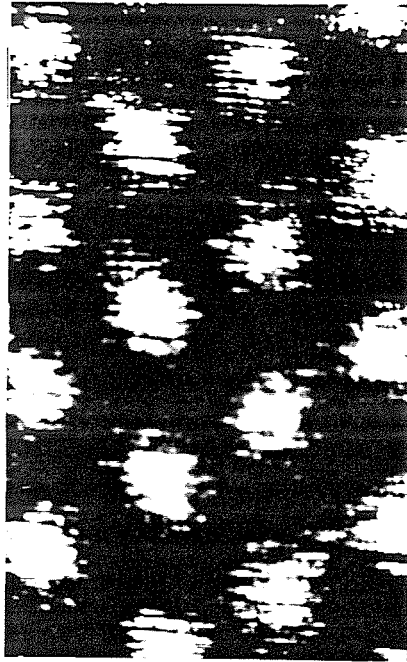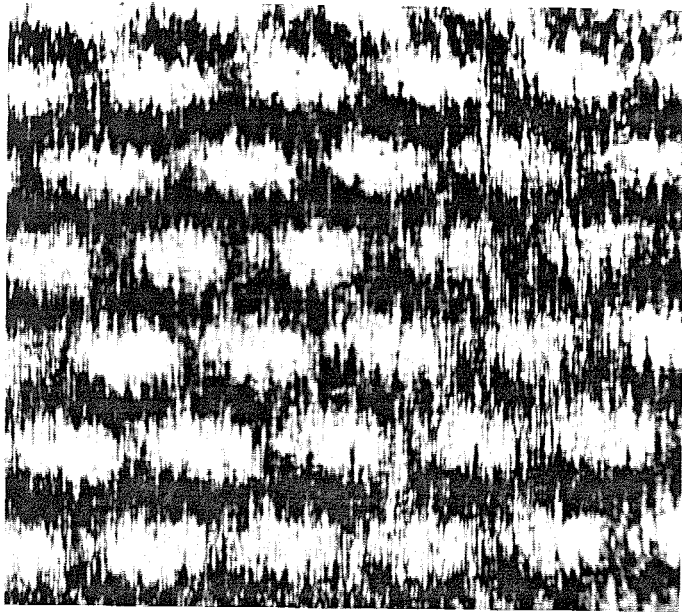
Figure 6:

Typical current vs. tip/sample displacement, s-s$_o$, curves for polymer/W tips. Tip translation speed < 50 Å/s, bias = +250 mV, tunneling current setpoint = 1.0 nA. Current noise of ca 20 pA ha been removed for clarity. Curve A: HOPG sample in contact with 5 m$\underline{M}$ Fe(CN)$_6^{3-/4-}$, 50 m$\underline{M}$ KCl; Curve B: HOPG sample in contact with 0.1 $\underline{M}$ Fe(CN)$_6^{3-/4-}$, 1.0 $\underline{M}$ KCl; Mechanically polished Pt(111) sample (polished with 1.0, 0.3, 0.05 μm alumina powders prior to use) in contact with 0.1 $\underline{M}$ Fe(CN)$_6^{3-/4-}$, 1.0 $\underline{M}$ KCl.

A: Polymer/W tip, HOPG sample, 5 m$\underline{M}$ Fe(CN)$_6^{3-/4-}$ / 50 m$\underline{M}$ KCl.
B: Polymer/W tip, HOPG sample, 0.1 $\underline{M}$ Fe(CN)$_6^{3-/4-}$ / 1.0 $\underline{M}$ KCl.
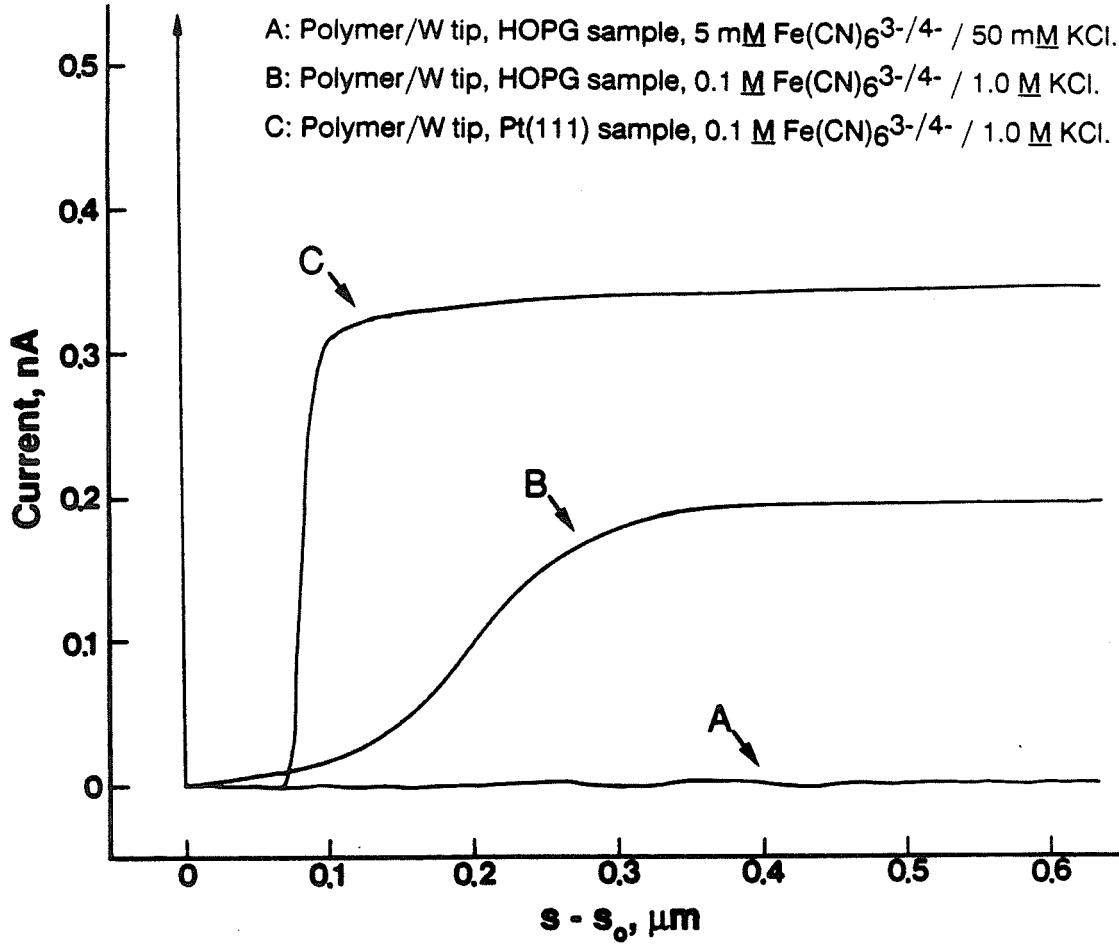C: Polymer/W tip, Pt(111) sample, 0.1 $\underline{M}$ Fe(CN)$_6^{3-/4-}$ / 1.0 $\underline{M}$ KCl.

Figure 7:

Current vs. tip/sample displacement, s-s_0, curves for glass/Pt-Ir tips. Tip translation speed

< 50 Å/s. Current noise of ca 20 pA has been removed for clarity. Curve A: HOPG sample in

contact with 0.1 $\underline{M}$ Fe(CN)$_6$$^{3-/4-}$, 1.0 $\underline{M}$ KCl. Tip bias = +250 mV, tunneling current setpoint

= 1.0 nA; Curves B and C: HOPG sample in contact with 4 m$\underline{M}$ Fe(CN)$_6$$^{3-/4-}$ (40 m$\underline{M}$ KCl) and

0.1 $\underline{M}$ Fe(CN)$_6$$^{3-/4-}$ (1.0 $\underline{M}$ KCl), respectively. Tip biases and tunneling current setpoints were

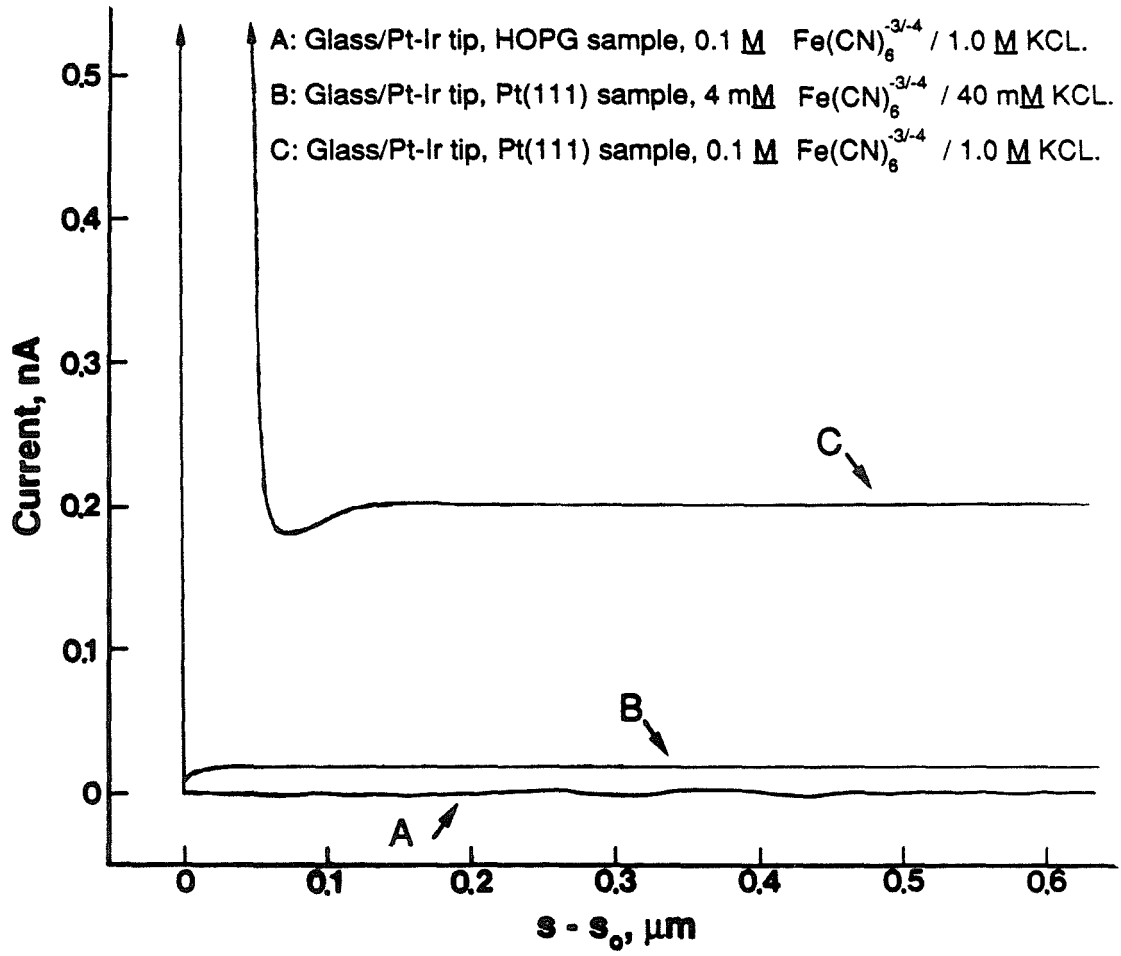+400 mV and 0.8 nA for curve B and +60 mV and 5 nA for curve C.

A: Glass/Pt-Ir tip, HOPG sample, 0.1 $\underline{M}$ Fe(CN)$_6^{-3/-4}$ / 1.0 $\underline{M}$ KCL.

B: Glass/Pt-Ir tip, Pt(111) sample, 4 m$\underline{M}$ Fe(CN)$_6^{-3/-4}$ / 40 m$\underline{M}$ KCL.

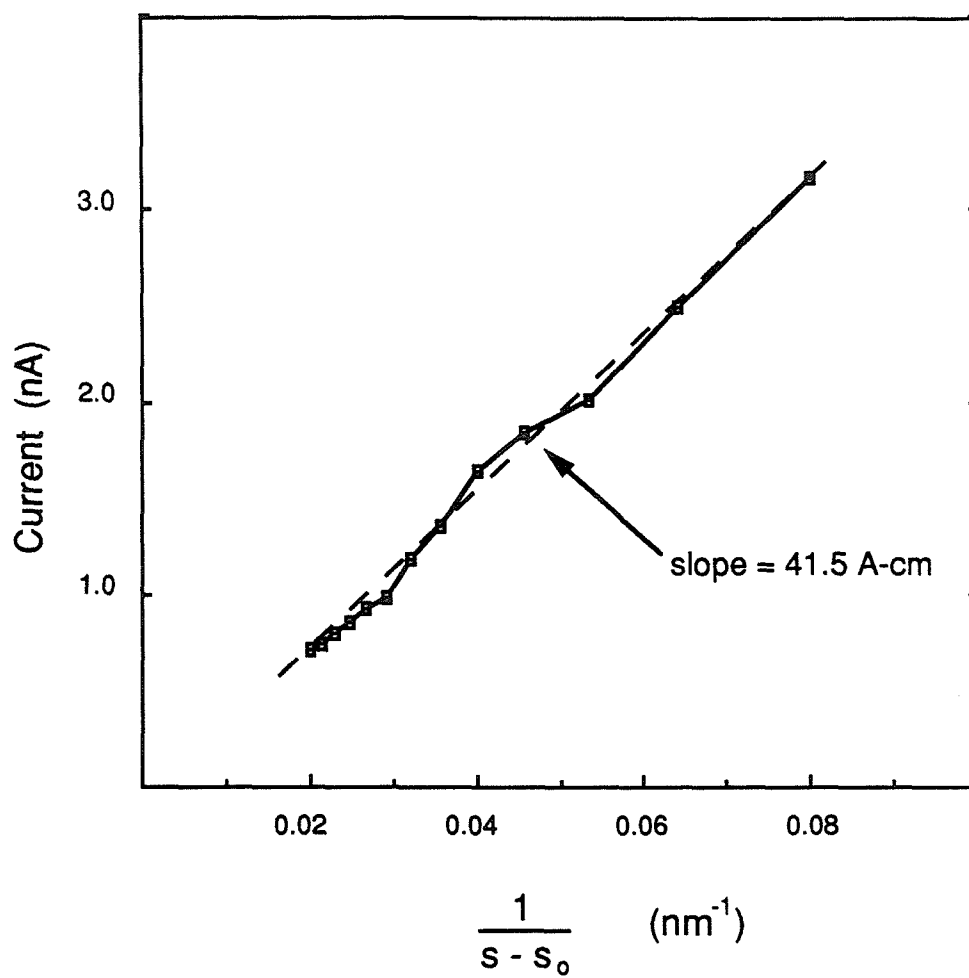C: Glass/Pt-Ir tip, Pt(111) sample, 0.1 $\underline{M}$ Fe(CN)$_6^{-3/-4}$ / 1.0 $\underline{M}$ KCL.

Figure 8:

Plot of measured current vs. $1/(s-s_0)$ for curve C of Figure 7. The slope of the plot was

determined to be 41.5 A-cm.

Figure showing Current (nA) versus $\frac{1}{s - s_o}$ (nm^{-1}), with slope = 41.5 A-cm

Chapter 5

Preparation and Characterization of Conical and Hemispherical Ultramicroelectrodes

INTRODUCTION

The construction of Pt, Au and graphite ultramicrodisk electrodes with element radii as small as 0.1 μm has become routine in many electrochemical laboratories.[1] The inherently small RC time constants of ultramicroelectrodes (UMEs) allow fast, transient electrochemical experiments to be performed,[2] and the low total current allows voltammetry to be performed in highly resistive media.[2a,3] Additionally, mass transport to a UME is extremely rapid, and this permits the determination of fast heterogeneous rate constants using steady-state voltammetry.[4] However, the interpretation of steady-state electrochemical results for the disk geometry is complicated by the fact that the steady-state current density near the edge of a microdisk can be much greater than at the center of the disk.[5] Consequently, the mathematical analysis of cyclic voltammetry and chronoamperometry at microdisks is difficult, and frequently involves approximations.[5]

UMEs possessing a hemispherical geometry would circumvent this problem, since the steady-state current density at a hemispherical surface is uniform. Consequently, simplified mathematical treatments are available for this electrode geometry.[6] Unfortunately, conventional UME construction techniques are not well suited to preparing hemispherical ultramicroelectrodes.[1] Thus, experimental results for this UME geometry, despite its obvious theoretical advantages, are notably absent from the literature.

This chapter describes modifications to the STM tip coating procedures introduced in Chapter 4, which produce both glass and polymer-insulated Pt-Ir UMEs. These UMEs typically possess cone-hemisphere radii in the range 0.5 μm-10 μm, though electrodes with radii as small as 1.5 nm have been fabricated (*vide infra*). Data for the electrochemical characterization of these electrodes by cyclic voltammetry and chronoamperometry are also presented. The chronoamperometry data for the conical UME's have been analyzed in terms of an expression that combines linear diffusion and radial diffusion terms. These

measurements have yielded the first experimental information on the diffusional properties of cone-shaped microelectrodes. The chapter concludes with an example of the application of these UMEs to the measurement of fast heterogeneous rate constants.

Methods and Materials

Reagent grade $K_4Fe(CN)_6$, KCl, KOH, and Na_2SO_4 (all from J.T. Baker) and NaCN (Mallinckrodt) were used as received. $Ru(NH_3)_6(PF_6)_3$ was obtained as a precipitate from an aqueous solution of $Ru(NH_3)_6Cl_3$ (Strem) upon addition of NH_4PF_6. The white precipitate was washed with cold, dilute aqueous HPF_6 solution. Both the product, and reagent grade KPF_6 (Alfa), were recrystallized from a warm (40 °C) dilute HPF_6 solution. Aqueous solutions were prepared using 18 MΩ-cm deionized water obtained from a Bronsted Nanopure system. Poly-(α-methylstyrene) (Aldrich, MW = 60,000) was used as received. Pt(70%)-Ir(30%) wire (dia. = 0.020") was obtained from Englehard Industries.

Chronoamperometry and cyclic voltammetry were performed using a Princeton Applied Research (PAR) Model 173 potentiostat in conjunction with a PAR Model 175 voltage programmer. Cyclic voltammograms at scan rates below 500 mV s^{-1} were recorded on a Houston Instruments Model 2000 X-Y recorder. Data from faster voltammetric sweeps, or from current-time transients, were recorded on a Nicolet Model 2090 III digital storage oscilloscope. DC currents were measured using a Keithley Model 427 Current Amplifier, and AC currents were measured with a Keithley Model 177 Voltmeter.

Electrochemical cells for most experiments were of a conventional one-compartment design. A fritted compartment was used to isolate the reference electrode in measurements of the rate constant for $Ru(NH_3)_6^{3+}$ reduction (*vide infra*). All microelectrode experiments were performed using a conventional three-electrode configuration employing a saturated calomel reference electrode (SCE).

Scanning electron microscopy and energy dispersive x-ray (EDX) elemental analysis were performed with a CamScan SEM equipped with a Tracor-Northern x-ray analyzer and data station. A typical accelerating voltage for these measurements was 20 kV. Prior to SEM examination, all electrodes were coated with ca 200 Å of gold using a plasma coater. Spacial profile analysis of Pt using EDX methods was not impeded by the presence of this Au coating.

Tip Etching

The electrochemical etching bath consisted of an unstirred solution of 2 $\underline{M}$ NaOH and 6 $\underline{M}$ KCN. The cyanide facilitated the complexation and dissolution of metal from the immersed wire, and the NaOH inhibited the formation of HCN. All etching was performed in a fume hood.

The apparatus used for etching of Pt-Ir(30%), and the procedures that were used to obtain sharp and reproducible etched wires, were previously presented in Chapter 4. An AC voltage of 25 V RMS was applied between an immersed Pt-Ir wire and a C counter electrode, and the depth of immersion was adjusted until the average current was 1.25 A RMS. Etching was terminated when the desired conical geometry and aspect ratio was obtained (*vide infra*).

Tip Coating

Glass-Coating Procedures. A coating apparatus was used to apply controllable, uniform coatings of nonporous glass insulation to the etched Pt-Ir tips. A description of the apparatus, and of procedures used for degassing the glass bead and for manipulation of the Pt-Ir wire, may be found in Chapter 4. Soda-lime glass (Corning Glass #0080) was cleaned with i-C_3H_7OH and deionized water, and was then used for coating the Pt(70%)-Ir(30%) wire.

Tip translation speeds in the range 0.3-0.5 mm/min and glass temperatures of 1350±20 °C were used to form the UME's studied in this work.

Polymer-Coating Procedures. The procedure used for forming UMEs with polymer coatings was qualitatively similar to that used for glass coating. Because of the lower temperatures required for the polymer-coating process, and the lack of the need to remove bubbles from the PαMS melt, a simpler procedure utilizing a soldering iron (Ungar, 22W) with an "omega" wire (diam. ≈4mm) was usually employed. This polymer-coating procedure, unlike the one we normally employ for *in situ* STM investigations (Chap. 4), produced the abrupt polymer/metal interfaces required for well behaved electrochemical responses. In contrast to the glass-coating process, the rate of tip translation during the polymer-coating step did not appear to be an important variable in determining the final coating morphology. During coating, the polymer melt was adjusted to a temperature of 190-205 °C. Within this temperature range, the cone-hemisphere radius decreased from 10 μm to 0.5 μm as the temperature was increased.

Electrochemical Pretreatment and Surface Conductivity

Following glass or polymer coating, reversible steady-state voltammograms in the $Fe(CN)_6^{4-}$ test solution were not always observed initially. Instead, for approximately 10% of the UMEs with either type of insulation, the cyclic voltammetry appeared to be quasi-reversible, with plots of $log[(i_l-i)/i]$ vs. $E-E_{1/2}$ yielding slopes of 80-90 mV.[4f] However, when such electrodes were potentiostatted at -0.6 V vs. SCE for several minutes, the apparent reversibility of the $Fe(CN)_6^{4-/3-}$ wave usually improved. Slopes of $log[(i_l-i)/i]$ vs. $E-E_{1/2}$ were then close to 60 mV, as expected for reversible electron transfer processes (21). This observation suggests that a surface oxide layer was present at the exposed Pt-Ir surface, and was possibly introduced during the preceding electrochemical etch. Electrochemical reduction of this oxide then enabled routine voltammetry to be performed with these UME's.

An additional complication was sometimes observed with glass-coated UME's. In some cases, the cyclic voltammetry of the redox species of interest was superimposed on steeply sloping background currents. This observation suggested the presence of a parallel resistance in the electrochemical equivalent circuit. This current was found to result from a surface conductivity effect. Insulating the exposed metal shaft of such electrodes with epoxy was found to remove the sloping background component from these voltammograms, and resulted in normal, well-behaved electrochemical responses.

Properties of Etched Pt-Ir Tips

The coating of Pt-Ir metal tips by glass and polymer layers was found to be a function of the sharpness, surface roughness, and cone angle of the etched tips. Extremely sharp metal tips (tip radius < 1 μm) facilitated the polymer and glass coating processes, and these tips resulted in the conical UME geometries of interest in this study. The tip-etching procedures employed (Chap. 4) readily yielded tip radii in the range 0.5-1.0 μm.

An SEM image of a typical etched (but uncoated) Pt-Ir tip is shown in Figure 1. The geometry of this tip was close to conical, with an aspect ratio (height/base diameter) of α=1.3 and a radius of curvature at the tip apex of 1.0 μm. Typical aspect ratios were found to be 1.2-1.3. Varying the termination time of the etching process (Chap 4.) yielded "sharp" tips possessing aspect ratios from 0.5 to 10. Although we have found that an aspect ratio of 1.2-1.4 is optimal for obtaining polymer and glass-coated UME's, the etching procedure is thus capable of producing other types of tips, if desired, for use in other applications.

The surface of the hemispherical tip in Figure 1 was observed to be smooth to the limiting resolution of the SEM. This indicates that the metal underwent an effective electropolishing process during etching.[7] For this reason, further polishing of the metal surface, even after insulating with glass or polymer coatings, was not necessary. Also, the longitudinal grooves revealed by the SEM images of the tip shaft were not detrimental to the

final UME performance characteristics, because this area was insulated from contact with the electrolyte by the glass/polymer coating process.

SEM Characterization of UME Tips

Figure 2 displays SEM images of representative Pt-Ir microelectrodes. In the glass-coated UME shown in Figure 2a, the interface between the glass insulator and the exposed metal surface is clearly visible. Notably, although this interface is not geometrically uniform, no cracks or other defects in the glass-metal seal are evident. In SEM images of polymer-coated UMEs, such as that shown in Figure 2b, a well-defined interface was not apparent between the polymer insulator and the exposed metal surface. The difficulty in resolving this interface implies that there was an intimate seal between these two components of the UME. Defects, cracks, and other mechanical deformations were similarly absent in SEM images of other glass-coated and polymer-coated UMEs. Thus, it appears that both the glass and polymer coatings adhere extremely well to the etched Pt-Ir surface. This feature is critical for making well-defined microelectrodes using any tip insulation process.

The approximate location of the insulator-metal boundary for polymer-coated tips was determined using both SEM imaging and EDX spectroscopy. The increased brightness near the apex of the polymer-coated tip in the SEM image of Figure 2b is consistent with the expected increase in electron backscattering efficiency at exposed Pt-Ir regions. This conclusion was corroborated by obtaining EDX spectra as a function of position along the tip axis. Selected spots (0.05 μm x 0.05 μm) at a series of distances from the tip apex were analyzed for the presence of Pt. Pt x-ray fluorescence lines were clearly evident at the areas near the tip apex. However, the fluorescence intensity decreased as the electron beam traversed the interface between the bright and dark regions of the SEM image (Figure 2b). At distances greater than 0.5 μm beyond this interface, Pt x-ray fluorescence lines were no

longer discernible, supporting the conclusion that the dark regions in the SEM image corresponded to coated areas of the metal wire.

The exposed metal surface of the polymer-coated UME (Figure 2b) closely approximated a conical geometry, with an aspect ratio (α = 1.2) similar to that of the etched, uncoated Pt-Ir tips (Figure 3). In addition, no significant texture of the metal surface is apparent in the SEM image of Figure 2b, indicating that the surface was smooth on a scale of 0.1 μm. Though the overall conical geometry is still apparent, greater roughness is visible at the exposed metal tip of the glass-coated UME (Figure 2a). This indicates that the tip morphology produced by the etching procedure described above is not retained after exposure of the metal to the high temperatures inherent in the glass-coating procedure.

Cyclic Voltammetric Characterization of UME Tips

Cyclic voltammograms for the representative glass-coated and polymer-coated UMEs (Fig. 2) in aqueous 4.34 m$\underline{M}$ Fe(CN)$_6^{4-}$, 1.0 $\underline{M}$ KCl solutions are shown in Figure 3a and 3b, respectively. At the two slowest scan rates (2 and 10 mV/sec) in this figure, the shape of the voltammograms are sigmoidal, and no cathodic wave was observed. The combination of these two features indicates that radial diffusion was established and that steady-state mass transport conditions were present for both types of tips.[8] At faster scan rates (50, 200, 1000 mV sec^{-1}), significant forward and reverse peak currents were observed, indicating the presence of diffusional mass transport limitations on these timescales.[8]

These data can be used to estimate the critical (or smallest) dimension of the exposed metal at the UME tip. As a qualitative first approximation, the apparent hemispherical radii of these UMEs can be estimated from the limiting current, i$_l$ using the equation describing hemispherical diffusion: $i_l = 2\pi nFDCr$.[6] The limiting currents obtained from the 2 mV/sec scans in Figure 3 are i$_{l,glass}$ = 7.1 nA, and i$_{l,polm.}$ = 16.4 nA. These values

yield apparent hemispherical radii of 3.4 μm and 7.85 μm for the glass and polymer-coated UME's, respectively.

An estimate of the small dimension of the exposed metal surface is also available from the change in the shape of the cyclic voltammogram as a function of scan rate. The appearance of peaks (both cathodic and anodic) in the voltammogram indicates the onset of linear diffusion. This condition occurs when the diffusion layer thickness becomes less than the smallest dimension of the electrode.[8] Thus, an analysis of the voltammetry in the transition region between linear and spherical diffusion yields an estimate of the UME radius, which is independent of that calculated using the value of the limiting current. A quantitative treatment of linear-scan voltammetry at microdisk electrodes by Aoki et al.[5e] has shown that a unique relationship exists between the ratio of the voltammetric peak current to the steady-state limiting current, i_p/i_l, and the dimensionless parameter, $p = (nFr^2\nu/RTD)^{1/2}$ (where r = electrode radius and ν = voltage scan rate). The values of this ratio for the 1 V/sec scans shown in Figures 3a and 3b are 1.1 and 1.3, respectively. These values yield apparent microdisk radii of 2 μm for the glass coated UME (Figure 3a) and 7 μm for the polymer-coated UME (Figure 3b). These calculated values are in reasonable agreement with the apparent radii calculated from the limiting current formula for hemispherical diffusion to these UMEs.

Analysis of SEM images and EDX spectra allowed the cone base radius of the polymer-coated and glass-coated UME's to be established as 8.2 μm and 2.8 μm, respectively. These values are compared in Table I with those obtained from cyclic voltammetry. Since the apparent voltammetric radius values were calculated using the hemispherical limiting current equation (vide supra), the agreement shown in Table I between the SEM data and the apparent electrochemical radius data suggests that this equation is an acceptable approximation to the steady-state electrochemical behavior of these cone-shaped UMEs. Of course, a more quantitative treatment (necessary for time-

dependent processes, *vide infra*) would account for the deviation in actual area of a cone

and hemisphere with identical radii. However, the close agreement evident in Table I

between qualitative electrochemical radii and actual geometric radii did prove to be a

satisfactory guide for the selection of polymer-coated UMEs of various metal areas.

Chronoamperometry

A quantitative evaluation of the electrochemical behavior of these

ultramicroelectrodes is possible using chronoamperometry.[9] Figure 4a shows typical i *vs.*

$t^{-1/2}$ data in aqueous 0.5 $\underline{M}$ Na$_2$SO$_4$- 4.21 m$\underline{M}$ Fe(CN)$_6^{4-}$ solutions for polymer-coated UMEs

possessing radii of 1.7, 4.8, and 6.5 μm (as estimated from the observed i$_l$ values for these

electrodes). In these experiments, the potential was stepped from 0.0 V to 0.5 V *vs.* SCE.

Note that the linearity of these plots is excellent (correlation coefficient > 0.99) for times

between 70 μsec and 0.01 sec.

Because the concentration of ferrocyanide in this solution and its diffusion

coefficient (7.94 x 10^{-6} cm^2/sec (Ref. 9a) are known, the slopes of these plots can be used in

the Cottrell equation to calculate an apparent electrode area. These areas are listed in Table

II.

The i *vs.* $t^{-1/2}$ data at long times (t > 1 msec) are shown in greater detail in Figure 4b.

Positive deviations of the experimental data from the Cottrell line are particularly evident for

the 4.8 μm and 6.5 μm radii UME's. These positive deviations are expected in the time

interval where a transition from linear diffusion to hemispherical diffusion occurs.[9a] This

change in the mode of diffusion will occur when the diffusion layer increases in thickness

and assumes dimensions greater than those of the conical metal surface.[8] Thus, a

quantitative analysis of the i *vs.* t data in this transition region should yield information

regarding the size and the geometry of the exposed metal at the UME tip.

A first-order mathematical description of the chronoamperometric transients for a general electrode geometry can be obtained by writing the total diffusion limited current as a sum of the planar flux and radial flux diffusion components:[5a,6]

$$i_{total} = i_{planar} + i_{radial} \tag{1}$$

The form of the planar component of this expression is given by the well-known Cottrell Equation:[6]

$$i_{planar} = nFAD^{1/2}C/(\pi^{1/2}t^{1/2}) \tag{2}$$

This portion of the total current can be calculated for any electrode geometry, and will provide an excellent approximation to the total diffusion limited current at sufficiently short electrolysis times. For the particular UME geometries of interest in this work, the hemispherical area is given simply by $A_{hemi}=2\pi r^2$, while the conical area, A_{cone}, equals $\pi r_c(h^2 + r_c^2)^{1/2}$, where h and r_c are equal to the height and base radius, respectively, of a right circular cone.

The geometric information of interest is contained in the radial diffusion term of Equation (1). For spherical, hemispherical and disk UME geometries, a general expression for the radial component in Equation (1) has been found to be:[5a]

$$i_{radial} = arnFDC \tag{3}$$

where r is the electrode radius, and a is a function of the electrode geometry. For spheres $a=4\pi$, for hemispheres $a=2\pi$, and for disks, the apparent a is time-dependent but approaches $a=4$ as $t \rightarrow \infty$. To date, the applicability of this treatment and the appropriate value of a are

unknown for conical electrodes, because the conical UME geometry has not been available for investigation.

Thus, if Equation (1) provides a correct description of the diffusion limited current response of a conical UME, the only adjustable parameter in the fitting of the chronoamperometric data in Figure 4 is the value of a. To apply Equation (1) to this UME geometry, the Cottrell area of the UME was obtained from the slopes of the i vs. $t^{-1/2}$ data at times < 0.01 sec ($t^{-1/2}$ > 10 $sec^{-1/2}$), using Eq. (2). The measured Cottrell areas were then used in conjunction with the observed cone aspect ratio of 1.2 (Figure 2b) to calculate a value for r_c, the base radius of the cone. Fitting the long time regions of the chronoamperogram to Equations (1) - (3) then yielded a best value for a.

Figure 5 displays experimental and theoretical log i vs. log t plots for the three UMEs used in the chronoamperometry shown in Figure 4. Only the UMEs with the two largest radii yielded chronoamperometry that deviated from hemispherical diffusion predictions; thus, only these electrodes yielded values for r_c and a (Table II), using the conical diffusion treatment described above. For these two conical UMEs, the agreement between the two values for a is excellent. Furthermore, measurement of numerous other conical UMEs in this radius range yielded a values of 1.9π - 2.2π. Thus, the apparent a value for these types of conical electrodes, obtained from the steady-state portion of the chronoamperogram, was close to that calculated for a hemispherical electrode geometry, $a_{hemi} = 2\pi$.[6,10] Of course, the value of a also depends on the geometry and extent of the insulating region of the electrode assembly; thus, the values for conical electrodes obtained in this work are probably fortuitously close to the $a=2\pi$ value calculated for a hemisphere on an infinite insulating planar support.

Another method for determining the value of a is to utilize the relationship between the steady-state limiting current in the cyclic voltammetry (Figure 2) and the conical base radius r_c as determined by SEM. For steady-state diffusion, Equation (3) should describe the

relationship between r_c and the total observed current at the UME. For the polymer-coated conical UME of Figure 2b, using the value for r_c determined by SEM analysis (8.2 μm) and the observed i_l value at 2 mV/sec (i_l = 16.4 nA) yields a value for a of 1.9π. This value is in excellent agreement with those determined by analysis of the chronoamperometry data using Equation (1). This implies that the semiquantitative approach of Equation (1) is a quite satisfactory description of the diffusional behavior of these conical UMEs over a range of radii and time regimes.

Also shown in Figure 5 are log i $vs.$ log t calculations for these UMEs based on a hemispherical electrode geometry. These data are presented merely to illustrate the deviation from pure hemispherical diffusion displayed by these conical UMEs. To obtain these fits, a value for r was obtained from the steady-state limiting current using Eqn. (3) with $a=2\pi$, as expected for a hemisphere. The entire theoretical chronoamperogram was then calculated using this value for r with $a=2\pi$ and $A=2\pi r^2$ in Eqns. (1)-(3), as would hold if the UME were indeed a hemisphere. Note that for the 4.8 μm and 6.5 μm radii UMEs, the currents calculated using this method underestimate the actual values in the short time (Cottrell) regime. For example, the 6.5 μm UME has a response in the Cottrell region which is displaced by 0.1 = log 1.25 from the hemispherical calculation. The discrepancy indicates that the actual electroactive surface area of the UME is 25% greater than that expected, given the erroneous assumption that the UME is indeed a hemisphere.

The correction in area necessary to achieve agreement between the hemispherical UME model and the actual Cottrell area is further evidence for a conical UME geometry. An aspect ratio of 1.20 is required for a right circular cone of base radius r_c= 6.5 μm to yield a 25% increase in exposed area relative to a hemisphere with r=6.5 μm. Similarly, the aspect ratio required for a 25% increase in area of the 4.8 μm UME is α = 1.19. These values, summarized in Table II, agree well with the geometric α values of 1.2-1.3 obtained by direct SEM measurements on these electrodes.

The electrochemical behavior of the 1.7 μm radius UME (Figure 5c) is distinctly different from that of the larger radii UMEs discussed above. Note that the calculated log i vs. log t data for the hemispherical model overlays the experimental data over the entire time regime investigated. Thus, the electrochemical behavior of this electrode with respect to chronoamperometry is essentially indistinguishable from that of a hemispherical UME over the full range of experimental times.[6,9] Significantly, UMEs that exhibited hemispherical diffusion behavior always possessed radii < 2 μm.

For both the 4.8 and the 6.5 μm radii UMEs of Figure 5, the current calculated from Equation (1) is in good (but not perfect) agreement with the data over the entire experimental time interval. The slight overestimate of the actual current in the transition region indicates that the apparent value for a is too large in this time interval. This observation is evidence for an apparent a coefficient that is weakly time-dependent over this time regime. A similar situation has been observed for chronoamperometry at microdisk electrode surfaces.[5a,9] Observation of a time-dependent apparent a is equivalent to stating that the first-order treatment given by Equation (1) is not a rigorously correct solution to the diffusion equations in this time regime. However, a rigorous solution to the diffusion equation for a cone is expected to be quite complicated, and the semiquantitative approach embodied by Equations (1)-(3) is quite satisfactory for describing the behavior of our UMEs over the time regimes of usual experimental interest.

Discussion

The combination of SEM images, cyclic voltammetry, and chronoamperometry data indicates that the tip etching/coating process is capable of producing well-defined conical and apparent hemispherical ultramicroelectrode tip geometries. The larger radii UMEs (r > 2 μm) exhibited electrochemical behavior in accord with diffusion to a cone, and the aspect ratio and base-cone radius of these electrodes given by the SEM analysis were consistent

with the electrochemical behavior of these tips. In contrast, for smaller radii UMEs (r < 2 μm), chronoamperometric data for t>70 μs was consistent with hemispherical diffusion. Although *hemispherical mercury microelectrodes have been reported previously,*[11] the fabrication procedure reported here is the first to our knowledge to yield solid metal electrodes in this theoretically advantageous diffusion geometry.[1]

Assuming that the UMEs share a common etched-tip geometry, a unified picture, Scheme I, can be obtained for the effects of the tip coating process. When the radius of the exposed metal approaches the ultimate etche-tip radius (r $\approx$ 1 μm), the apparent electrochemical geometry of the exposed metal should approximate that of a hemisphere. Greater UME diameters should display greater amounts of surface area on the conical tip surface. As shown in Table II, this behavior is in accord with the data for the UMEs examined in this work. The 1.7 μm radius electrodes exhibited a chronoamperometric response in accord with that expected for a hemispherical electrode over the entire experimental time range, while significant deviations from hemispherical behavior were observed for the 4.8 μm and 6.5 μm radii UMEs.

Our two-step fabrication procedure is conceptually simple and is similar to procedures used previously to prepare glass-insulated Pt-Ir electrodes for *in vivo* potentiometry in neurophysiology applications.[12] However, both the etching and coating steps of the procedure have undergone significant refinement, in order that geometrically well-defined and microscopically smooth metal surfaces are exposed after insulator coating. In addition, previous workers have found it necessary to subject the coated and etched metal wire to an intentional "exposure step," in which the insulating material is apparently removed from the coated assembly to expose bare metal.[12] We have found that this step is unnecessary, because exposed metal areas with the desired geometries and intimate insulator-metal seals, are present in coated wires prepared by our etching/coating process.

UMEs with radii both larger and smaller than those described above could be obtained by manipulating the coating conditions as described described above and in Chapter 4. The smallest UME radius obtained using the fabrication methods described here was 1.5 nm (estimated from the voltammetric limiting current). It was routinely possible to prepare UMEs with somewhat larger radii of 0.2-0.5 μm using either the glass or polymer-coating procedures. These latter values are comparable to the smallest electrode radii accessible using conventional microdisk construction techniques.[1]

Use of Tip UMEs for Measurement of Heterogeneous Rate Constants

A straightforward application of our insulated-tip UME design is in the measurement of heterogeneous electron transfer rate constants. The rate of mass transport to a UME is extremely rapid and varies with the reciprocal of the critical electrode dimension. Thus, mass transport to a sufficiently small UME can be rapid enough so that electron transfer kinetics dominate the overall charge transfer rate. The effect of kinetic limitations on measured steady-state voltammograms at a UME is depicted in Figure 6. Curve A in the figure is an idealized cyclic voltammogram (normalized to the limiting current value) for a reversible electrochemical reduction. Such voltammetry should be exhibited for all 1-electron electrochemical reactions possessing a standard heterogeneous rate constant (k^o) greater than the mass transfer coefficient (D/r) of the system (vide infra).[13] When k^o is less than D/r, however, kinetic limitations will be apparent in the steady-state cyclic voltammetry data. In this case a response such as that depicted in curve B of Figure 6 will be obtained. The shape of this quasi-reversible steady-state voltammogram is related to the rate constant (k^o) and transfer coefficient (α_e) for the electron transfer process (vide infra).

The theory for reversible and quasi-reversible steady-state voltammetry at spherical electrodes was described first by Delmastro and Smith,[14a] and later by Bond and Oldham.[14b] Modifications to the theory that are needed to address the hemispherical

geometry were introduced by Oldham and Zoski.[15] The current is related to the applied potential through Equation (4):

$$i = i_{lim}/(\theta + (\pi^2/8\kappa))$$ (4)

where i_{lim} is given by Eqn. (3) with $a = 2\pi$ and the potential dependent variables θ and κ are defined as follows:

$$\theta = 1 + D_O/D_R exp[nF/RT(E-E^{o'})]$$ (5)

$$\kappa = (\pi^2 k^o r/8D_o)exp[-\alpha_e nF/RT(E-E^{o'})]$$ (6)

In the limit of $\theta >> \kappa$, Eqn. (4) (Ref. 15) reduces to the expression that describes the reversible steady-state current/voltage behavior at a hemispherical UME. It was under these conditions that curve A of Figure 6 was plotted ($\alpha_e = 0.5$). In contrast, curve B of the figure was obtained with $k^o < D_O/r$ with the same value for α_e. This curve is shifted to more negative potentials, and the slope of the curve through $E^{o'}$ has been reduced. Curves C and D in Figure 6 indicate the effect that changes in α_e have on the shape of a quasi-reversible voltammogram. Thus, it is important to note that changes in α_e and k^o affect the simulated voltammogram in unique ways.

Figure 7 shows cyclic voltammetry data for the reduction of $Ru(NH_3)_6^{3+}$ in an aqueous 50 m$\underline{M}$ KPF_6 solution obtained with a glass-coated UME ($r = 3.4 \mu$m). The solid curve in the figure is the expected i vs. V behavior for the reversible reduction reaction based on the measured limiting current to the electrode. We have observed this curve when relatively large UMEs were employed ($r > 10 \mu$m). The data, represented by the squares in the figure, do not fall on this curve, evidently because of kinetic limitations. In order to fit the data, values for the electrode radius, r, were obtained from the limiting current by using Eqn.

(3) with $a=2\pi$ and the known values for the concentration of $Ru(NH_3)_6{}^{3+}$ (0.407 m$\underline{M}$) and for

the diffusion coefficient, D_O.[16] A value for k^o was obtained by manually fitting the

experimental current at $E^{o'}$, and α_e was obtained from the best fit of the I/V data in the

potential interval $E^{o'}$ ± 10 mV. The values for k^o and α_e that produce the best fit to the data in

Figure 7 are 0.375 cm/sec and 0.9, respectively. These values are in good agreement with

the results obtained by Gennett and Weaver[17] (k^o = 0.35, α_e = 0.65), and by Wipf et al.[16] (k^o

= 0.45 ± .12, α_e = 0.63), on mercury surfaces.

Repeated fitting of a given data set indicated that variations on the order of ±20% are

introduced by the fitting process itself with the $E_{1/2}$ shifts (i.e. potential values at which the

current is ½ of the limiting value) from the reversible behavior that were encountered in

these investigations (5-8 mV). A conservative estimate of other sources of error (i.e., data

digitization and reference electrode drift) renders the $E_{1/2}$ values uncertain by < 2 mV.

Including these potential sources of error, we have determined average values of k^o and α_e

to be 0.26 (+0.38/-0.1) cm/sec and 0.8 ± 0.1, respectively, from measurements on 3 glass-

coated and 3 polymer-coated UMEs (electrode sizes in the range 1.6 - 5.3 μm). These

results remain in good agreement with those of Gennett and Weaver[17] and Wipf et al.[16]

despite the fact that work-term corrections have not been made.[18] Of course, more precise

numbers could be obtained for the reduction of $Ru(NH_3)_6{}^{3+}$ with the use of smaller UMEs.

Summary

A new method for preparing glass and polymer-coated Pt-Ir(30%) UMEs has been

presented. The resulting electrodes have been characterized with SEM, cyclic voltammetry,

and chronoamperometry. The larger electrodes (r > 2 μm) represent the first reported UMEs

with a conical geometry, while the smaller ones (r< 2 μm) behave as well-defined

hemispheres. The application of these UMEs to the measurement of fast heterogeneous

rate constants has also been demonstrated.

This new UME design possesses a number of significant features: 1) no mechanical pretreatment (i.e., polishing) of the UME is required (because the etched metal surface is microscopically smooth), 2) the metal-insulator seals of these electrodes are reproducible and abrupt, and 3) the procedure does not require the handling of micron-sized wire that is commonly used in conventional microdisk fabrication processes. Polymer-coated versions of these UMEs can be prepared with a minimum of equipment in any electrochemical laboratory.

A possible disadvantage of this design is the fact that the metal surface of the UMEs described here cannot be renewed by polishing. This problem is inherent to the protruding hemispherical geometry, but is partially offset by the ease with which new UMEs can be prepared using our procedure.

Several obvious applications of our UME tips include use in high-speed electroanalytical methods, where the advantageous geometry and low total exposed surface area can be exploited, and in neurophysiological studies that require easily prepared, chemically inert, implantable microelectrodes. Additionally, preliminary results from our laboratory suggest that heterogeneous rate constants larger than 100 cm/sec can be measured with extremely small versions (r < 5nm) of these UMEs. Use of these well-defined UMEs in a scanning tunneling microscope configuration should enhance the limiting resolution of scanning electrochemical microscopy, which is currently obtained using 5-10 μm radius wires.[19] Additionally, scanning ultrathin layer cells could be formed for determination of the spatial distribution of heterogeneous rate constants on conducting surfaces. In this configuration our electrodes should also allow control of the electric field line distribution between the UME and a planar electrode to permit extremely small-scale lithography. Applications of this tip-fabrication procedure to these problems is currently being explored, and will be described in future publications from our laboratory.

References

1. Fleischmann, M.; Pons, S.; Rolison, D.R.; Schmidt, P.P. *Ultramicroelectrodes*, Datatech Systems, Inc. Morganton, NC, 1987; Chapter 3.

2. (a) Howell, J.O.; Wightman, R.M. *Anal. Chem.* **1984**, *56*, 524-529. (b) Howell, J.O.; Wightman, R.M. *J. Phys. Chem.* **1984**, *88*, 3915-3918. (c) Montenegro, M.I.; Pletcher, D. *J. Electroanal. Chem.* **1986**, *200*, 371-374. (d) Fitch, A; Evans, D.H. *J. Electroanal. Chem.* **1986**, *202*, 83-92. (e) Amatore, C.A.; Jutand, A.; Pfuger, F. *J. Electroanal. Chem.* **1987**, *218*, 361-365. (e) Andrieux, C.P.; Garreau, D.; Hapiot, P.; Pinson, J.; Saveant, J.M. *J. Electroanal. Chem.* **1988**, *243*, 321-335. (f) Wipf, D.O.; Kristensen, E.W.; Deakin, M.R.; Wightman, R.M. *Anal. Chem.* **1988**, *60*, 306-310. (g) Andrieux, C.P.; Garreau, D.; Hapiot, P.; Saveant, J.M. *J. Electroanal. Chem.*, **1988**, *248*, 447-449. (h) Wipf, D.O.; Wightman, R.M. *Anal. Chem.* **1988**, *60*, 2460-2464.

3. (a) Bond, A.M.; Fleischmann, M.; Robinson, J. *J. Electroanal. Chem.* **1984**, *168*, 299-312. (b) Bond, A.M.; Fleischmann, M.; Robinson, J. *J. Electroanal. Chem.* **1984**, *180*, 257-263. (c) Cassidy, J.; Khoo, S.B.; Pons, S.; Fleischmann, M. *J. Phys. Chem.* **1985**, *89*, 3933. (d) Dribble, T.; Bandyopadhyay, S.; Ghoroghchian, J.; Smith, J.J.; Sarfarazi, F.; Fleischmann, M.; Pons, S. *J. Phys. Chem.* **1986**, *90*, 5275-5277. (e) Bruckenstein, S. *Anal. Chem.* **1987**, *59*, 2098-2101.

4. (a) Dayton, M.A.; Ewing, A.G.; Wightman, R.M. *Anal. Chem.* **1980**, *52*, 2392-2396. (b) Scharifker, B.; Hills, G. *J. Electroanal. Chem.* **1981**, *130*, 81-97. (c) Russell, A.; Repka, K.; Dribble, T.; Ghoroghchian, J.; Smith, J. J.; Fleischmann, M.; Pitt, C.H.; Pons, S. *Anal. Chem.* **1986**, *58*, 2961-2964. (d) Bond, A.M., Oldham, K. B.; Zoski, C. G. *J. Electroanal. Chem.* **1988**, *245*, 71-104. (e) Oldham, K.B.; Zoski, C.G.; Bond, A. M.; Sweigart, D.A. *J. Electroanal. Chem.* **1988**, *248*, 467-473. (f) Galus, Z.; Golas, J.; Osteryoung, J. *J. Phys. Chem.* **1988**, *92*, 1103-1107. (g) Bond, A.M.; Henderson, T.L.E.; Mann, D.R.; Mann, T.F.; Thormann, W.; Zoski, C.G. *Anal. Chem.* **1988**, *60*, 1878-1882.

5. (a) Dayton, M.A.; Brown, J.C.; Stutts, K.J.; Wightman, R.M. *Anal. Chem.* **1980**, *52*, 946-950. (b) Oldham, K.B. *J. Electroanal. Chem.* **1981**, *122*, 1-17. (c) Galus, Z; Schenk, J.O.; Adams, R.N. *J. Electroanal. Chem.* **1982**, *135*, 1-11. (d) Shoup, D.; Szabo, A. *J. Electroanal. Chem.* **1982**, *140*, 237-245. (e) Aoki, K.; Akimoto, K.; Tokuda, H.; Osteryoung, J. *J. Electroanal. Chem.* **1984**, *171*, 219-230.

6. Galus, Z. *Fundamentals of Electrochemical Analysis*, Halsted Press: New York, 1976; Chapter 4.

7. Petzow, G. *Metallographic Etching*, American Society for Metals: Metals Park, OH, 1978; Chapter 1.

8. Wightman, R. M. *Anal. Chem.* **1981** *53*, 1125A-1134A.

9. (a) Hepel, T; Osteryoung, J. *J. Phys. Chem.* **1982**, *86*, 1406-1411. (b) Hepel, T.; Plot, W.; Osteryoung, J.; *J. Phys. Chem.* **1983**, *87*, 1278.

10. Delahay, P. *New Instrumental Methods in Electrochemistry*, Interscience: New York, 1954; p. 54.

11. (a) Lines, R.; Parker V.D. *Acta Chemica Scand.* **1977**, *B31*, 369. (b) Wehmeyer, R. K.; Wightman, R.M. *Anal. Chem.* **1985**, *57*, 1989-1993. (c) Golas, J.; Osteryoung, J. *Anal. Chem. Acta* **1986**, *186*, 1-9. (d) Golas, J.; Osteryoung, J. *Anal. Chem. Acta* **1986**, *181*, 211-218. (e) Golas, J.; Galus, Z.; Osteryoung, J. *Anal. Chem.* **1987**, *59*, 389-392.

12. (a) Wolbarsht, M.L.; MacNichol, E.F., Jr.; Wagner, H.G. *Science*, **1960**, *132*, 1309-1310. (b) Guld, C. *Med. Electron. Biol. Eng.* **1964**, 2, 317-327.

13. Bard, A.J.; Faulkner, L.R. *Electrochemical Methods*, John Wiley and Sons: New York, 1980; p. 28.

14. (a) Delmastro, J.R.; Smith, D.E. *J. Phys. Chem.* **1967**, 71, 2138. (b) Bond, A.M.; Oldham, K.B. *J. Electroanal. Chem.* **1983**, 158, 193.

15. Oldham, K.B.; Zoski, C.G. *J. Electroanal. Chem.* **1988**, 256, 11-19.

16. Wipf, D.O.; Kristenson, E.W.; Deakin, M.R.; Wightman, R.M. *Anal. Chem.* **1988**, 60, 306-310.

17. Gennett, T.M.; Weaver, M.J. *Anal. Chem.* **1984**, 56, 1444.

18. (a) Marcus, R.A. *J. Chem. Phys.* **1965**, 43(2), 679-701. (b) Barr, S.W.; Guyer, K.L.; Weaver, M.J. *J. Electroanal. Chem.* **1980**, 111, 41-59.

19. (a) Lin, C.W.; Fan, F.-R.F.; Bard, A.J. *J. Electrochem. Soc.* **1987**, *134*, 1038-1039. (b) Craston, D.H.; Lin, S.W.; Bard, A.J. *J. Electrochem. Soc.* **1988**, *135*, 785-786. (c) Bard, A.J.; Fan, F.-R.F.; Kwak, J.; Lev, O. *Anal. Chem.* **1989**, *61*, 132-138.

Table I. Comparison of UME Radii Determined From SEM Data and Cyclic Voltammetric Data For Typical Glass and Polymer-Coated UMEs.

Electrode	r_{SEM} (μm)[a]	r_l (μm)[b]	r_{CV} (μm)[c]
glass	2.8	3.40	2
polymer	8.2	7.85	7

[a]Radius at the base of the exposed metal surface as estimated from SEMs shown in Figure 2.

[b]Radius calculated from the voltammetric limiting current at ν = 2 mV/sec using the expression for steady-state hemispherical diffusion, $i_l = 2\pi FDCr$ (6).

[c]Radius estimated from the ratio i_p/i_l at ν = 1 V/sec using a microdisk voltammetric model (5e).

Table II. Summary of Geometric Data For Polymer-Coated UMEs Obtained From Chronoamperometry Experiments.

A_{expt} (cm^2)[a]	r_c (μm)	a	$\dfrac{A_{expt}[f]}{A_{hemi}}$	α[g]
3.46×10^{-6}	6.51[b]	2.000π[d]	1.29	1.19
1.91×10^{-6}	4.84[b]	2.002π[d]	1.30	1.20
1.81×10^{-7}	1.70[c]	2.000π[e]	1.00	--

[a]Areas calculated from the slopes of the i vs. t$^{-1/2}$ plots (Figure 4a) using the Cottrell Eqn. (Eqn. 2).

[b]Base radius of the right circular cone with aspect ratio, α, =1.2, that possesses the Cottrell area listed in column 1. (Calculated using the equation $A = \pi r_c (r_c + h_c)^{1/2}$).

[c]Radius of the hemisphere which possesses the Cottrell area listed in column 1.

[d]Value of the a coefficient obtained by fitting the experimental log i vs. log t data (Figure 7) with the conical model (Eqns. 1-3) in the steady-state time regime. Values for the radius are listed in column 2 and α=1.2 is assumed.

[e]Value of the a coefficient from the hemispherical diffusion model.

[f]Ratio between the experimentally determined Cottrell areas for each UME listed in column 1 and the surface area of a hemisphere possessing the radius listed in column 2.

[g]Aspect ratio, α = cone height/cone diameter, of a right circular cone possessing a surface area equal to the experimentally determined value and a radius calculated from the limiting current at each UME, using the hemispherical diffusion equation (Eqn. (3), a = 2π).

Figure 1:

Scanning electron micrograph of the apex of a Pt-Ir(30%) wire after electrochemical

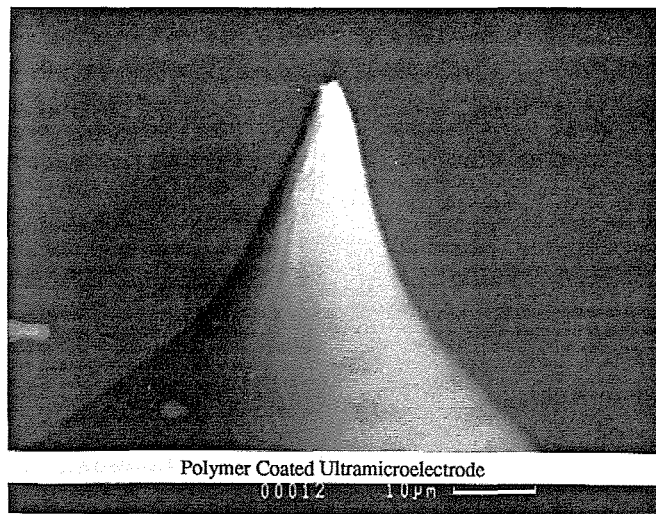etching.

Freshly Etched Pt-Ir Tip
00023   3μm

Figure 2:

Scanning electron micrographs of (a) the glass-coated UME used to obtain the cyclic voltammetry shown in Figure 3a, and (b) The polymer-coated UME used to obtain the cyclic voltammetry data in Figure 3b.

Glass Coated Ultramicroelectrode

00028   3μm

(a)

Polymer Coated Ultramicroelectrode

00012   10μm

(b)

Figure 3:

A: Cyclic voltammograms for the glass-coated UME of Figure 2a immersed in 4.34 m$\underline{M}$

$Fe(CN)_6^{4-}$, 1 $\underline{M}$ KCl(aq) at potential scan rates of (a) 2, (b) 10, (c) 50, (d) 200, (e) 1000 mV/s.

B: Cyclic voltammograms for the polymer-coated UME of Figure 2b in the same solution.
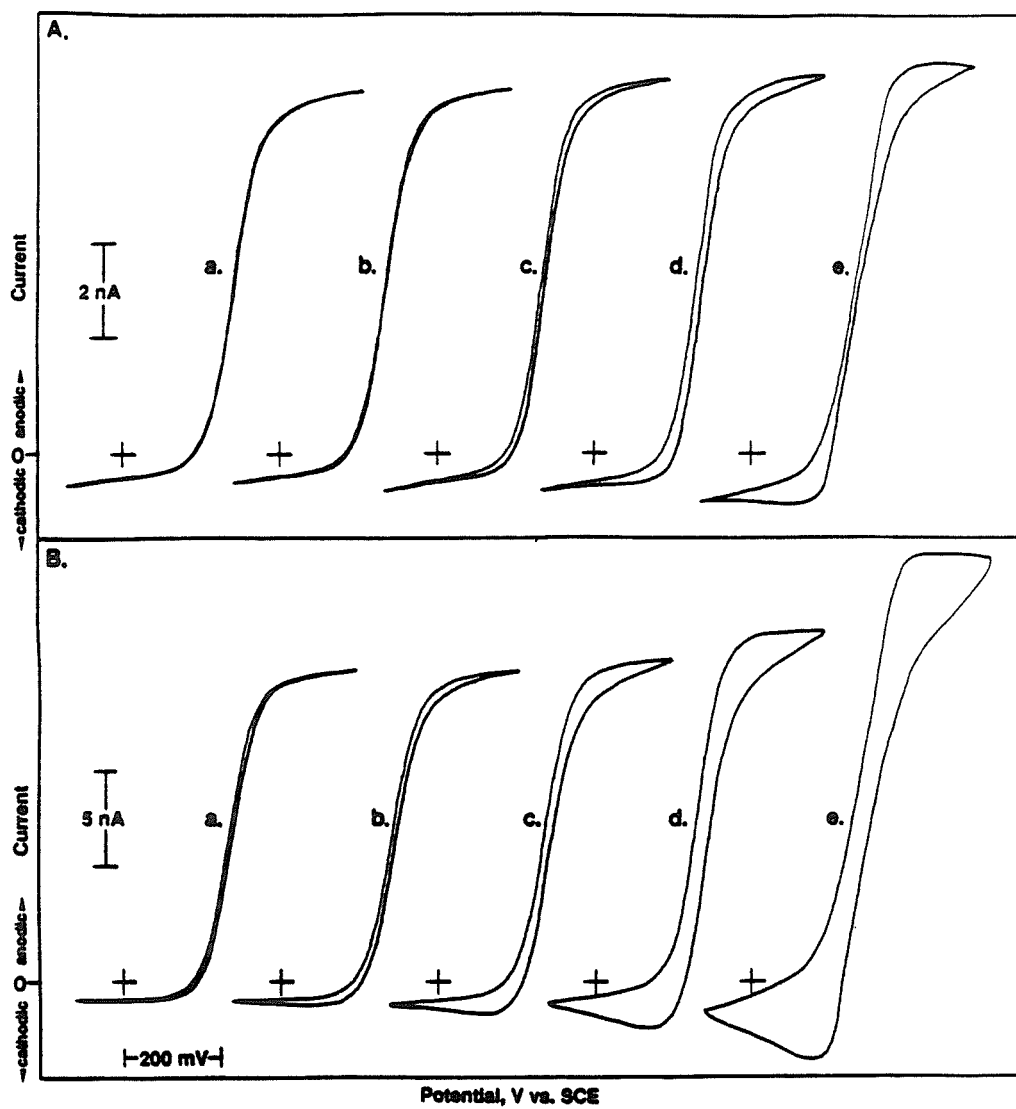
Scan rates are the same as in part A of this figure.

Figure 4:

Current vs. time$^{-1/2}$ plots for potential steps at three polymer-coated Pt-Ir UMEs of different sizes. Potential steps were applied from 0.0 to 0.5 V vs. SCE in 4.21 m$\underline{M}$ Fe(CN)$_6^{4-}$, 0.5 $\underline{M}$ Na$_2$SO$_4$ (aq). Panel A shows plot of data for time intervals from 70 μs to 3 s; B, data for time interval from 1 ms to 3 s.

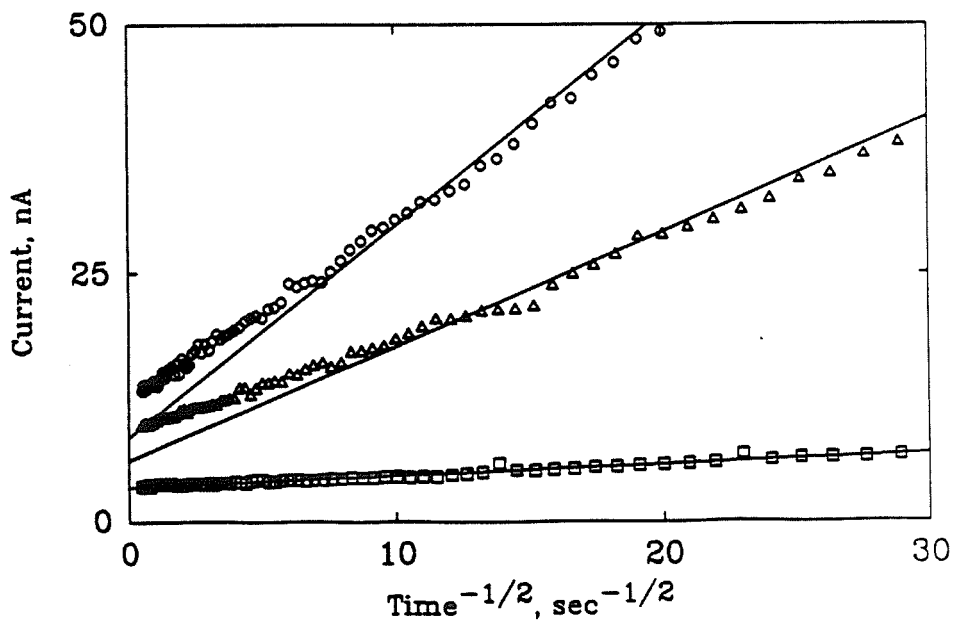Solution: aqueous 4.21 m$\underline{M}$ Fe(CN)$_6^{4-}$, 0.5 $\underline{M}$ Na$_2$SO$_4$.
Initial potential: 0.0 V, final potential: 0.5 V.
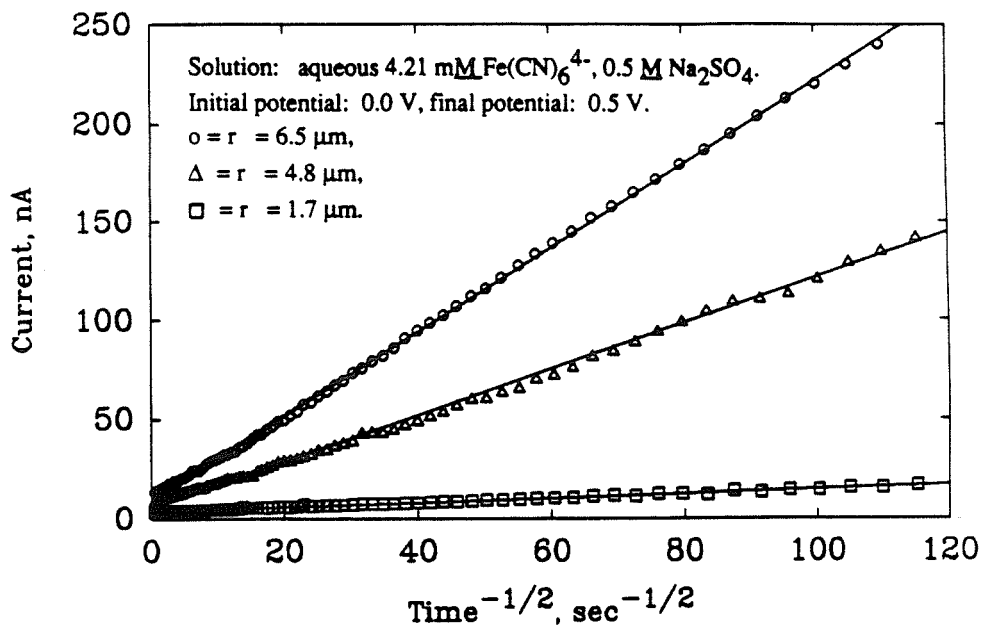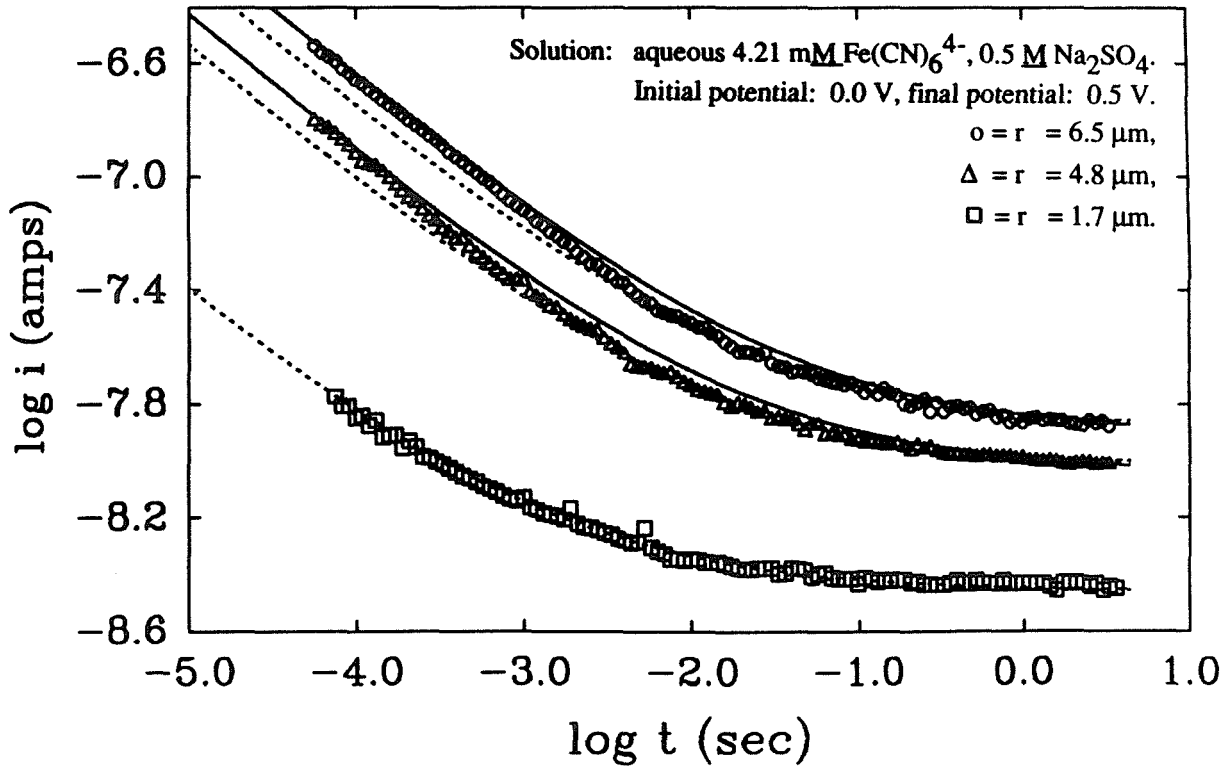o = r = 6.5 µm,
Δ = r = 4.8 µm,
□ = r = 1.7 µm.

Figure 5:

Comparison of experimental log i vs. t data for the plots in Figure 4 with the theoretical

behavior expected for both the conical electrode geometry (solid line) and the

hemispherical electrode geometry (broken line). The calculations were done by using
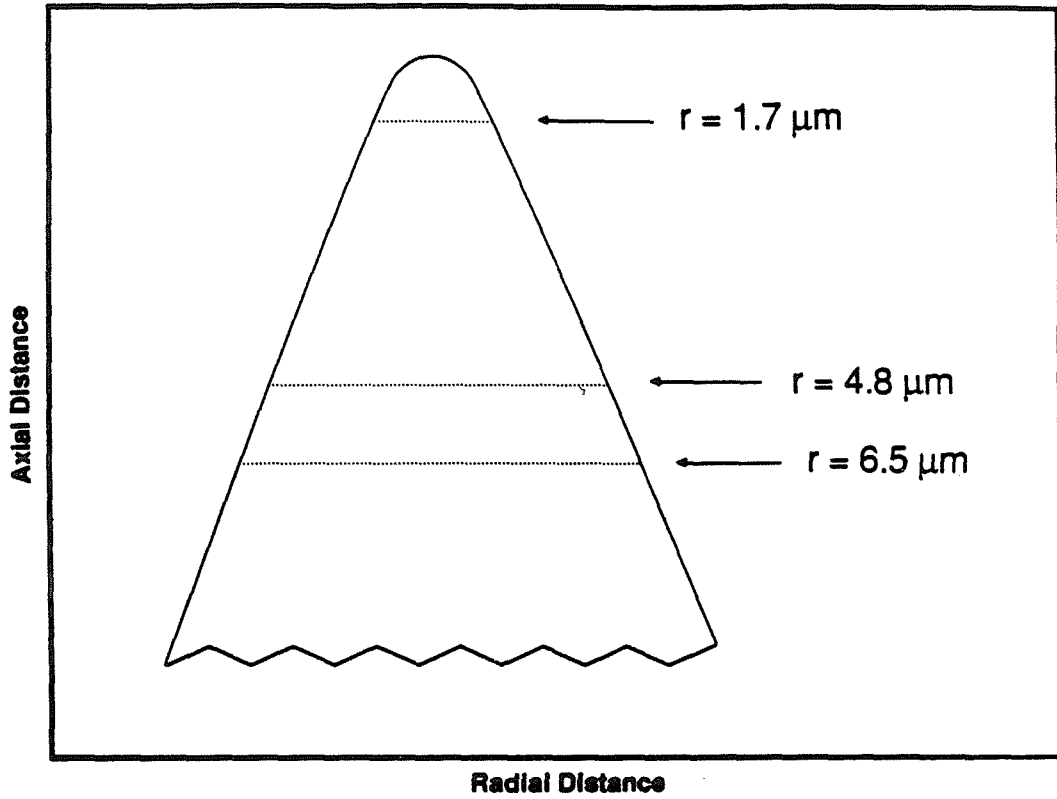
Eqns. 1-3, as described in the text.

Solution: aqueous 4.21 m$\underline{M}$ Fe(CN)$_6^{4-}$, 0.5 $\underline{M}$ Na$_2$SO$_4$.
Initial potential: 0.0 V, final potential: 0.5 V.
o = r = 6.5 μm,
Δ = r = 4.8 μm,
□ = r = 1.7 μm.

Scheme 1:

Representation of the-etched tip geometry showing the approximate location of the

insulator-metal interface (broken lines) for the 1.7 μm, 4.8 μm, and the 6.5 μm radii

polymer-coated UMEs examined with chronoamperometry.

Scheme I

Figure 6:

Simulated steady-state cyclic voltammograms formed with use of Equation 4. A: Current

vs. voltage curve for a reversible electrochemical reduction with $\alpha_e = 0.5$; B: Current vs.

voltage curve for a quasi-reversible electrochemical reduction with $\alpha_e = 0.5$; C: Same as

curve B but with $\alpha_e = 0.7$; D: Same as curve B but with $\alpha_e = 0.4$.

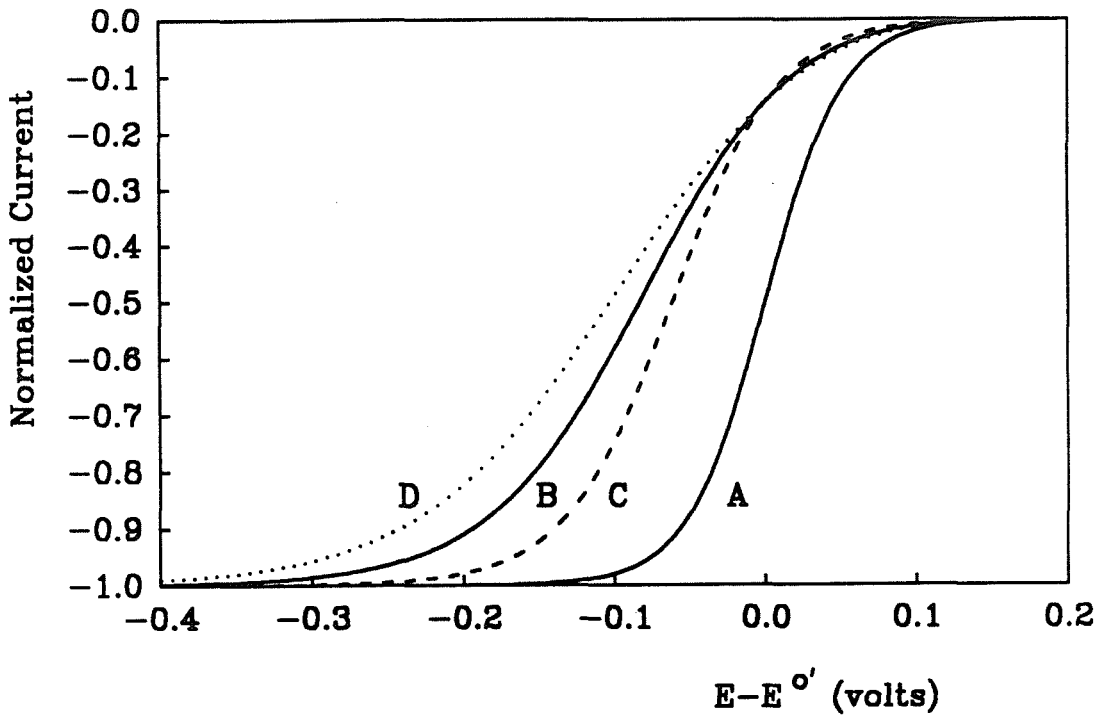Figure 7:

Cyclic voltammetry data for the reduction of 0.407 m$\underline{M}$ Ru(NH$_3$)$_6$$^{3+}$ in 50 m$\underline{M}$ KPF$_6$ obtained

with a 3.4 μm glass-coated electrode. The experimentally measured data are represented

by squares. The solid curve represents the expected behavior for reversible steady-state

voltammetry. The dashed line is the best fit to the data using Equations 4-6 (see text).